Experimental Characterization of Condensation Behavior for Metastable Carbon Dioxide

by

Derek Edwin Paxson

Submitted to the Department of Aeronautics and Astronautics
in partial fulfillment of the requirements for the degree of

Masters of Science

at the

MASSACHUSETTS INSTITUTE OF TECHNOLOGY

September 2016

Author .....
Department of Aeronautics and Astronautics
July 6, 2016

Certified by .....
Zoltán S. Spakovszky
Professor of Aeronautics and Astronautics
Thesis Supervisor

Accepted by .....
Paulo C. Lozano
Chair, Graduate Program Committee

Experimental Characterization of Condensation Behavior for Metastable Carbon Dioxide

by

Derek Edwin Paxson

Submitted to the Department of Aeronautics and Astronautics
on July 6, 2016, in partial fulfillment of the
requirements for the degree of
Masters of Science

Abstract

This thesis is focused on the experimental characterization of the thermodynamic properties and behavior of carbon dioxide (CO_2) undergoing non-equilibrium condensation near the critical point in a convergent-divergent nozzle. The insight gained facilitates new modelling tools that guide the design of more efficient compressors for applications such as carbon capture and sequestration (CCS), enhanced oil recovery (EOR), and Supercritical CO_2 power cycles.

Modelling of non-equilibrium condensation requires knowledge of the fluid's metastable (subcooled-vapor) properties and related stability limit, known as the Wilson line. While there have been computational studies on metastable CO_2, there is no experimental data in the literature to anchor these results for conditions near the critical point. A laboratory scale blowdown experiment was constructed to visualize the onset of condensation, allowing for a first-of-its-kind assessment of the Wilson line, and the accuracy of two methods for determining metastable properties: spline-based extrapolation and equation of state (EOS) based extrapolation using the Span and Wagner EOS.

The experiment consists of a heated charge tank and an optically accessible instrumented convergent-divergent nozzle. The nozzle was sized such that relevant length and time-scales were similar to those of the flow around a compressor leading edge. Pressure transducers were used to provide static pressure data, and a novel shearing interferometer, tailored to the high densities of supercritical CO_2, was developed to measure the static density. The maximum errors between measured and calculated metastable densities are 2%, and 15% for the Span and Wagner EOS and tabular extrapolation methods, respectively. The conditions under which condensation was observed in the experiment were used to establish the Wilson line. Based on this, a new safety limit for compressor inlet conditions near the critical point enabling greater compressor efficiencies was developed.

Thesis Supervisor: Zoltán S. Spakovszky
Title: Professor of Aeronautics and Astronautics

Acknowledgments

First and foremost, I would like to thank my advisor, Professor Zoltán S. Spakovszky. Without his guidance, knowledge, and support over the past two years, this research would not have been possible. I would also like to thank Dr. Claudio Lettieri for his help throughout my time at MIT even after he had moved to Delft. James Letendre was another invaluable resource during my introduction to the project and the CO_2 rig, and I would like to thank him for all his advice on safe and effective practices for my rig renovation.

I would also like to thank Mitsubishi Heavy Industries, and in particular, Dr. Eisaku Ito, and Mr. Akihiro Nakaniwa, for their support of the project and their continued valuable input on the trajectory of the project.

My time at MIT would not have been the same without all my friends, both in my lab and otherwise. To Vincent, Georgi, Andrew, Andras, and the rest of the GTL, you were great study partners, and even better friends. To my friends on the hyperloop team and especially my fellow levitation team members, Philippe and Greg, I am very grateful for you providing a much needed break from all the time spent on research and my thesis. To Leah, thank you for your unwavering love and support through the ups and downs of my time at MIT.

Finally, I would like to thank my parents, Dan and Susan, for their love and support throughout my time at MIT and on my journey here. They both instilled in me a love of knowledge, learning, and exploration, and provided me with the opportunities that allowed me to be where I am today.

Contents

List of Figures

List of Tables

Nomenclature

Acronyms

BOS	Background Oriented Schlieren
CCD	Charge coupled device
CCS	Carbon capture and sequestration
CFD	Computational fluid dynamics
COTS	Commercial off-the-shelf
CP	Critical point
CO_2	Carbon dioxide
DFT	Discrete Fourier Transform
DOT	Department of Transportation
EOS	Equation of state
FEA	Finite Element Analysis
FFT	Fast Fourier Transform
IFFT	Inverse Fast Fourier Transform
LDV	Laser Doppler Velocimetry
NIST	National Institute of Standards and Technology
NPT	National Pipe Thread Taper
PIV	Particle Image Velocimetry
RANS	Reynolds Averaged Navier Stokes
S-CO_2	Supercritical carbon dioxide
SF	Safety Factor
SW	Span-Wagner

VAC	Volts (Alternating Current)
VI	Virtual Instrument (LABView)

Symbols

A	Cross-sectional area
α	mean polarizability
β_p	Volumetric thermal expansion coefficient
c	Speed of sound
c_p	Heat capacity at constant pressure
c_v	Heat capacity at constant volume
δ	Interferometer beam displacement
h	Specific enthalpy
f	Frequency
γ	Ratio of specific heats
k	Wave number
L	Lorentz-Lorenz function
μ	Dynamic viscosity
M	Molar mass (for CO_2)
Ma	Mach number
$\dot{m}$	Mass flow rate
N_A	Avogadro constant
m_s	Isentropic temperature exponent
n_s	Isentropic exponent
p	Pressure
ρ	Density
R	Gas constant
Re	Reynolds number
s	Specific entropy

T	Absolute temperature
τ_{cl}	Condensation time scale ratio
u	Specific internal energy
V	Volume
w	Test section width
Z	Compressibility factor

Subscripts

c	Critical condition
D	Diameter
L	Axial length
r	Reduced quantity (non-dimensionalized with critical value)
t	Stagnation quantity

Chapter 1

Introduction

1.1 Background and Motivation

With the ever increasing effects of global warming and climate change, the energy industry has been pressured to reduce the emission of carbon dioxide (CO_2) and other greenhouse gasses . Despite the increasing use of solar, wind, and other renewable energy sources, along with cleaner burning natural gas power plants, coal is still the most widely used fuel for electricity generation, accounting for 33% of the energy produced and over 71% of the CO_2 emissions in the United States.[22]. Carbon Capture and Sequestration (CCS) has been proposed as a means to slow the progress of climate chance by trapping CO_2 emissions from coal and other hydrocarbon-fired power plants in underground aquifers, preventing the harmful greenhouse gasses from entering the atmosphere. While this is not a sustainable solution to global greenhouse emissions, it serves as a stopgap until renewables and other clean power options can mature and proliferate. One of the key enabling technologies for CCS is the development of CO_2 compressors operating near the critical point.

The critical point of CO_2 is 304.1 K, 73.8 bar. Above these pressures and temperatures, vanishing surface tension causes it to become a single homogeneous mixture with no distinct liquid and gas phases. In this state, CO_2 has densities similar to those of a liquid (of order 1000 kg/m^3), but has the compressibility of a gas. This is illustrated graphically on a pressure-temperature phase diagram in Figure 1-1.

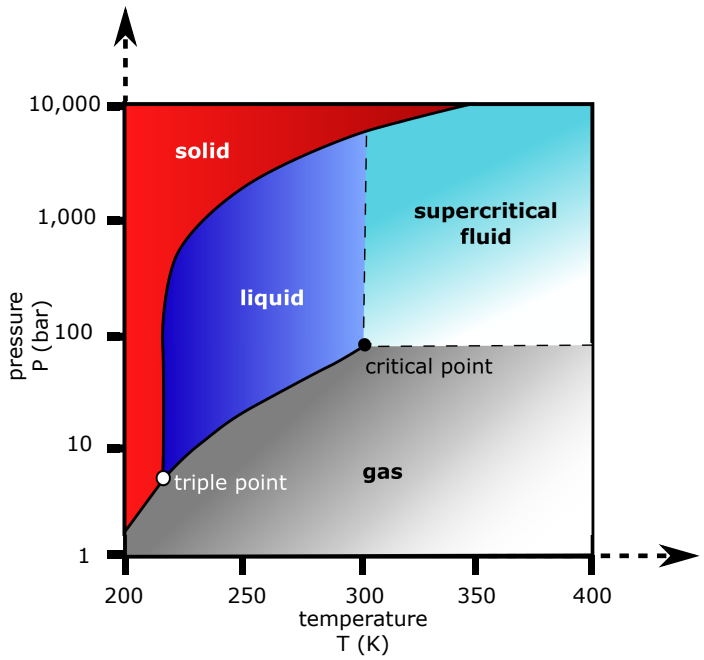

Figure 1-1: Phase diagram for CO_2 showing supercritical region in upper right-hand corner. Credit: B. Finney, M. Jacobs. 2010

Another application for S-CO_2, similar to CCS, is enhanced oil recovery (EOR). CO_2, usually from a power plant, is compressed to pressures as high as 700 bar before being injected into previously inactive oil wells. The CO_2 reduces the viscosity of the oil, allowing for it to be more easily pumped to the surface. This technique allows for oil wells to produce up to 50% more oil than using traditional pumping techniques.[3]

S-CO_2 for power cycles is also being considered as an alternative to the aging steam Rankine cycle which has served as the backbone of the global power generation industry since the late 19th century [36]. S-CO_2 Brayton and Rankine cycles have the possibility of demonstrating efficiencies of almost 50% compared with typical steam Rankine efficiencies of 30-40%.[6] In addition to the efficiency benefits, the high densities of S-CO_2 result in an order of magnitude increase in the power density of turbomachinery when compared with traditional steam turbines making it attractive for applications with stringent space constraints.

1.2 Problem Statement

Stable and efficient operation close to the two-phase region is desirable for super-high pressure CO_2 compressors used for CCS and EOR. The key benefits are reduced overall power requirements via lower stage inlet temperatures, and increased power densities through the high densities of CO_2 near the critical point [41]. In multi-stage compressor for EOR or CCS, this drives the later stage inlet temperatures towards the critical point. This can be seen in the vicinity of the 4th stage inlet to the critical point on the T-s diagram illustrated in Figure 1-2.

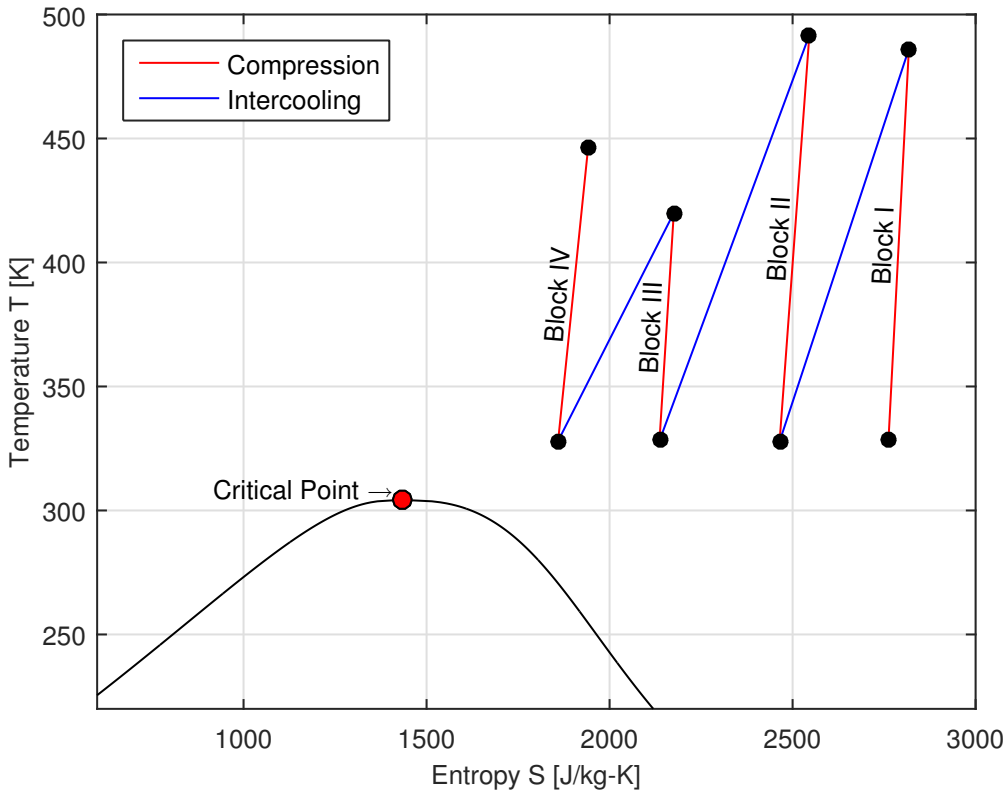

Figure 1-2: T-s diagram of a typical multi-stage centrifugal compressor for CCS or EOR. Note the decreasing distance from the vapor dome from stage I to IV

During testing near the critical point in a representative compressor, reduced efficiency and stability issues were observed [8]. Due to the lack of experimental data and accurate modelling of S-CO_2 in this region, a relatively conservative empirical safety boundary was established limiting the minimum inlet temperature for the compres-

sor. The implementation of the safety boundary eliminated these issues, but further work was required to rigorously define this boundary and push it as close to the vapor dome as possible. Computational and experimental work in the MIT Gas Turbine Lab indicated that the compressor could be safely operated at significantly lower inlet temperatures than were indicated by the original safety boundary. A new computationally derived safety boundary was produced and was used to establish a new set of operating parameters for the compressor. The compressor was successfully run at operating points established by the computationally derived safety boundary [50]. Both these safety boundaries along with successful operating points for the compressor are indicated in Figure 1-3. Despite this success, a rigorous experimentally derived limit on compressor operation had not been established before this research.

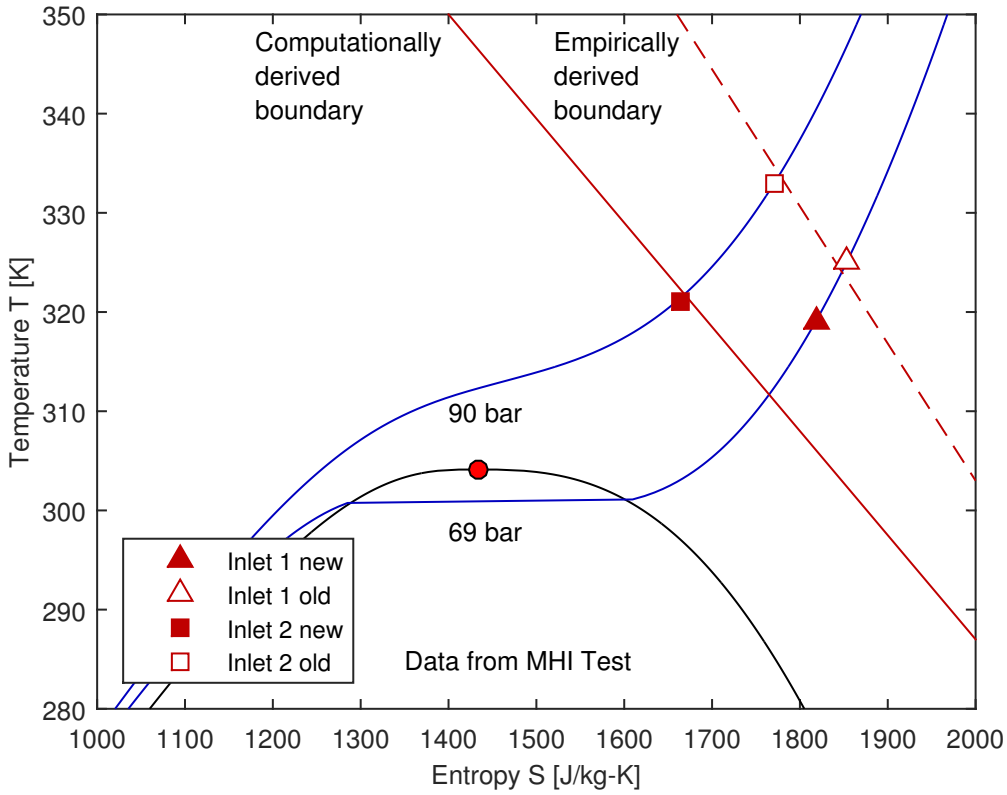

Figure 1-3: T-s diagram illustrating both the old and new inlet condition safety boundaries as well as successfully demonstrated operating points defined by the new safety boundary

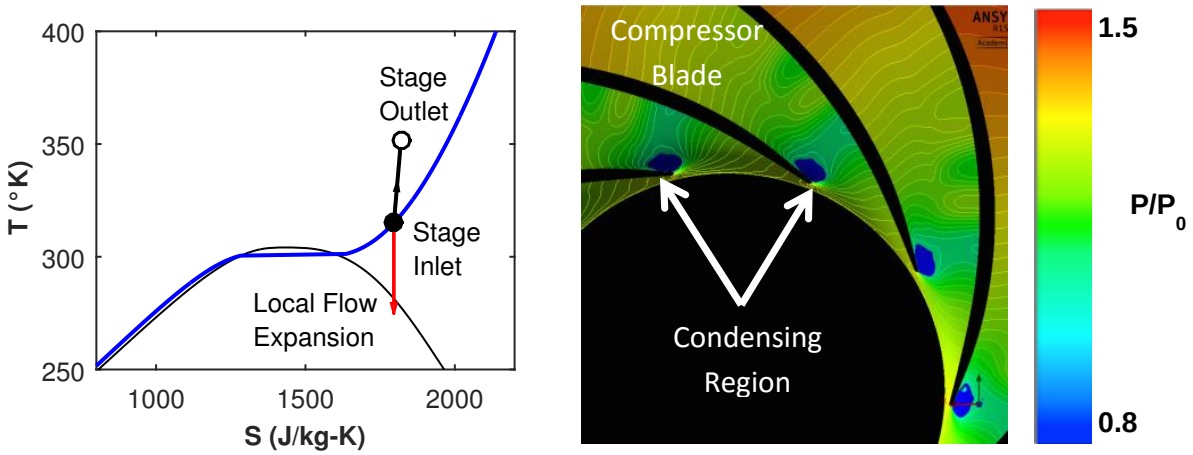

(a) T-S diagram of local flow expansion over leading edge

(b) T-S diagram of local flow expansion over leading edge

Figure 1-4: Condensation near the leading edge of a compressor impeller operating near the two-phase dome

1.3 Challenges

While the bulk fluid properties in S-CO_2 compressors generally remain single-phase, flow acceleration near the impeller blade leading edges can result in localized excursions into the two-phase region [41], [29]. Figure 1-4 illustrates this behavior in a T-s diagram. While two-phase modeling is usually applied to investigate the internal flow behavior in turbomachinery with saturating fluids, a key feature of S-CO_2 compressors allows for the use of single-phase calculations, greatly simplifying the numerical approach. The rapid rate of expansion, and subsequent rapid compression, make the phase change process fundamentally non-equilibrium.

A previous scaling analysis defined a non-dimensional parameter based on the ratio of through flow time to nucleation time to assess under what conditions condensation would occur. At the leading edge of a typical compressor blade, this ratio is of order 10-4, indicating that the nucleation time is much longer than the residence time of a fluid particle, and that condensation is not likely to occur [29]. Further supporting the hypothesis that single-phase calculations can be successfully used is the small relative size of the regions where condensation could occur. Several studies in the literature, for example [29] and [41], suggest that the extent of the condensation region is of the

order of 1% of the blade chord.

During rapid cooling, the fluid enters a metastable state where it continues to behave like a gas until the stability limit, the so called Wilson line, is reached, or there is sufficient nucleation to initiate bulk condensation [19]. This non-equilibrium process, graphically represented in Figure 1-5, is difficult to measure and an accurate characterization of the meta-stable thermodynamic properties remains a key challenge.

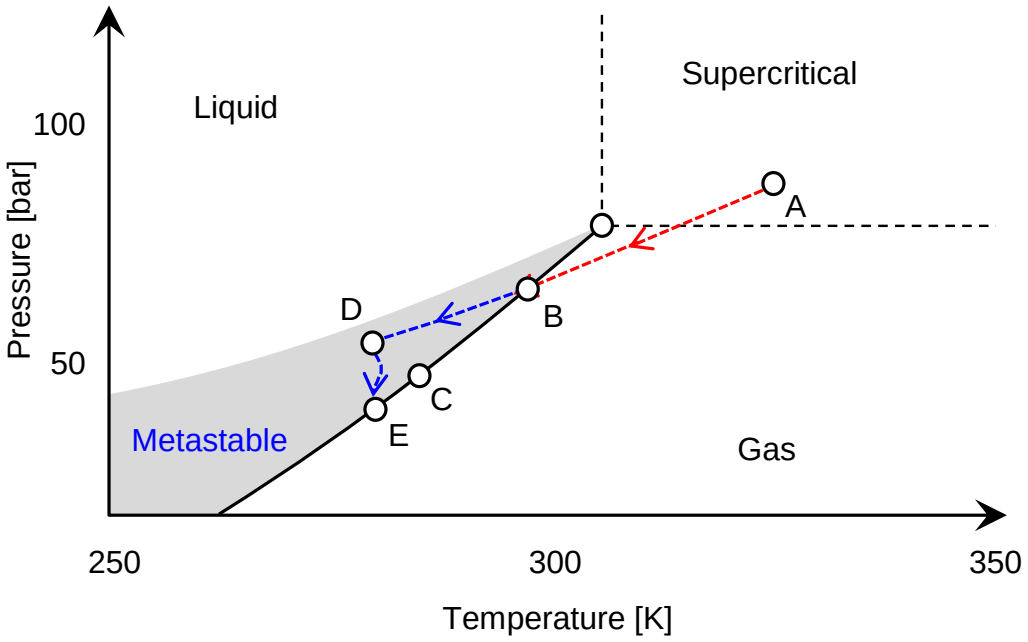

Figure 1-5: Pressure temperature diagram illustrating the difference between equilibrium and non-equilibrium phase change during an expansion. The short time scales typically encountered in compressors lead to fluid following path A-B-D rather than the equilibrium process A-B-C.

A limited amount of work has been reported in the literature on metastable CO_2, especially near the critical point. Away from the critical point, the equilibrium and metastable vapor can be modelled as an ideal gas. This was demonstrated in [15], where non-equilibrium condensation of CO_2 at pressures of one order of magnitude lower than those seen in an S-CO_2 compressor was studied. In [21], a general numerical methodology for determining thermal choking due to finite rate (non-equilibrium) condensation for an ideal, calorically perfect vapor in high speed flows was outlined.

Near the critical point, however, CO_2 exhibits significant non-ideal behavior and these approaches have limited applicability to S-CO_2 compressors design [7].

1.4 Current State of the Art for Characterization of Metastable Fluids

Much effort has been put into accurately characterizing the metastable state of water vapor due to its prevalence as a working fluid in the power generation industry. For example in 1997 the International Association for the Properties of Water and Steam (IAPWS) released the most widely used collection of tabulated steam properties. A dense-gas EOS was extrapolated into the metastable vapor region to establish the thermodynamic properties. Despite this, there is still no experimental data with which to compare the extrapolated properties [42]. The state-of-the-art representation of the real-gas properties of CO_2 is the Span and Wagner (SW) model. NIST RefProp uses this formulation to calculate equilibrium properties as well as metastable vapor and liquid properties, but again, these values have no experimental basis [47].

Cubic spline extrapolation was used in [29] to extend real-gas properties calculated by the Lee-Kesler Model [27] into the metastable region. Experimental pressure measurements demonstrated good agreement away from the critical point; however, the method broke down at the critical point due to inaccuracies in the extrapolation scheme caused by the large gradients of thermodynamic properties. This extrapolation method, along with a method based on the SW EOS implemented by RefProp, are outlined in detail in Chapter 2.

1.5 Goals and Objectives

The research outlined in this thesis is focused on the characterization of the behavior of CO_2 undergoing non-equilibrium condensation in a high speed flow within the context of high pressure S-CO_2 compressors. The main objectives are:

- Modify, and test the MIT Gas Turbine Laboratory CO_2 blowdown facility to facilitate optical access to the test section and improve run set up time by at least an order of magnitude.

- Demonstrate the use of interferometry as a means of measuring the density of both equilibrium and metastable CO_2 near the critical point.

- Quantitatively determine the accuracy of direct and equation of state (EOS) based extrapolation for determining metastable properties of CO_2.

- Devise experimentally derived guidelines for the prevention of condensation over the impeller leading edge in S-CO_2 compressors.

The potential payoff from this research is to allow for the design and operation of more efficient supercritical CO_2 compressors. The benefits of lower power consumption compressors will push technologies like EOR, CCS, and S-CO_2 power cycles towards economic viability.

1.6 Key Contributions

The primary accomplishments of this research are:

1. Commissioning of a blowdown test facility with a nozzle test section with optical access tested to 150 bar enabling the investigation of metastable CO_2 expansion in a transonic flow near the critical point.

2. Demonstration of the use of interferometry for measuring the density of supercritical CO_2 near the critical point to within 2%, allowing for the assessment of metastable extrapolation schemes.

3. Characterization of EOS based extrapolation accuracy to within 2% in the region of interest for S-CO_2 compressors, enabling the full characterization of the thermodynamic state prior to condensation.

4. First of its kind measurements of the Wilson line for CO_2 at total conditions representative of an S-CO_2 compressor providing insight into the behavior of CO_2 undergoing non-equilibrium condensation.

5. Definition of a new experimentally derived safety boundary for compressor inlet conditions indicating the possibility of increased compressor efficiency through operation at inlet conditions close to the critical point.

1.7 Thesis Organization

Chapter 2 outlines the nature of metastable subcooled vapors and their behavior. It contains a brief description of the Span and Wagner EOS based extrapolation method as well as the tabular extrapolation method used to determine metastable properties for CO_2. Chapters 3, 4, and 5 outline the design of the blowdown rig used to gather all the data included in this thesis. Chapter 3 focuses on the functional design of the rig as a whole with considerations for operating range, reliability, and usability. Chapter 4 covers the functional requirements and design for the nozzle test section describing in detail the design methodology as well as the structural, thermal, and fluid analysis that went into the final design. Finally, Chapter 5 outlines the design and theory of the shearing interferometer which was used to measure density in the test section. Details on the operation of the rig including operating procedures and error analysis are given in Chapter 6. Experimental results are covered in Chapter 7 with a focus on the assessment of the accuracy of metastable properties and the determination of the Wilson line. Chapter 8 summarized the accomplishments of the experiments and includes recommendations for future work and possible improvements to the rig. Appendix A contains all the technical drawings for the components in the test section. Appendix B is a user manual for the MIT blowdown rig in its current form. This includes instructions on how to set up the optics, how to run the rig, and how to post-process the interferometric images.

Chapter 2

Calculating Thermodynamic Properties of Supercritical CO_2

One of the key challenges in modelling the performance of S-CO_2 compressors is accurately modelling the thermodynamic behavior of CO_2 near the critical point. These difficulties in modelling result from the departure of gas behavior from that of an ideal gas. This chapter covers the Span & Wagner equation of state, the state-of-the-art EOS for real gas CO_2, two methods of determining metastable properties for real-gas CO_2, and the tabular lookup method used to calculate these properties in a robust manner.

2.1 Real Gas Behavior

Away from their respective critical points, gasses follow the ideal gas law,

$$p = \rho RT \tag{2.1}$$

The linear relationship between pressure, temperature and density is a result of the molecules being far enough apart to be considered point masses undergoing elastic collisions with no intermolecular attractive or repulsive forces [13]. As the fluid is brought closer to the critical point, the mean free path between molecules becomes

smaller and intermolecular forces begin to cause departures from the ideal gas equation of state.

The key parameter which defines the deviation from ideal behavior is the compressibility factor Z, defined as,

$$Z = \frac{p}{\rho RT}. \tag{2.2}$$

For an ideal gas, Z = 1, but near the critical point (T_c = 304.1 K, p_c = 73.8 bar), the compressibility factor for CO_2 is approximately 0.275 which yields close to a 300% error in density as calculated by the ideal gas EOS. To capture the behavior of gasses near the critical point or saturated vapor curve where real gas effects are significant, modified real gas equations of state were developed.

2.2 Real Gas Equations of State for CO_2

Two main types of real gas equations of state are used to calculate the thermodynamic properties of CO_2, Generalized models which can be adapted to any real gas, and models developed specifically for CO_2 using experimental data.

Generalized Real Gas Models

For typical industrial compressor modelling, generalized real gas models are used. These models can be adapted for modelling many different fluids with compressibility factor typically expressed a function of the reduced quantities (pressure, temperature, and density, non-dimensionalized by their respective critical values) [30]. Generalized equations such as the Lee-Kesler model can be used to accurately model CO_2 showing typical errors less than 2% between pressures of 50-250 bar. Near the critical point, however, deviations from experimental data can reach as high as 5.8% [8].

Specific Real-Gas Model

With significant scientific and industry interest in S-CO_2 there was a need for a more accurate EOS for modelling CO_2 near the critical point. Span & Wagner created

an equation of state specifically for CO_2 that shows significantly better agreement even very near to the critical point. Rather than modifying an existing equation of state as had been done in the past, the Span & Wagner EOS (SW EOS) was a fundamentally new multiparameter equation based on the Helmholtz energy and based specifically on archival CO_2 property data. Further information on this type of EOS can be found in [46].

The equation expresses the Helmholtz energy as a sum of ideal-gas and real-gas parts, the latter of which consists of a 42 term summation based on fundamental chemical behavior and fit to experimental data. The trailing 3 terms of the summation are specifically used to tailor the behavior of the EOS around the critical point leading to much better agreement than with the Lee-Kesler or other generalized Equations of state [47]. The reported errors in density (the primary property of interest for this thesis) is 0.03-0.05% [47].

This equation represents the state of the art in determining properties of CO_2 and is utilized in the National Institute of Standards and Technology Reference Fluid Property Database (NIST RefProp). Despite the accuracy of the SW EOS for equilibrium properties, both the original authors of the EOS and the creators of its implementation in RefProp acknowledge that the accuracy of the equation for generating metastable subcooled vapor data is unknown.[47], [28].

2.3 Calculation of Metastable Properties

As mentioned in Chapter 1, knowledge of the metastable, subcooled vapor properties of CO_2 is required for simplified single-phase calculations for S-CO_2 compressors. There is significant literature on the modelling of steam expansions into the metastable region. for example [23] and [51], but there is very little published work on metastable CO_2.

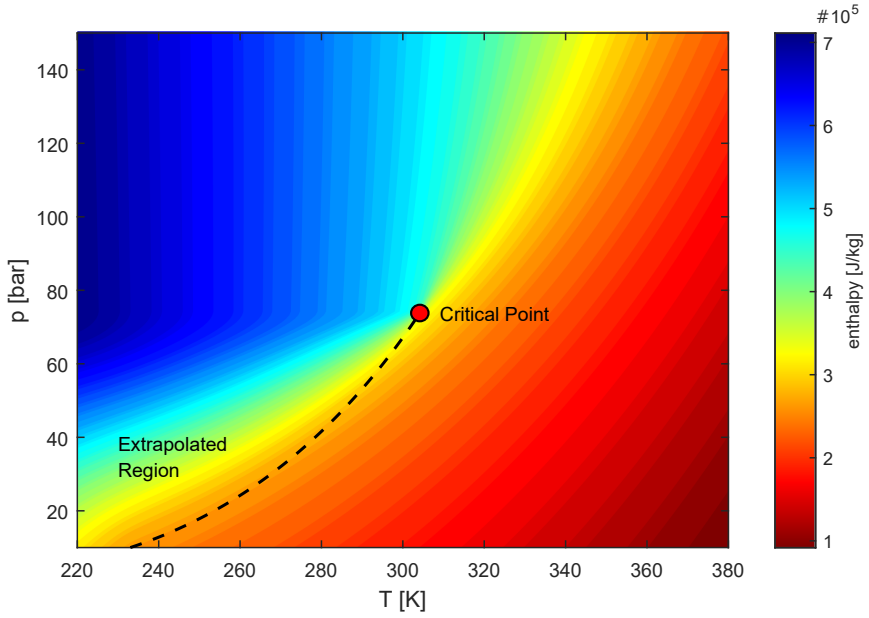

Figure 2-1: p-T contour plot of enthalpy with the metastable properties generated by a spline-based extrapolation method

Tabular Extrapolation from Equilibrium Properties

Due to the complexity of extrapolating the Span & Wagner EOS, a simpler extrapolation method was implemented for calculations seen in [50], [29], and [7]. This method utilized a cubic-spline based extrapolation of the equilibrium vapor properties across the saturated vapor curve into the metastable vapor region. The extrapolations were performed on tables in pressure-temperature (p-T) coordinates, leading to tables such as that illustrated in Figure 2-1.

For numerical stability, the equilibrium vapor properties were merged into a continuous surface with the equilibrium liquid properties, completely eliminating the discontinuity typically seen at the saturated vapor curve on a p-T plot. This led to large non-physical gradients in the thermodynamic properties for pressures and temperatures far into the metastable region. In addition to the errors caused by the continuity constraint, it should be noted that all thermodynamic properties (enthalpy, entropy, specific heat, etc.) were independently extrapolated into the metastable region with no consideration for the original equation of state. For these reasons, this method is only valid for small excursions into the metastable region.

This extrapolation method was utilized for 3-D real-gas CFD and compared with experimentally derived pressures in a converging-diverging nozzle in [50]. Comparison with experiments showed good agreement away from the critical point (Figure 2-2a), but indicated instability and large errors when a blowdown directly through the critical point was modelled (Figure 2-2b).

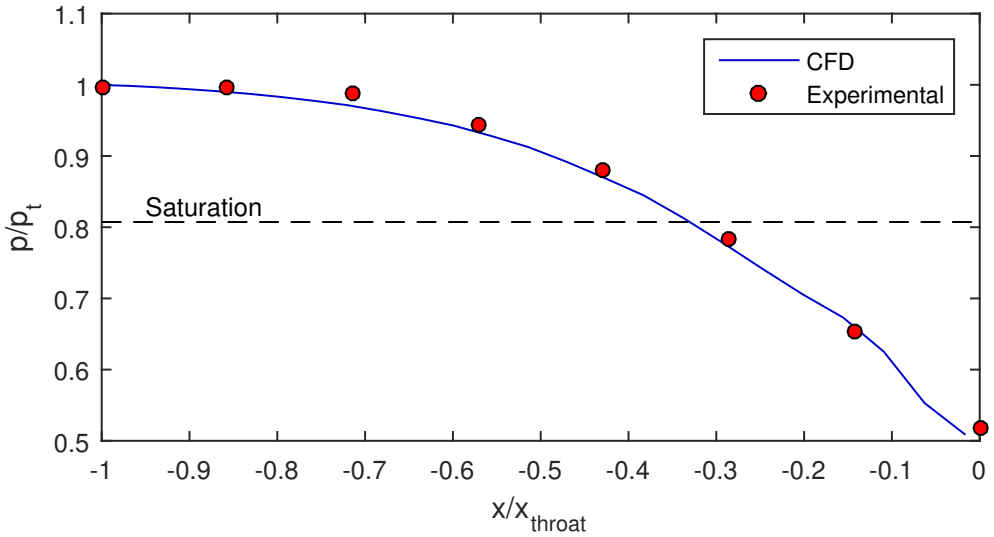

(a) $T_t = 315$ K, $p_t = 89.1$ bar (away from critical entropy)

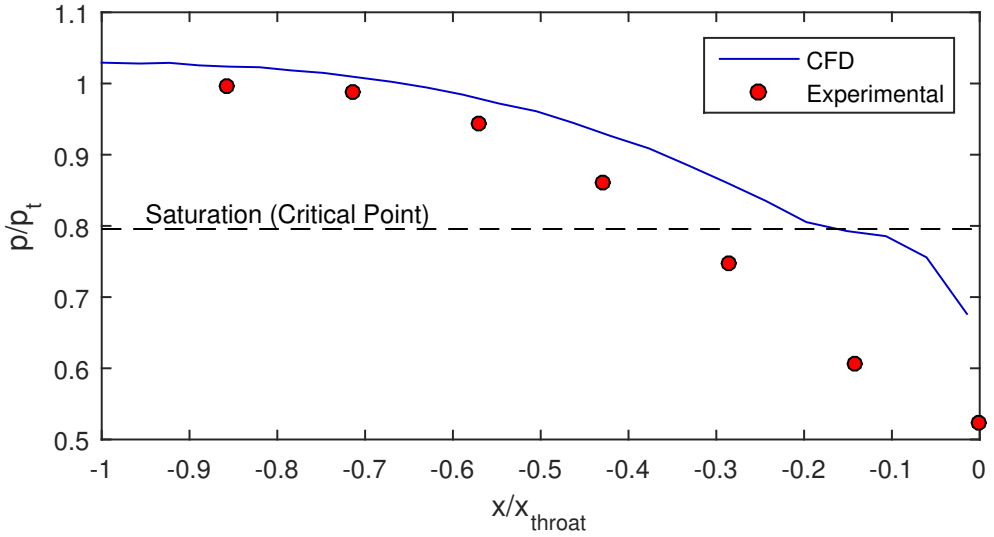

(b) $T_t = 315$ K, $p_t = 95.7$ bar (directly at critical entropy)

Figure 2-2: Accurate modelling using metastable properties away from the critical point (a) and discrepancies between CFD and experiment due to breakdown of the metastable extrapolation method at the critical point (b). (Data Courtesy of Dr. C. Lettieri and D. Yang)

Extrapolation of the Span & Wagner EOS Through RefProp

RefProp has the ability to generate metastable properties for CO_2 through extrapolation of the Span and Wagner EOS. This is accomplished by forcing the solver to find a vapor solution even when the pressure and temperature are on the liquid side of the saturated vapor curve. There is a numerical limit beyond which a converged solution cannot be found, known as the spinodal limit. This limits the practical region of metastable properties which can be calculated from an extrapolated EOS. Figure 2-3 illustrates metastable enthalpy as extrapolated by RefProp as well as the sharp discontinuity at the spinodal limit.

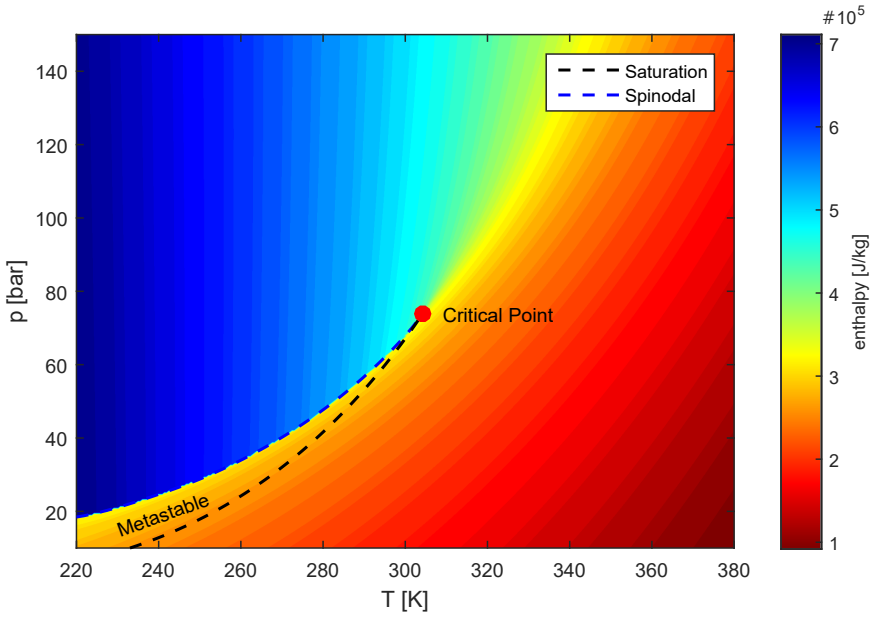

Figure 2-3: Metastable enthalpy values extrapolated through RefProp using the SW EOS

2.4 Table Lookup Method for Metastable Properties

Due to the formulation of the RefProp subroutines, metastable properties can only be calculated for pressure and temperature inputs. For the modelling of nozzle flows, it is beneficial to have the ability to cross reference any two relevant thermodynamic properties to find a third. Initially, root finding methods were used to find specific

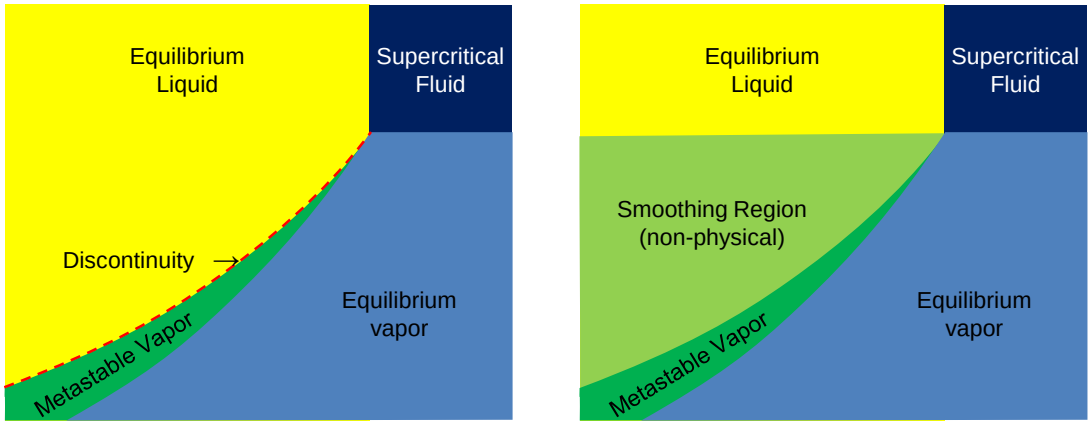

(a) (b)

Figure 2-4: Comparison between a discontinuous (a) and continuous (b) p-T phase map

properties such as density as a function of pressure and entropy for matching pressure transducer measurements to density measured through the interferometer, but this method was unreliable due to the discontinuity in the density and entropy maps at the spinodal.

A robust and generalized interpolated table lookup method was implemented to allow for the calculation of any thermodynamic property available in RefProp as a function of any two independent properties. First, continuous and smooth 2-D tables in p-T coordinates of all thermodynamic properties were created. This was accomplished using a method similar to that of the tabular extrapolation method outlined above, however the extrapolated values start at the spinodal limit rather than at the saturation curve. Figure 2-4 qualitatively shows the various regions of the smoothed tables and Figure 2-5 illustrates the resulting table for enthalpy.

The lookup process is carried out as follows; let a, b, and c denote the two known input and desired output thermodynamic property values respectively and |A|, |B|, and |C| represent the corresponding 2-D tables in p-T coordinates. An isocontour of value a is drawn in |A| and an isocontour of value b is drawn in |B|, yielding all possible points with the desired input property values. The intersection of these contours in p-T coordinates is found and this point value is interpolated on the output map |C| to yield the output $c(a, b)$. This is illustrated graphically in Figure

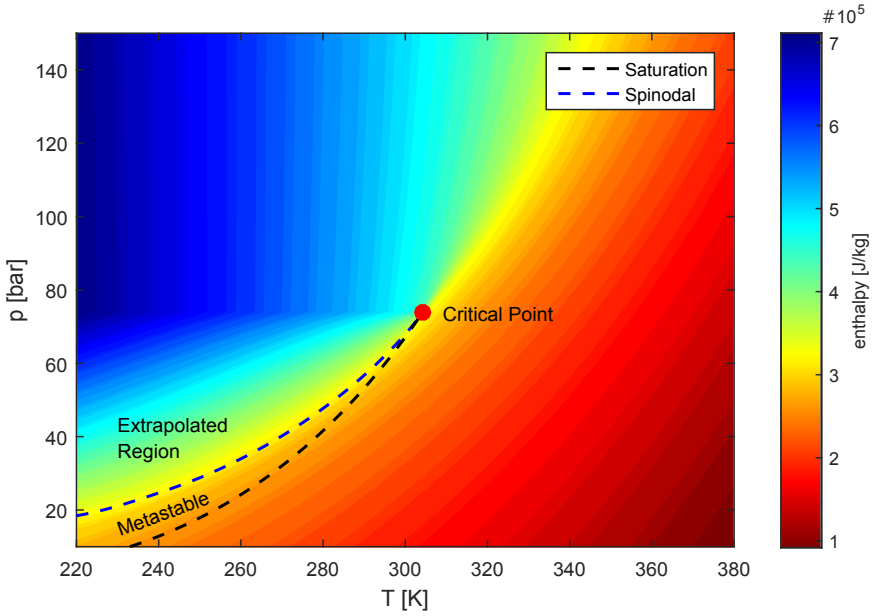

Figure 2-5: p-T plot with a non-physical smoothed region added between metastable vapor and equilibrium liquid properties implements for numerical stability

2-6. For any points in the smoothing region (light green in Figure 2-4) are flagged to ensure that the user is aware they are non-physical and should be disregarded. Near the critical point (reduced temperature and pressure below 1.003) the interpolation method shows errors of up to 5% when compared with RefProp, but it should be noted that the RefProp algorithm itself shows a 3% discrepancy between the accepted value of density and that calculated from the critical temperature and pressure, so errors are to be expected. Outside this region, the lookup method shows errors below 0.03% for all properties.

The following chapters outline the design, construction and testing of an experimental rig meant to evaluate these calculated metastable properties and to observe the behavior of supercritical CO_2 as it undergoes non-equilibrium condensation.

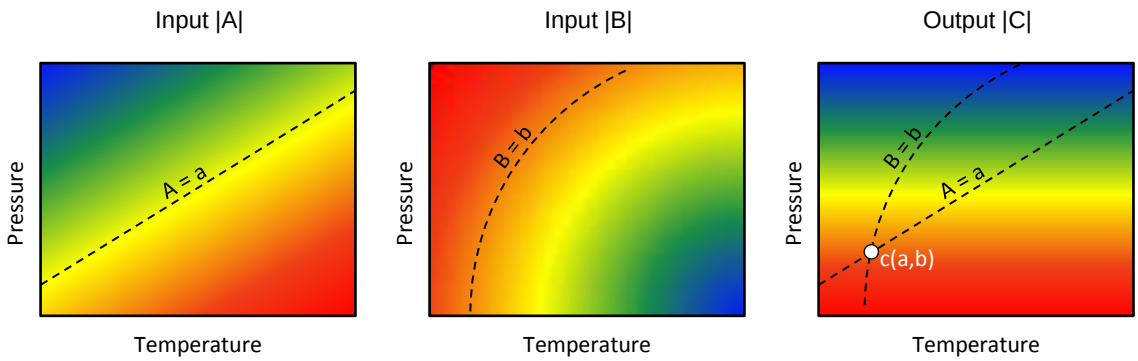

Figure 2-6: Qualitative illustration of the tabular lookup method for calculating metastable properties as a function of properties other than pressure and temperature

Chapter 3

Experimental Test Rig Design

The blowdown test rig that was utilized to gather all the data outlined in this thesis is a successor to the first-generation MIT S-CO_2 blowdown test rig which was constructed and run from 2012-2014 [50]. The first two sections outline the previous test rig and the challenges associated with its operation. The remainder of the chapter covers the design changes and improved capability that were incorporated into the second generation test rig to alleviate these challenges. These changes include a higher pressure and temperature charge tank, improved filling through the addition of a liquid CO_2 transfer pump, and improvements to the control software in LabVIEW.

3.1 First-Generation Test Rig

The first generation test test rig was primarily designed to identify the onset of condensation up to sonic conditions. It consisted of a converging-diverging nozzle instrumented with high-frequency Kulite pressure transducers along the converging section. A schematic showing the basic components and relevant parameters for the first generation test rig can be seen in Figure 3-1. In addition to measuring static pressure, the pressure transducers were mounted as the back face of a Helmholtz resonator such that speed of sound could be measured based on the transfer function between the measured pressure signal and a signal produced by a piezoelectric speaker. This novel technique was successfully implemented for static test cases (no flow) but

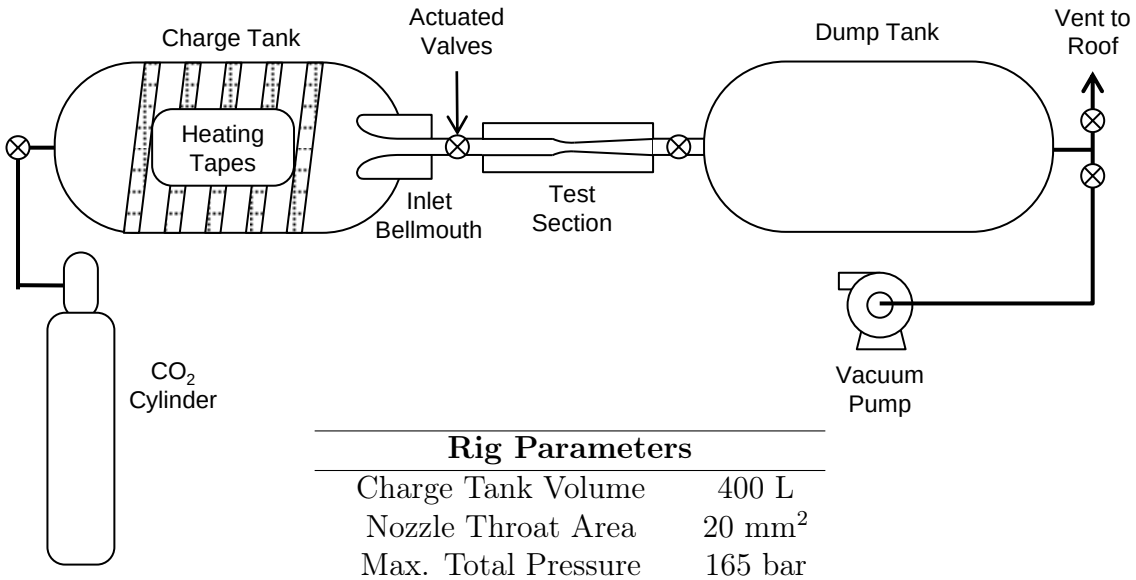

Rig Parameters	
Charge Tank Volume	400 L
Nozzle Throat Area	20 mm^2
Max. Total Pressure	165 bar
Max. Total Temperature	328 K
Typical Blowdown Time	1 s

Figure 3-1: Schematic and relevant parameters of the previous test rig design

was not successful during CO_2 runs with flow.

Blowdown runs with CO_2 were made at 4 different total pressures along a 315K isotherm: 74.4 bar, 78.6 bar, 89.1 bar and 95.7 bar. A more relevant metric for evaluation the total conditions is the reduced entropy (s/s_c). The reduced entropies for the four runs were 1.214, 1.185, 1.080, and 1.000, indicating that the total conditions for run 4 were directly above the critical point. For total conditions away from the critical point (runs 1-3) the pressure transducer data showed no evidence of condensation. These results were confirmed by two-phase numerical calculations. While there appeared to be no evidence of condensation up to sonic conditions in run 4, numerical calculations using extrapolated metastable properties did not agree well with the experimental data indicating errors in the extrapolation or a fundamental misunderstanding of the thermodynamic process through the critical point. These discrepancies between experiment and simulation indicated the need for a more accurate characterization of the metastable properties and lead to the development of a second-generation CO_2 blowdown test rig capable of observing the onset of condensation and fully characterizing the metastable state experimentally.

3.2 Challenges with First Generation Test Rig

The main challenges of the previous rig were with the speed of sound measurement method. While it was capable of measuring speed of sound in the static test section, difficulties in speaker performance and post processing prevented it from measuring speed of sound in a transonic flow. Because of this, the new test rig incorporates optical access to observe the onset of condensation and allow for the use of optical analysis methods for measuring fluid density in addition to pressure transducers for measuring static pressure.

The other difficulties with the test rig were related to the filling and heating procedure. CO_2 for the test rig was stored in 50 pound siphon feed cylinders. These contain CO_2 as a two phase liquid/vapor mixture at room temperature and approximately 60 bar. The cylinders were connected to the initially ambient pressure charge tank and allowed to equilibrate in pressure. The initial pressure differential of 60 bar between the cylinders and the charge tank decreases as the liquid CO_2 flows into and subsequently flash vaporizes in the charge tank until a pressure equilibrium is found. Assuming both the tank and cylinder are isothermal at room temperature, the two will equilibrate after approximately 83 kg of CO_2 have been transferred. This is less than 40% of the CO_2 mass required for a blowdown run directly over the critical point. Higher fill levels were achieved by creating a temperature differential between the bottles and the tank, but this resulted in filling rates on the order of days. Due to the filling procedure being highly dependent on the tank pressure, once the tank was heated, it would have to be allowed to cool to room temperature before any additional CO_2 could be added. This prevented subsequent runs at increasing total densities.

The rate at which the tank could be heated was hindered by a technicality in the tank specifications from the manufacturer. DOT tanks are rated for 55°C since that is the temperature at which the maximum allowable vapor pressure is tested for liquefied gas cylinders as per 49 CFR 173.301a and the manufacturer was unwilling to certify the vessel at a higher temperature. Because of this temperature limitation, the heating tapes could only be used at approximately 25% of their maximum power,

leading to heating times on the order of hours.

3.3 New Test Rig Design and Capability

While many of the smaller components and operating procedures changed, the majority of the basic test rig parameters (tank size, blowdown time, nozzle size, etc.) remained constant or similar from the first to the second generation test rig. For details on the tank sizing, and the heat transfer characteristics of the test rig see [50]. The main change required for the second generation test rig was the addition of the new optically-accessible test section. In addition to this new capability, three main goals for improvement in general test rig operation were identified to alleviate the issues with the previous generation test rig. The goals are as follows:

- Reduce setup time before and between runs by at least an order of magnitude
- Streamline operating procedures through automation
- Increase reliability

The changes implemented on the test rig to achieve these goals are outlined in Figure 3-2. The new charge tank and mixing impeller were installed to reduce heating times, increase the operating range of the test rig, and increase reliability. The filling time, and therefore the setup time, were reduced through the installation of a liquid CO_2 transfer pump and the change to bulk Dewar storage. Not pictured in the diagram is the new LabVIEW VI which incorporates automatic calibration and direct logging of data as calibrated channels rather than as raw voltages. Due to its complexity, details on the design of test-section are not included here and are instead included in a dedicated Chapter (4).

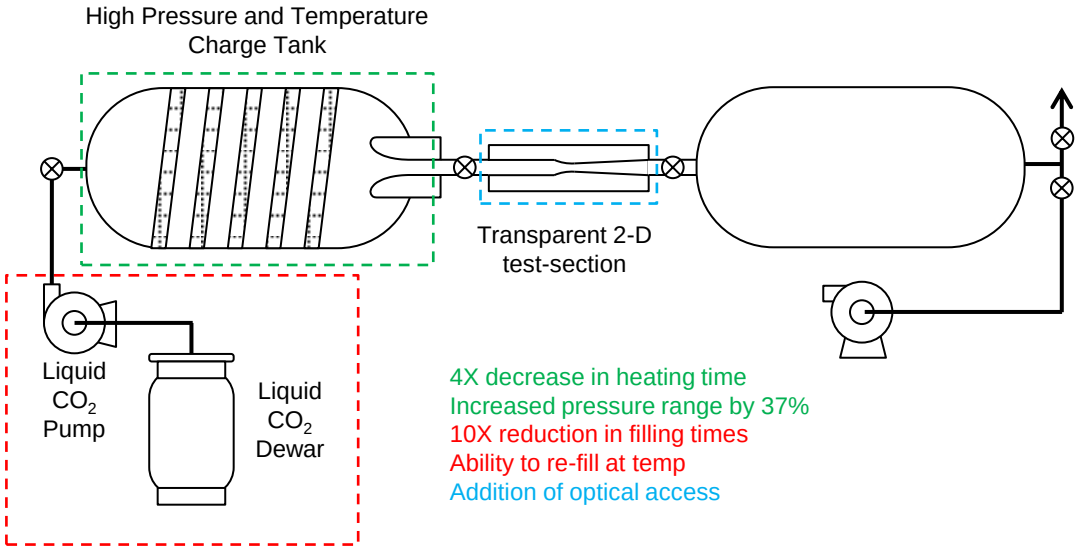

Figure 3-2: Schematic for the second generation test rig showing areas of improvement

3.3.1 Custom Charge Tank

The key specification for the a new charge tank was an increase in temperature capability. An allowable temperature of at least 380 K was specified in order to decrease heating times by a factor of 5 from the first generation rig. It was determined that a custom ASME tank was the only option for a vessel designed for the necessary temperatures and pressure. To reduce lead-time and cost, the tank was formed by cutting to length, and then re-spinning, one end of an existing tank. The only tank available from FIBA was rated for 275 bar at 300 K and 236 bar at 588K, leading to an additional 2X safety factor above the safe operating pressure. The increased wall thickness reduced the internal volume by 9% and doubled the tank thermal mass and weight. Due to temperature limitations on the insulation used on the heating tape connections, the tank operating temperature was set to 380K. To avoid the risk of overpressurization, the pressure operating limit was reduced to 150 bar.

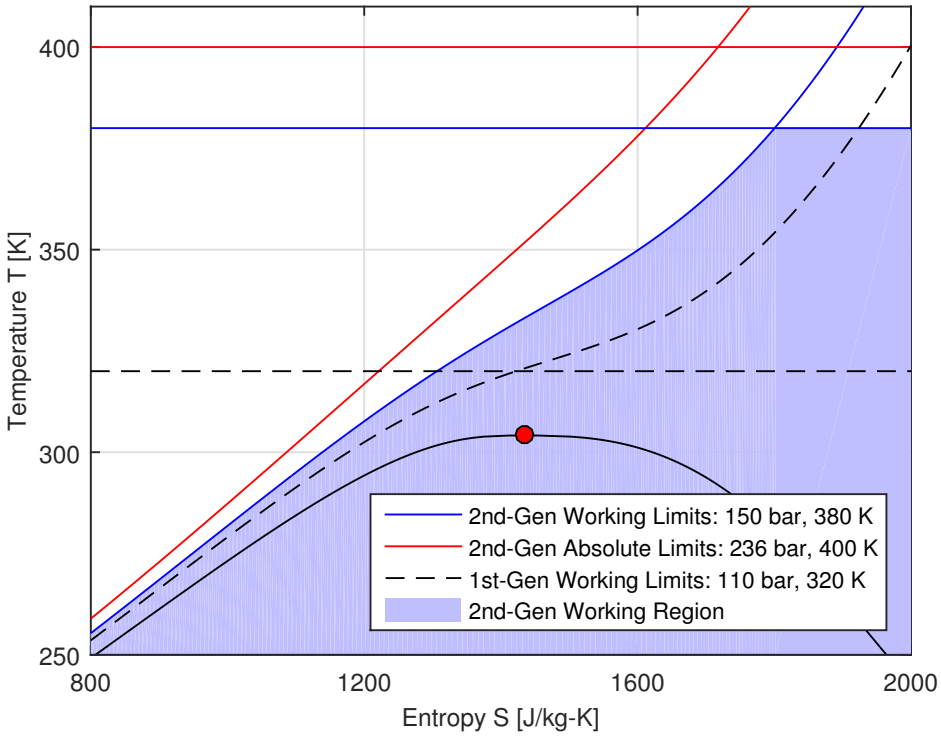

Figure 3-3: Comparison of the tank limitations for the first and second generation blowdown test rig showing 40% and 20% increases in pressure and temperature capability

In addition to the improved temperature and pressure limits, the installation of the heating tapes was modified to reduce heating time and temperature stratification within the tank. In the previous test rig, the heating tapes were wound in a spiral around the tank, creating 3 independently controlled heating zones spaced in the axial direction. Temperatures in the tank are typically stratified in the vertical (radial) direction due to the thermal mass and latent heat of the liquid region at the bottom of the tank when it is heated from a two-phase mixture into a supercritical fluid. For the second generation test rig, the tapes were wrapped axially in three meridionally spaced heating zones. The heating zones and the installed heating tapes are illustrated in Figure 3-4 The original 208V three bank VARIAC test rig was retained from the first generation test rig.

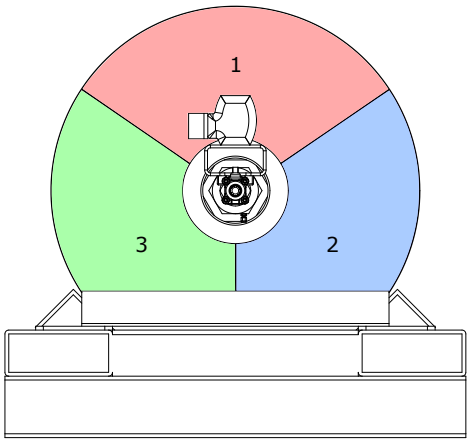

(a) meridionally spaced heating zones

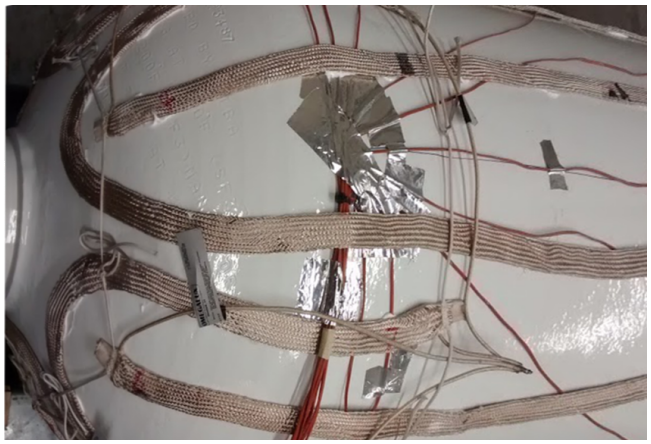

(b) Installed heating tapes

Figure 3-4: Modified heating tape installation which minimize tank stratification to 5K during heating

3.3.2 External Mixer Motor

Another cause of stratification within the tank in the first generation test rig was an undersized mixing impeller. The original mixing impeller was restricted to a diameter of 48mm in order to be able to pass through the 2" NPT fitting at the end of the tank. This selected 30mm impeller was directly driven by a DC motor which was housed inside the tank. to move the impeller away from the bellmouth and motor, a 30cm shaft extension was attached between the motor and impeller. This put stresses on the motor bearings causing them to prematurely fail. The failure of the motor was exacerbated by the supercritical CO_2 environment in which it was required to operate.

A new impeller and motor setup was designed to eliminate both issues. A 20cm impeller was chosen based on the tank size and guidelines from literature on industrial fluid mixing [37]. To achieve this size while maintaining the same <48mm installation footprint for entering the tank, a folding impeller was designed which could collapse down to 45mm and expand to 20cm when inside the tank. Both centrifugal force and blade loading push the folding blades toward their extended positions when the impeller is spun. A comparison between the impeller sizes is shown in Figure 3-5. The design for the impeller was based on an off the shelf design, but was custom made

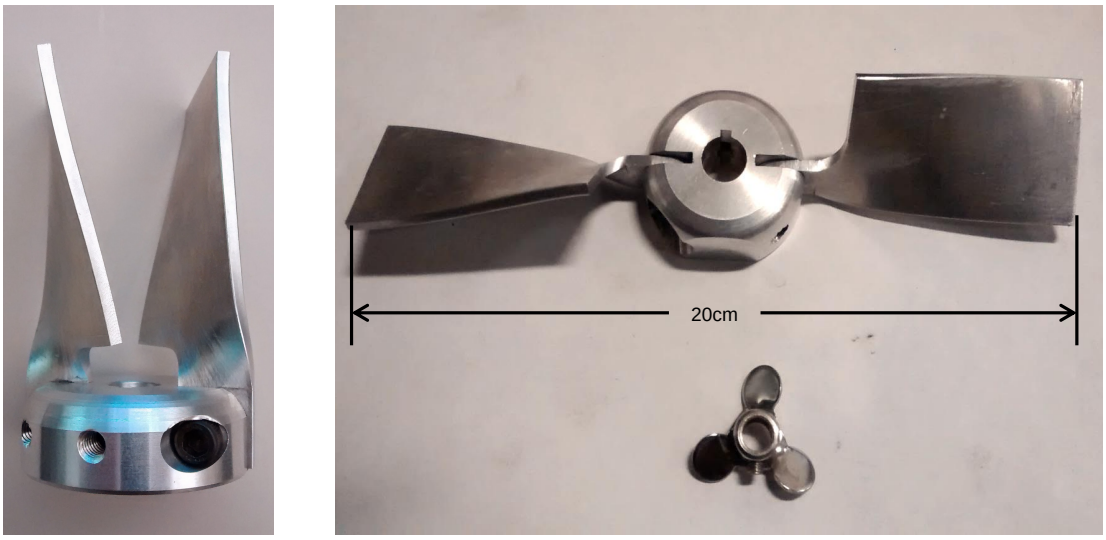

(a) (b)

Figure 3-5: Folded impeller (a), and comparison of Second and first-generation mixing impellers (b).

in-house to switch from stainless steel to aluminum to reduce mass by a factor of 3. The weight reduction increased the natural frequency of the shaft-impeller assembly allowing for either a longer shaft or higher rotational speeds.

A Teflon lip seal was used to provide a rotary pass through between the up to 150 bar pressure in the tank and the 1 bar pressure outside. This allowed the motor to be placed outside the tank and away from the S-CO_2 environment. The shaft diameter was chosen to be 13mm (1/2") to keep surface speeds at the design speed of 1000rpm below the maximum allowed by the lip seal at the design pressure of 150 bar. The shaft was mounted in a dedicated set of axial and thrust bearings to provide a rigid support system, and to eliminate transverse and vertical moments on the motor shaft and bearings. The bearings and seal were installed in a custom machined stainless steel housing which was threaded into the tank through the 1" NPT female threads in the rear tank bullplug. A 1/4" NPT female port was tapped into the bottom of the bearing housing to allow it to double as the inlet for liquid CO_2 from the pump. A CAD cutaway of the design is shown in Figure 3-6. Using the known mass of the impeller and shaft stiffness, he first resonant mode of the shaft-impeller system was calculated for various shaft lengths. The length of the shaft was set at 40cm such

that the first resonant mode of the assembly was half the design speed of 1000rpm.

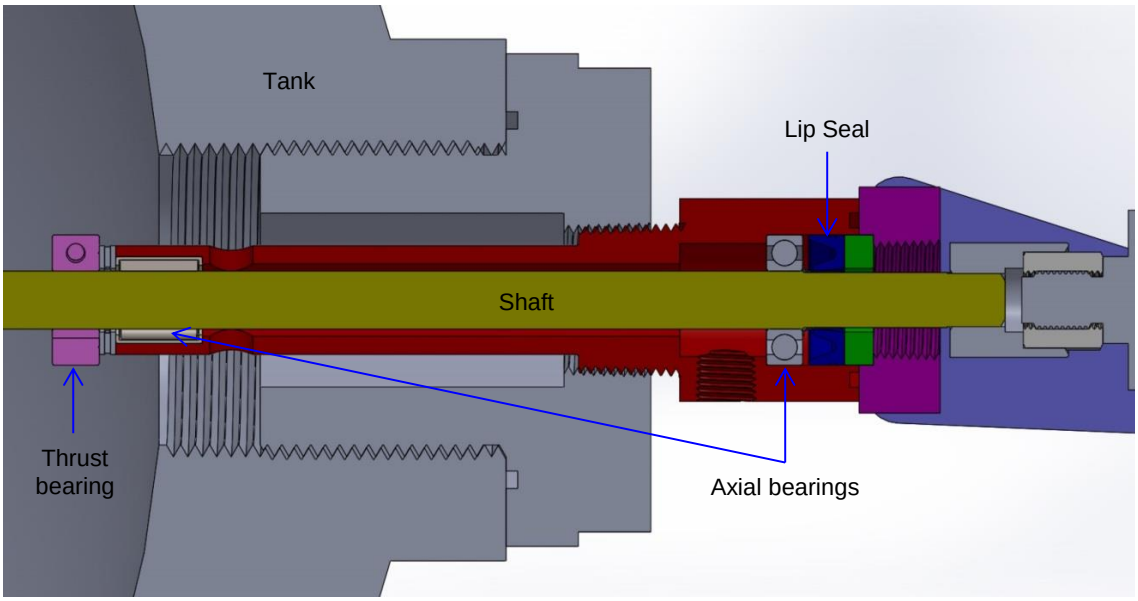

Figure 3-6: Cutaway view of the mixing impeller bearing and seal mount showing the axial and thrust bearings and the CO_2 inlet path

Using mixing impeller power correlations from [18], a motor power requirement of 500W at 1000 rpm was calculated. To satisfy this requirement with at least a two-fold safety factor, a 1200rpm 750 W electric drill motor was chosen. to allow for variable speed, the motor was hard wired to a 120VAC VARIAC mounted to the main control panel. To achieve a simple connection to the motor without marring the shaft surface and subsequently ruining the expensive lip seal during assembly and disassembly, an off-the-shelf machinable shaft coupling with one smooth-bored end for the shaft and one threaded end to fit on the chuck mounting threads of the drill was modified in-house.

After approximately 50 runs, the mixer motor seized. After disassembling it was found to be caused by the thrust bearing cage grinding against the shaft due to a lack of radial constraint. Further exacerbating this problem was the fact that the thrust bearing was run without lubrication inside the S-CO_2 environment of the tank. To alleviate this issue, the thrust bearing was relocated to a new bearing housing bolted behind the main seal/bearing cap outside the tank. Since the thrust bearing was installed outside the tank isolated from the S-CO_2, it could be run in an oil bath.

Figure 3-7: Mixer motor assembly outside the tank

Figure 3-8: Mixer motor Installed in the tank bullplug

A 30mm ball thrust bearing with a two-fold increase in axial load capacity over the original 24mm needle thrust bearing sized to pass through the 1" NPT inlet was used. To date, this new bearing has performed without issue. Figure 3-9 shows the comparison between the old and new design.

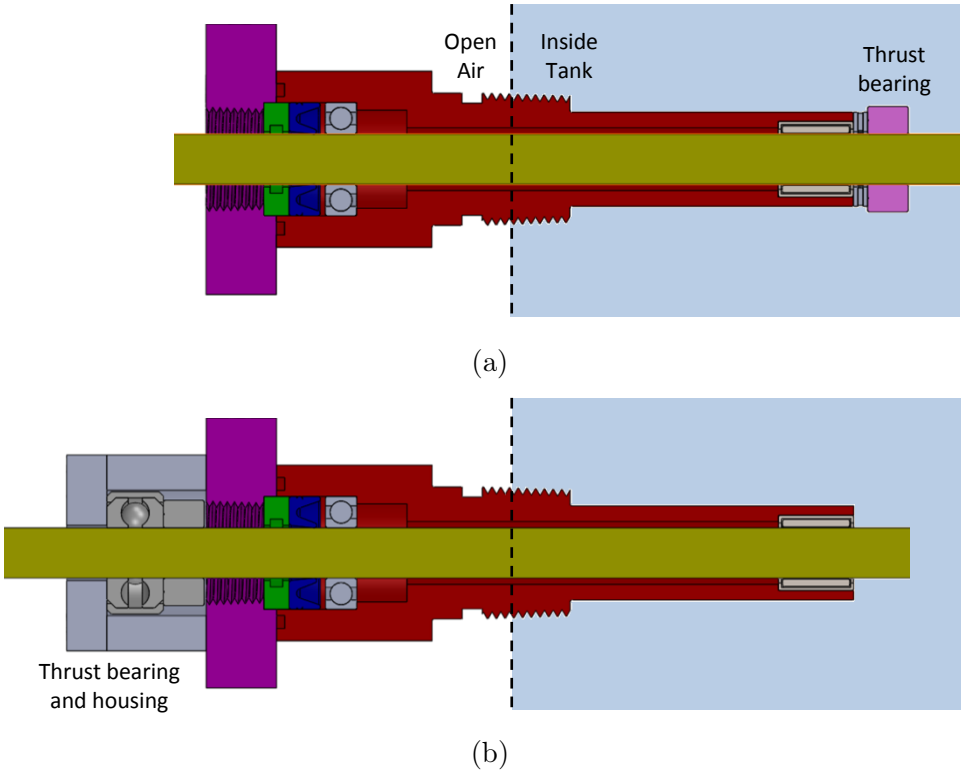

Figure 3-9: Comparison between old thrust bearing mounted inside tank (a), and new thrust bearing placement in an external oil bath (b) designed to alleviate seizing issues

3.3.3 CO_2 Transfer Pump

To alleviate the issues with filling from CO_2 cylinders outlined in Section 3.2, a method of pumping the CO_2 into the charge tank was investigated. The goals were to achieve an order of magnitude decrease in the fill time required for a critical point run and to provide the ability to re-fill an already heated tank without having to wait for it to cool to ambient. Two types of pumps were considered: pneumatic booster pumps and electric piston pumps. A booster pump uses a large pneumatically driven piston to drive a smaller piston which pumps the working fluid, effectively magnifying

the input pressure. While this design would have been simple to connect, requiring only a compressed air connection, a pump with the capability of delivering the outlet pressure of 150 bar necessary to fill a heated tank near the critical point could not be found.

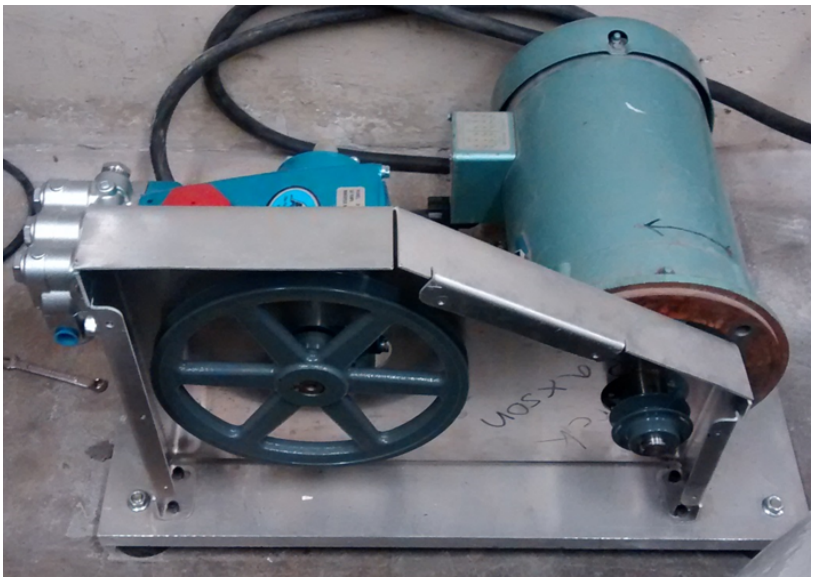

Figure 3-10: CAT 310.CO2 pump mounted to the base along with the motor

An electrically driven piston pump was chosen instead. The pump chosen was a 310.CO2, a COTS option from CAT pumps designed specifically for liquid CO_2. The pump was purchased without a motor and a simple base was made to mount the pump, the separately sourced drive motor and the belt guard to cover the v-belt drive. The motor was a 5hp 3-phase AC motor controlled with a variable frequency motor drive to allow for variable speed operation. The maximum allowable inlet pressure for the pump was 35 bar, preventing the use of standard siphon feed cylinders to store the CO_2. Because of their reduced storage pressure, a cryogenic liquid Dewar was used instead. Liquid CO_2 Dewars store CO_2 in a vacuum insulated tank at approximately 270K and 30 bar. In addition to being within the allowable range for the pump, the Dewar allowed for almost an entire tank of CO_2 to be stored in one container (190L).

In order to determine how much CO_2 was being pumped into the tank, the charge tank frame was mounted on a tripod of two spherical bearing pivots and a load cell effectively turning the tank frame into a lever of known length with force measurement

at one end. This allowed a single load cell to be used rather than having to mount and calibrate 3 or four load cells. images of the installation are shown in Figure 3-11. Due to the mass of CO_2 being only nominally 10% and maximally 20% of the entire tank mass, the accuracy of this weighing method ranged from 0.5-4% depending on the fill level. Regardless, it greatly simplified the filling procedure which was previously to over-fill and purge to the desired temperature and pressure.

(a) Beam Load cell (b) Spherical bearing tank mount

Figure 3-11: Load cell and pivot used to mount the charge tank such that the mass of CO_2 added could be measured

3.3.4 Tank Bellmouth and Thermocouple Mounting

One of the main sources of unreliability in the first generation test rig was the bellmouth. In the original design, the bellmouth was threaded directly into the 2" female NPT threads of the tank bullplug. This required the removal of the test section to allow rotation of the bellmouth. NPT threads are generally meant to be a single-use pressure connection so every removal and re-installation of the bellmouth created opportunities for the introduction of leaks. A liquid thread sealant was used to prevent such leaks, but its thread-locking properties made removal even more difficult, requiring up to 1500N·m for removal.

In addition to the sealing issues caused by removal of the bellmouth, there were

significant difficulties caused by the electronics and thermocouple internal to the tank. 8 wires and thermocouple had to pass through the bellmouth into the tank: 4 for the internal Kulite, 2 for the mixer motor, and 2 for the speakers. All these wires had to pass through a multi-cord sealing gland before taking an approximately 100° sharp bend inside the bellmouth. The shape of this pass through is shown in Figure 3-12. The wires were prone to being cut by the sharp edges of the pass through and it the process of forcing the 1/16" diameter stainless steel sheathed thermocouple through the sharp bend was prone to failure.

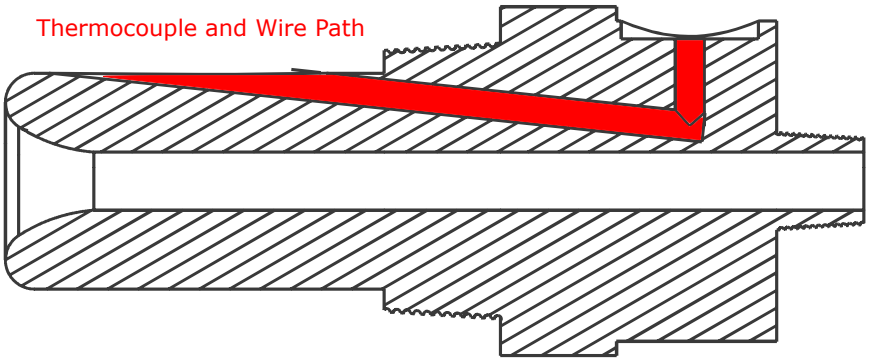

Figure 3-12: midplane cross-section view of the first generation bellmouth showing the sharp cable and thermocouple pass-through which caused routing issues

This majority of these issues were solved in the second generation design by eliminating the Kulite, mixer motor, and speaker inside the tank. The motor was mounted outside the tank as outlined in Section 3.3.2, and the high frequency response of an in-tank pressure transducer was no longer necessary, allowing the new total pressure sensor to be mounted outside the tank. Without the wires, the only connection which had to be passed into the tank was the thermocouple. A 1/16" NPT female port was drilled into the bellmouth allowing for a 1/16" stainless steel Swagelok fitting to be mounted. The fitting was swaged onto the sheath of the thermocouple, providing a leak-proof but removable sealing interface. The mounting of the 1/16" fitting can be seen in Figure 3-13.

To prevent the Issues with repeatedly threading and unthreading the 2" NPT bellmouth mounting feature. a 2" NPT to Swagelok fitting was adapted to serve as

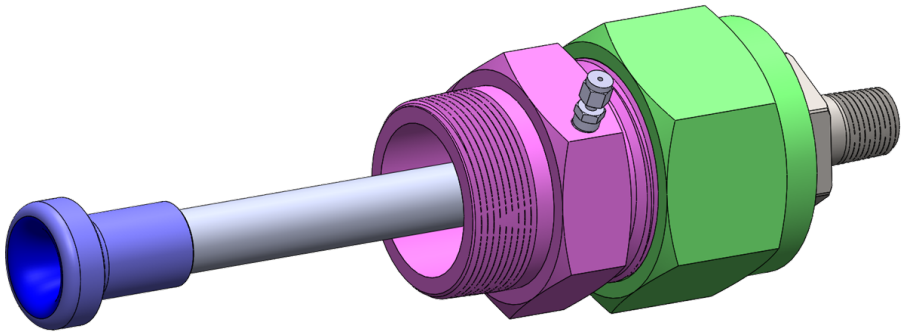

Figure 3-13: New bellmouth mounting design incorporating a 2" Swagelok fitting for easy removal and a smaller Swagelok tapped into the hex for thermocouple mounting

the interface between the tank and the bellmouth. A Swagelok ferrule was swaged onto a custom adapter/bellmouth assembly (grey/purple). This piece and the fitting base (pink), remained stationary while the Swagelok nut (green) was unthreaded. This allowed the wires and the thermocouple to remain permanently attached to the tank during bellmouth assembly and disassembly.

3.3.5 LabVIEW Virtual Instrument and Electronics

To simplify operation and increase reliability, the majority of the test rig electronics were re-wired and the main LabVIEW program was re-written to incorporate more functionality and automation. The Kulite amplifiers, National Instruments data acquisition module, power electronics for the mixer motor and valves, and a new rack-mounted control computer were all mounted in a rolling electronics rack. To simplify connectivity and control, the rack mounted computer is controlled remotely through remote desktop from either another desktop computer in the lab or a laptop outside the test cell. With this setup, all the LabVIEW control and data acquisition connections are confined to the rack.

The main change in functionality for the VI was the addition of automatic calibration of the Kulite pressure transducers in the nozzle. A pressure transducer with built in amplification and 0.08% combined nonlinearity hysteresis and drift was installed in the tank. Actuated valves were installed at both ends of the test section allowing for

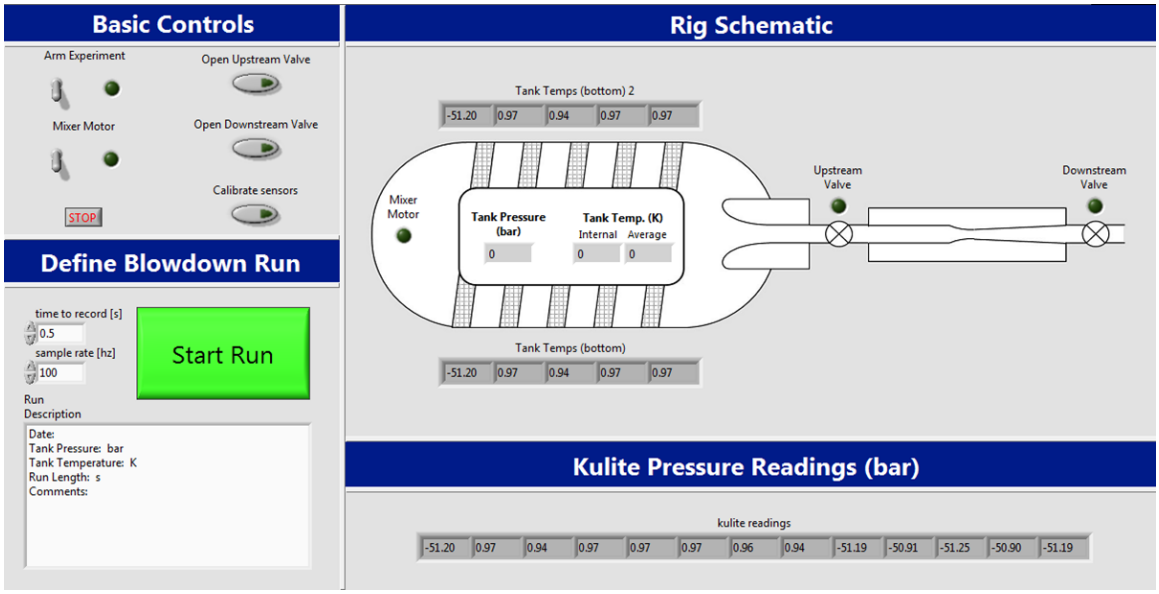

Figure 3-14: New LabVIEW VI developed to handle control and data acquisition for the test rig.

the computer to programmatically pressurize the test section to either the tank total pressure or the ambient pressure of the dump tank. With these two data points, a two-point linear calibration of the Kulites could be performed at the start of each run set. To further simplify operation of the test rig, the calibration established by the VI was used to calibrate the pressure channels before being written to file. This allows for the pressures to be directly read into MATLAB without having to post-process with a separate calibration file.

3.4 Results from Test Rig Improvements

The results of the test rig changes were almost all positive. Following the modification to the mixer motor mount, all components functioned as intended. Filling time from completely empty to a run directly over the critical point (216 kg of CO_2) was reduced from 2 days to 2 hours exceeding the goal of an order of magnitude decrease in time. Additionally, thermal stratification was reduced to a maximum 5K variation across the tank during initial heating and less than 0.1K variation after 30 minutes of 50% duty cycle mixing with the larger impeller. The LabVIEW VI functioned

very well, and only ran into issues which originated from third party code used to control the camera for the interferometer. The tank load cell setup was capable of determining CO_2 fill level to within 0.5% at the highest fill levels and was utilized for accurately determining total density for some of the runs. While the test rig is improved, there are still many changes that could significantly improve usability and accuracy. These ideas are outlined in Chapter 8.

Figure 3-15: insulated charge tank

Figure 3-16: From left to right: electronics rack, charge tank, test section, dump tank, heater control

Chapter 4

Test Section Design

This chapter covers the functional requirements and design for the nozzle test section describing in detail the design methodology as well as the structural, thermal, and fluid analysis that went into the final design. While many of the design parameters of the first test rig carried over to the second generation test rig (tank size, blowdown times, data acquisition) the new test section was a significant design departure. The design transitioned from a one-piece, fixed-geometry, axisymmetric nozzle to a rectangular cross section, modular, optically accessed design outlined below. This chapter covers the structural, fluid, and acoustic analyses that went into the design of this test section. This chapter presents the original design at the time of manufacture. Minor changes were made following initial testing, and these changes are included in Section 4.5. The key idea was to alleviate issues with the first generation test rig while also remaining as flexible as possible for future testing and unforeseen challenges. The capability requirements for the test rig are as follows:

Requirements:

1. Optical access to the test section with sufficient optical quality to perform typical optical analysis techniques (Schlieren, interferometry, PIV, etc.)

2. Increased measurement resolution through higher pressure tap density and field

density measurements in the entire nozzle.

3. Modular nozzle design for flexibility in contour shape and size.

4.1 Overview of Physical Layout and Features

The key to the design methodology for the test section was to separate the structural considerations from the fluid and acoustic considerations. This was mainly to achieve modularity as outlined above. Figure 4-1 shows an exploded view of the test section design which includes all the components contained in the following paragraphs.

Optical access is enabled through elongated glass windows which make up the front and back faces of the nozzle 4-1(b.). While a round test section made entirely of a transparent material would have been technically possible, it would complicate both the manufacturing and measurement processes. Typical optical measurement methods average the property of interest along the optical path. Tomographic methods allow for the extraction of axisymmetric and fully 3-D flow fields, but require the use of multiple viewing angles of the flow which would further complicate the setup [45]. Therefore, a rectangular cross section with flat windows was chosen.

The main body 4-1(a.) and two window retaining flanges 4-1(d.) provide the physical structure which gives the test section sufficient strength and stiffness to withstand the 150 bar pressure loads exerted by the CO_2. The body locates the glass windows for optical analysis in recessed pockets, while the retaining flanges hold the windows against the internal pressure loads, and stiffen the entire assembly. The interface between the window and the main body is sealed via a single crush o-ring 4-1(e.) in the triangular cavity formed by the chamfer on the inside edge of the window and the right angle formed by the sides and bottom of the window pocket. A nylon gasket 4-1(c.) is used to add a compliant surface for the glass to push against, and an expanded Teflon gasket creates a compliant seal between the windows and the nozzle inserts. The gaskets on both sides ensure no metal-to-glass contact which could lead to window failure.

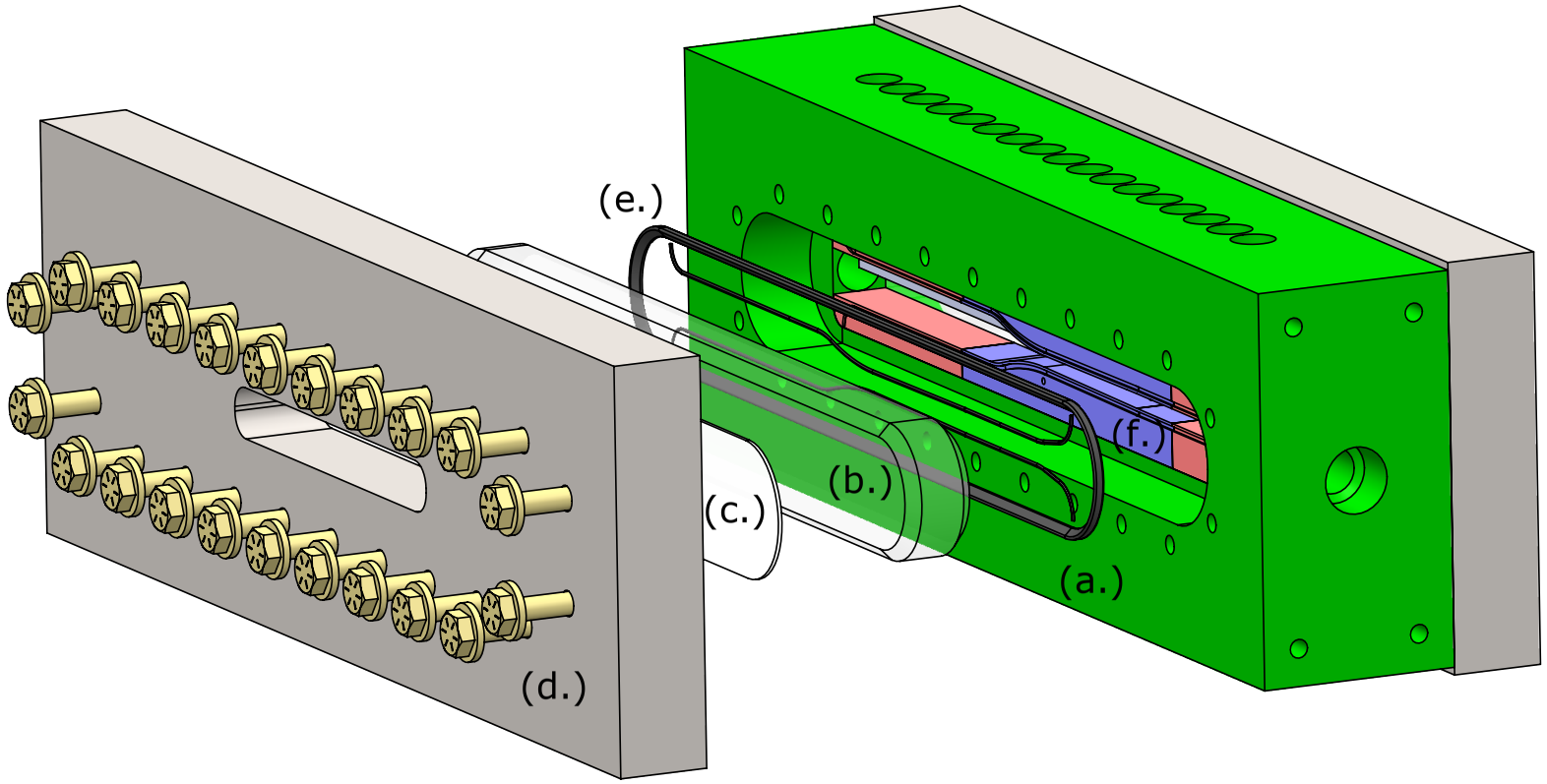

Figure 4-1: Exploded view of the test section showing (a.) main body, (b.) high pressure window, (c.) window spacer/cushion, (d.) retaining flange, (e.) main o-ring seal, (f.) nozzle inserts.

The modularity is achieved by using bolt-in interchangeable nozzle inserts 4-1(f.) and spacers, which determine the upstream and downstream channel heights, and along with the windows, comprise the wetted area of the converging-diverging nozzle. The inserts were designed to be simple and inexpensive to manufacture. They are machined from aluminum as they are required only to withstand the compressive loads from the nozzle pressure which are approximately 20 times lower than the yield strength. Using aluminum decreases the cost by a factor of approximately 5 and allows for the required accuracy of 0.01 microns to be achieved more easily. The inserts can be exchanged without having to remove the pressure transducers or having to remove the test section from the charge and dump tanks and associated valves attached to both ends allowing for easy geometry changes in the future.

To further improve the modularity, mounting locations for Kulites are placed along the entire length of the test section. In the configuration shown in all CAD screenshots, the nozzle is placed directly in the middle. This produces a constant area rectangular duct 6 channel heights in length between the circular-to-square inlet area and the nozzle inlet allowing any flow non-uniformities to mix out. If it becomes necessary to put other geometry in the supersonic flow downstream of the throat, the nozzle can be moved upstream by making upstream and downstream spacer pieces of different lengths.

4.2 Material Selection

Material selection for the test section components was based on three main factors: mechanical properties, corrosion resistance, and machinability. The corrosion requirement limited the available materials to alloys of aluminum and stainless steel. Wherever possible, 6061 aluminum was used for its good corrosion resistance and machinability 8 times better than that of 304 stainless. Its low elastic modulus however, led to it only being used in the non-structural nozzle inserts and spacers. 304 Stainless was used for the window retaining flanges due to its low cost, corrosion resistance, and three-fold improvement in stiffness over aluminum. 17-4 PH stainless

steel was chosen for the main body due to its improvements in machinability and yield strength more than twice as high as that of 304 stainless. The higher strength was necessary due to the stress concentrations found around the Kulite clearance holes which is covered in more detail in Section 4.3.1.

The largest challenge in material selection was encountered in designing the windows. Fused silica (quartz) was chosen for its relatively high abraded tensile yield strength (a common metric for brittle materials) and its extremely low coefficient of thermal expansion (CTE). The low CTE is necessary to limit high stresses in the glass from thermal shock. A quantitative summary of the properties for the materials used is shown in Table 4.1.

Table 4.1: Materials used in the construction of the test section

Material	**Where Used**	**Yield Strength [MPa]**	**Modulus [GPa]**
304 Stainless	Flanges	290	193
17-4PH Stainless	Main Body	760	197
6061 Aluminum	Nozzle Pieces	275	69
Corning 7980 Fused Silica	windows	54	73

4.3 Finite Element Structural Analysis

Due to the high pressures involved, designing the test section to prevent structural failure as well as to limit deflection to acceptable levels was a major challenge. Finite element analysis was used extensively due to the irregularity of the geometries used. The software package ANSYS Structural 15.0 was used for all structural calculations. Whenever possible, symmetry planes were used to minimize the total mesh size and subsequently the computational time. For all the analysis outlined below, the load case was the maximum allowable total pressure of 150 bar exerted on all wetted surfaces. Fatigue was not a concern due to the low cycle rates planned for the test rig. As such, the limiting factor on stress was 2.5X safety factor on yield. Details on

the yielding criteria used to establish these safety factors in the specific parts will be outlined below. For all analyses, areas of stress concentration were identified and the local mesh was successively refined until mesh convergence was reached.

4.3.1 Main Body and Flanges

The main body and flanges are both integral parts of the test section structure. As such, structural FEA was performed on an assembly of both components. Due to the ductility of stainless steel, the von Mises yield criterion was used to ensure that the minimum 2.5X safety factor with respect to yielding was satisfied. In addition to the structural constraints, the main body was subjected to significant deflection constraints. Deflection was a concern around the nozzle throat where it would cause variation in the nozzle throat area. A total deflection equivalent to a 0.5% increase in throat cross section was chosen as the threshold value. This value was predominantly chosen to match structural goals with achievable machining tolerances; the uncertainty in nozzle contour of 1% of throat height so deflections were limited to half this value. To reduce mesh size and computational cost, all analyses for the assembly were performed on a single quadrant with symmetry constraints on the horizontal and vertical planes intersecting at the central axis of the flow path.

Deflection Analysis

The main body is fundamentally a structurally inefficient shape due to the long unsupported span from inlet to outlet. This is unavoidable due to the use of the non-load bearing windows on each side of the flow path. This resulted in the window retaining flanges being extended in height to double as stiffening ribs in addition to holding the windows in place. The key metric for deflection was the total vertical deflection of the surface where the nozzle inserts would be bolted. As stated above a goal of 0.5% increase in throat area was deemed an acceptable limit. This equates to a total deflection of less than 15 microns. Initially, the slot in the side of the window retaining flanges was the entire length of the test section. This provided the maximum

viewing area for the optics; however, it was impossible to keep the deflection to less than 1.5% of the throat area while maintaining a manageable weight for the test section assembly (<30kg). To limit the deflection, the slot was reduced in length to 100mm. This provided a clear view of the entire nozzle, but none of the upstream or downstream sections of the test section. New retaining flanges can be made to optically utilize the front and rear portions of the test section in the event that the nozzle location moves. The results for the FEA deflection analysis can be seen in Figure 4-2 showing a deflection of 9.2 microns, approximately 60% of the allowable value of 15.

Stress Analysis

An initial assessment of the structural integrity of the main body showed stress concentrations at the thin webbing near the inlet and outlet. Geometry changes showed little changes in this stress which led to the use of 17-4 PH over 304 stainless steel. After the change to a partial length viewing slot was made, the majority of the stress was transferred to the flanges, moving the maximum stress to the webbing between counterbores for the Kulites. Localized refinement was added to the mesh around the areas of highest stress to ensure that the FEA was accurately capturing the stress values at all points. A similar mesh convergence study was also performed at the ends of the flange viewing slot where stress concentrations were found. The details of the mesh convergence study for both the flange and the body are shown in Figure 4-3. The final safety factors with respect to yielding were 3.5 for the main body and 3.8 for the flange, exceeding the requirement of 2.5. Figure 4-4 includes a stress plot for the test section body and flange.

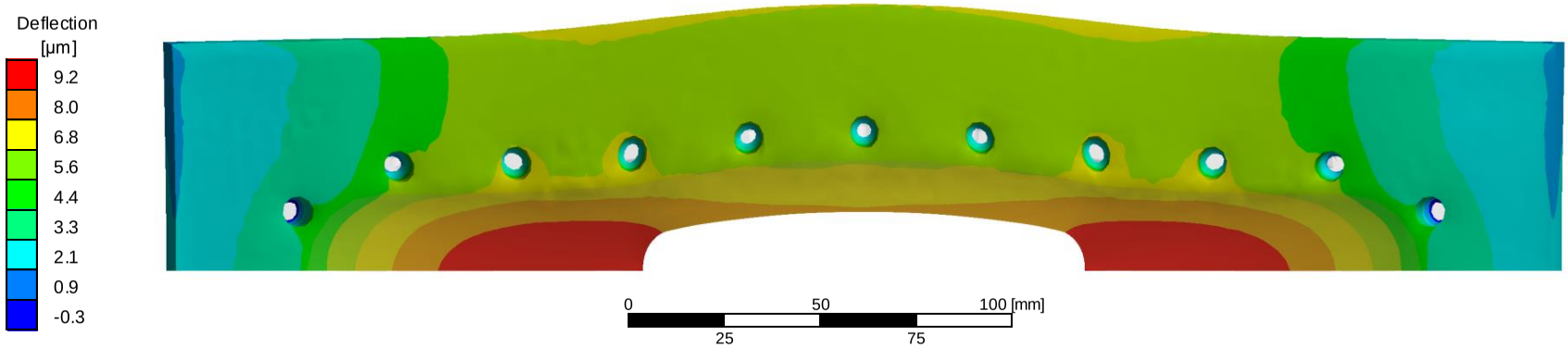

(a) Flange deflection normal to the window face

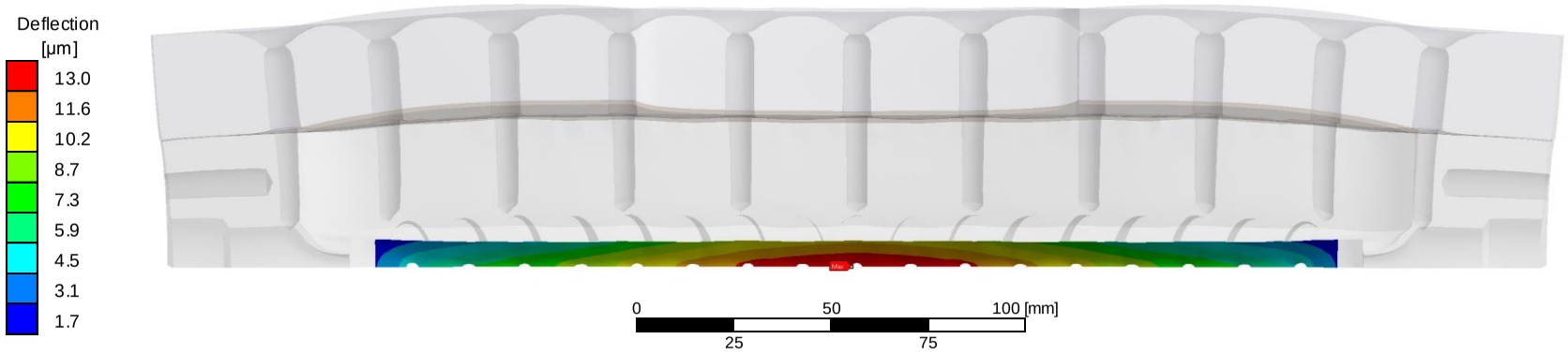

(b) Main Body deflection normal to the nozzle mounting face

Figure 4-2: Directional deflection plots for the Flange and body

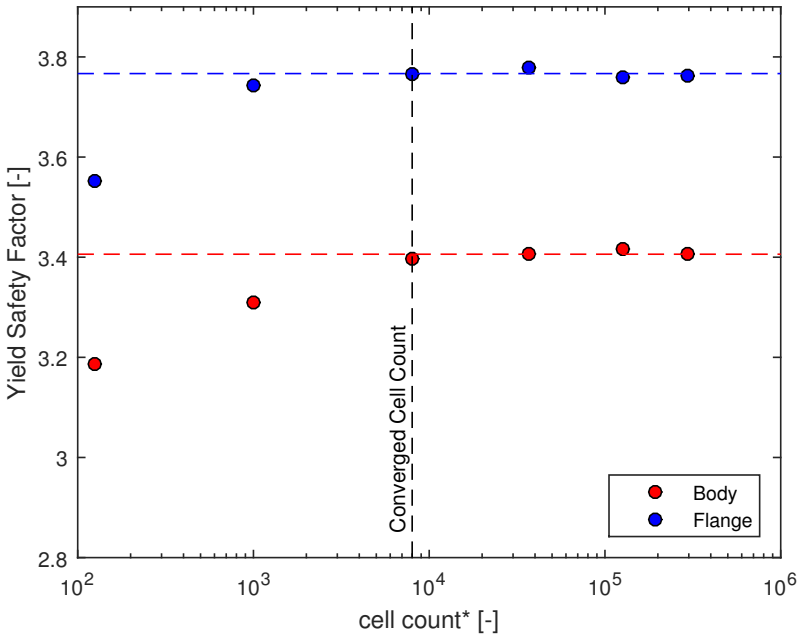

Figure 4-3: Convergence of maximum stress with increasing localized cell count for the main body and retaining flange

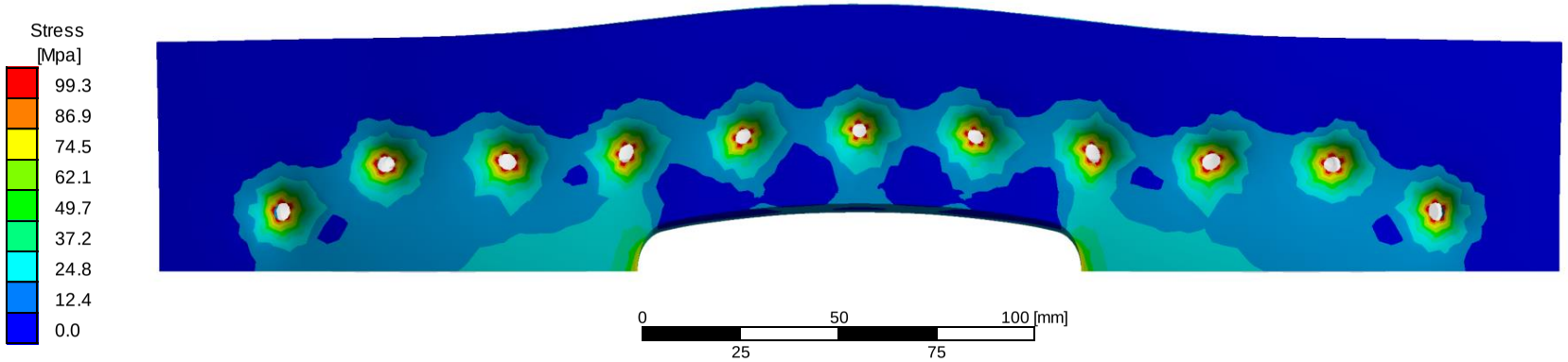

(a) Flange

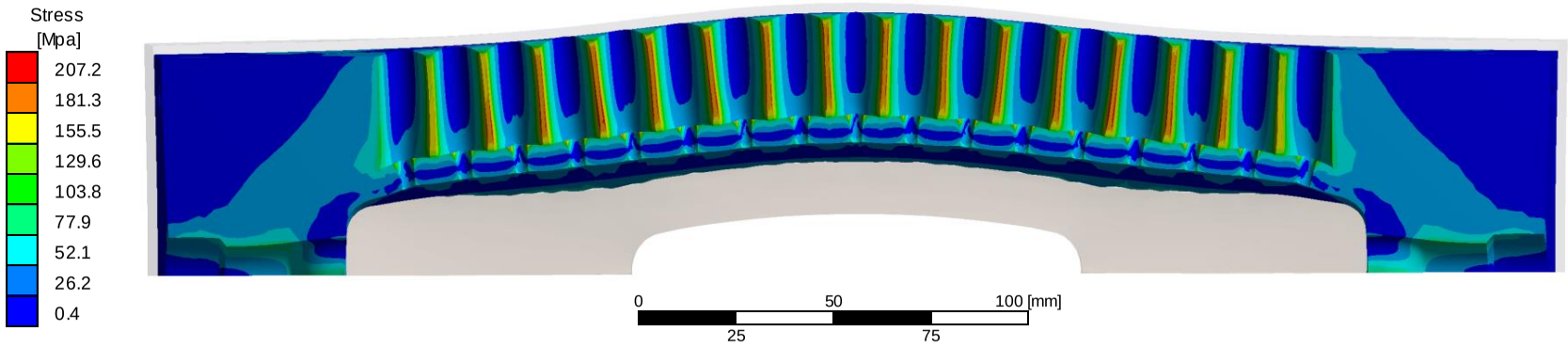

(b) Main Body

Figure 4-4: Von Mises stress plots for the retaining flange and body showing evidence of stress concentrations.

4.3.2 Windows

Fused silica (the material of which the windows are made) and other ceramics typically have very high compressive and tensile strengths. These strengths are compromised in real-world situations by the fracture toughness values 1-2 orders of magnitude lower than those of structural metals [14]. These low fracture toughness values lead to rapid crack propagation from inherent flaws in the material. As an example, flame-drawn fused silica fibers, which have no significant surface imperfections, typically fail at a tensile stress of 6 GPa [39]. This is three orders of magnitude higher than the effective bulk tensile strength given by the manufacturer of the fused silica that was used for the windows [4]. Because of the large difference between the effective tensile and compressive strengths, the typically used von Mises failure criterion is not applicable. The most appropriate failure criterion for brittle materials is the maximum principal stress [9]. All the safety factors discussed after this use this failure criterion.

Confirming Material Properties Through Existing Designs

To confirm that the tensile strengths given by the manufacturer were comparable with effective strengths seen in practice, FEA analysis was performed on a commercially available high pressure window design. MFP products Inc. published information on a custom design for a fused silica window for high pressure applications [1]. Given the quoted failure pressure of approximately 400 bar and dimensions of 15.5mm diameter and 5.5mm thickness, a finite element analysis was set up to evaluate the real-world tensile strength of fused silica in a relevant application.

The FEA simulation was set up as axisymmetric and 2-D to minimize cell count while allowing for high mesh refinement at the top surface of the window, where tensile stresses would be highest. A mesh sensitivity study was carried out with a cell count of approximately 10^5 yielding converged result for maximum principal stress. The calculated tensile strength of 58 MPa was used to define the safety factors for the actual test section windows.

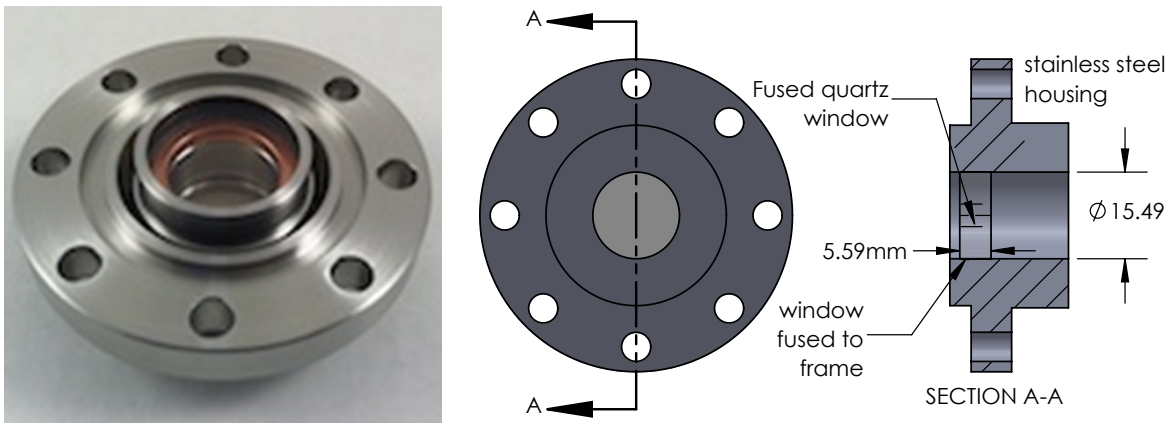

(a) (b)

Figure 4-5: Image (a.) and technical drawing (b.) of the MPF Products Inc. window used to evaluate the strength of fused silica

Window FEA Setup

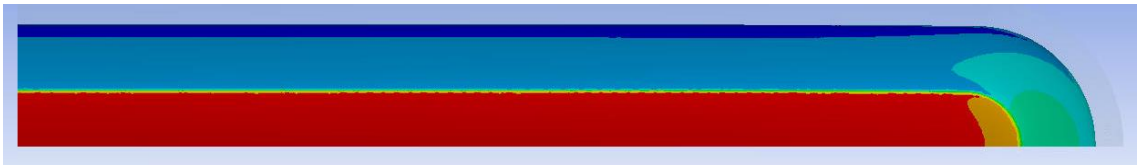

Figure 4-6: contour plot of maximum principal stress on the outside face of the window showing trend towards 2-D plane strain due to the high aspect ratio

The window FEA simulation was initially set up as a 3-D simulation of one quadrant of the window, retaining flange, and the nylon gasket between the two. A mesh sensitivity study was performed on this geometry, but computation times limited the allowable cell size to 50 microns and convergence of maximum principal stress was not observed. This was due to the high gradients in stress near the interface between the window and the nylon gasket where the majority of the pressure forces are reacted. Because of the high aspect ratio of the windows, the stress distribution can be accurately modelled as 2-D plane strain (seen in Figure 4-6). The reduced solve times which resulted from the 2-D simplification allowed for mesh converged calculations to be run using cell sizes down to 20 microns. A plot showing the convergence of stress in the top surface of the window for both the 3-D and 2-D simulations is shown in Figure 4-7.

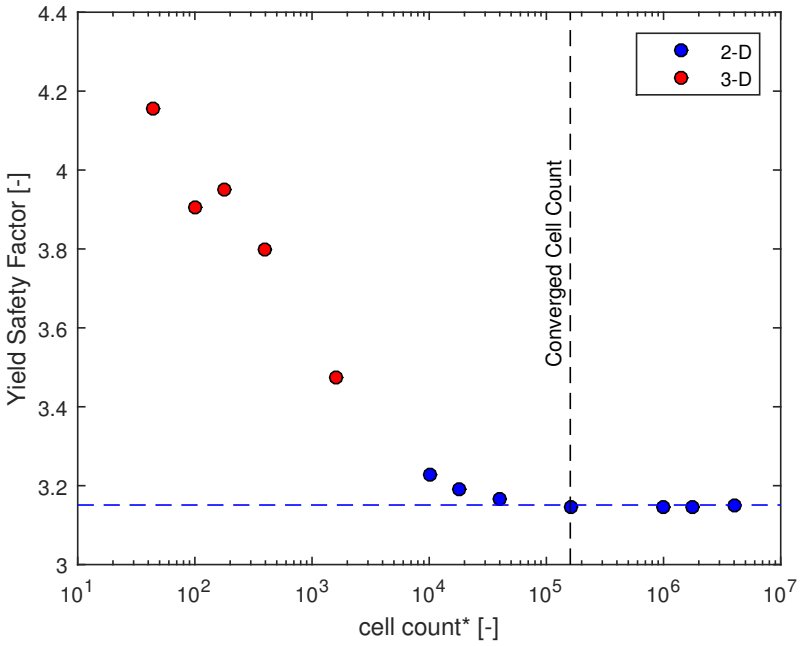

Figure 4-7: Results of sensitivity study on window mesh size showing consistency of results between 2-D and 3-D simulations

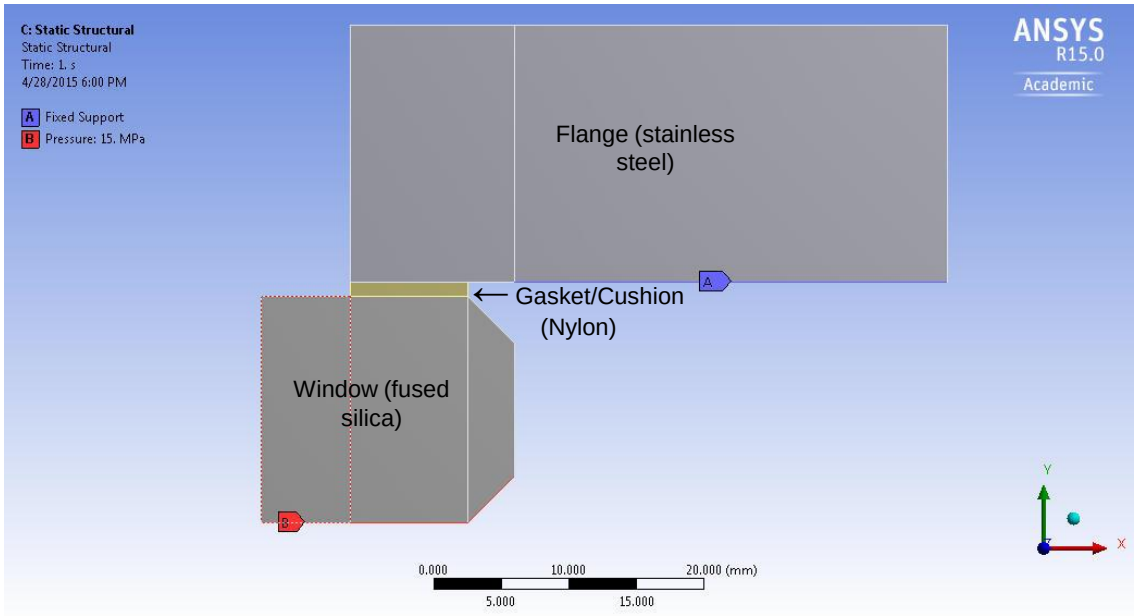

Figure 4-8: 2-D FEA setup for the window

Window Design Parameters Sensitivity Analysis

With a converged FEA simulation of the window set up, a sensitivity analysis on the various free geometric parameters was carried out to explore the feasible design space. The window shape was constrained by the required size of the flow path and the nozzle inserts. The remaining free parameters were the window thickness, and the height of the viewing area. A viewing area as tall as the full height of the nozzle would have been ideal, but a reduced height around the centerline was also considered. The main factors driving the design towards thinner windows were cost and manufacturing constraints. Beyond a cost standpoint, the absolute limit for thickness given the other dimensions of the window was set at 25mm by the manufacturer.

The sensitivity of safety factor to window viewing slot height was found to be low with a 50% reduction in height yielding only a 15% increase in safety factor at a fixed windows thickness of 19mm. Since a safety factor of almost 3 was possible, it was chosen to have the slot be the full height of the nozzle (13mm). The sensitivity of safety factor to window thickness was also investigated, showing diminishing returns for stress reduction through increased window thickness above approximately 20mm. Moving up to the practical maximum of 25mm increased the factor of safety by 10%. A machining drawing for the window showing the final dimensions, tolerances and surface finishes is shown in Appendix A.

4.4 Nozzle Insert Design

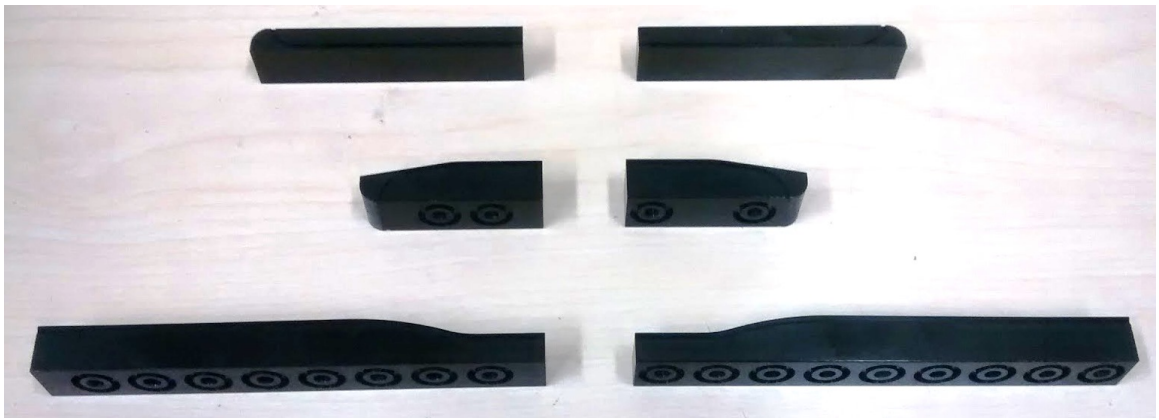

Figure 4-9: Second set of nozzle inserts manufactured for the test rig showing addition of o-ring groove along contour and black anodization to minimize reflected light

4.4.1 Contour Design

The Key feature of the nozzle contour is the elongated diverging section. This was incorporated into the nozzle design to allow for increased pressure measurement resolution for the purpose of detecting condensation onset in the supersonic portion of the nozzle. The shift of measurement focus from subsonic to supersonic flows was a result of the fact that condensation was not observed in the converging section of the previous generation MIT S-CO_2 blowdown test rig [50]. As is covered in more detail in Chapter 6, the diverging section was of limited use due to Mach waves originating from surface imperfections distorting the interferometric fringes.

In addition to lengthening of the diverging section, the overall expansion ratio of the nozzle was reduced from that of the first generation test rig. The expansion ratio was sized such that an expansion with total conditions set to be the temperature and pressure limits of the test rig (380K 150bar) would be entirely single phase, ending at the vapor dome. Using 1-D real-gas constant n_s modelling, an expansion ratio of 1.3 was determined to fit this requirement.

4.4.2 Static Pressure Measurements

Static pressure measurements in the nozzle were made with Kulite XT-190 piezoresistive pressure transducers. These sensors were used with good reliability on the first generation test rig leading to their continued use with the second generation test rig. The Kulites were mounted in the test section body rather than directly in the nozzle to enhance the modularity of the test rig through easy changes in nozzle geometry. This prevented flush mounting and instead required the transducer to be recessed into the nozzle inserts with a narrow passage connecting to the nozzle wall. In this section, this passage and the volume formed by the recessed mounting hole and Kulite face will be referred to as the neck and cavity respectively. Quantitative constraints on the installed performance and geometry of the static pressure taps were as follows.

- Cutoff frequency above 2.5kHz to allow for acoustic response time of the same order as the nozzle through flow time (400μs)

- Static pressure error due to finite tap size below 1%

- Hole depth to diameter ratio below 15 to allow for conventional drilling without specialized tooling.

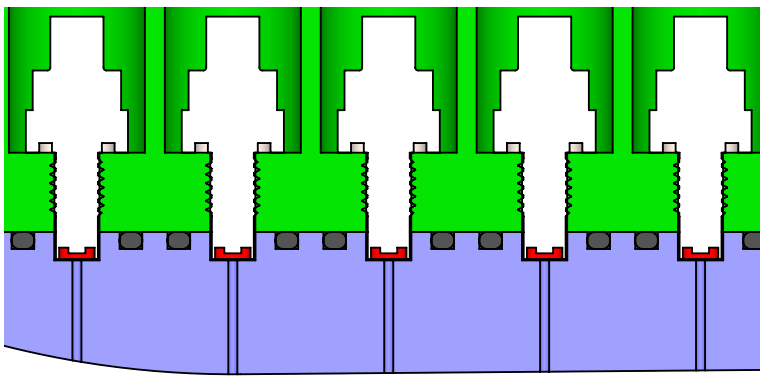

Figure 4-10: Centerline plane cutaway of the test section showing the installed Kulite position in the main body and thin passages which lead to nozzle wall

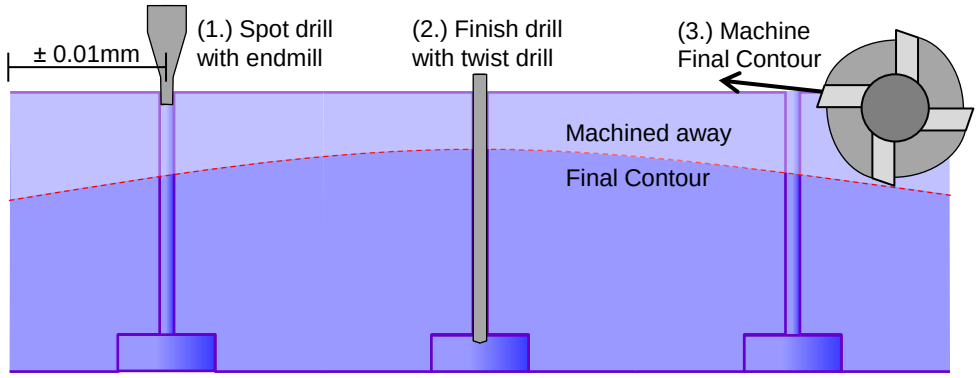

Figure 4-11: Machining process used to ensure accuracy of drilled holes to 0.01mm

4.4.3 Manufacturing Constraints

As is shown in the acoustic analysis below, the neck length should be reduced to maximize the cutoff frequency of the installed Kulite. The minimum neck length was constrained by the height of the nozzle inserts, which, due to manufacturing constraints for the threaded mounting holes, was set at 13mm at its widest point. The length of the neck was minimized by mounting the Kulites such that they protruded from the main body into a cavity machined into the nozzle insert. Figure 4-10 shows the arrangement of the Kulites in the final test section geometry. This arrangement led to a neck length of 10.2 mm.

A hole size of .81mm (.032in.) was chosen to achieve a neck length to diameter ratio of 12.5, just satisfying the manufacturability constraint laid out above. to minimize location error from drill bit drift, the holes were drilled from the nozzle contour side of the insert. A pilot hole was first spot drilled to a depth of 1mm with a 0.81 mm endmill to prevent the twist drill from walking. This allowed for a hole location accuracy of 0.01mm. With all pressure taps drilled, the insert blanks were milled away to the final contour. This is represented graphically in Figure 4-11.

Pressure Errors from Finite Hole Size

While flush mounting of pressure transducers in static pressure measurement applications is ideal for both accuracy and frequency response, it is common practice to measure static pressure using small diameter pressure taps. By introducing a hole of

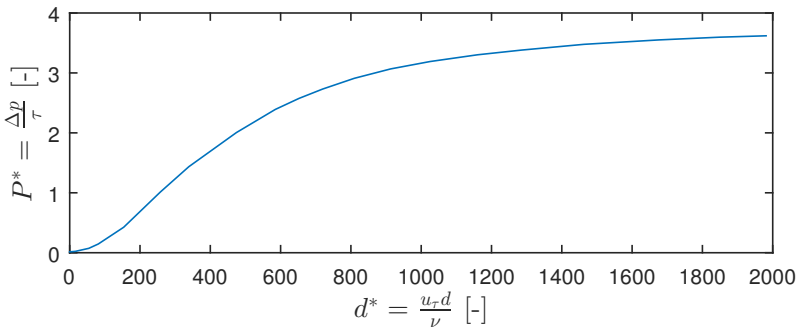

Figure 4-12: non-dimensionalized pressure error vs. non-dimensionalized hole size from [17]

finite diameter into the sidewall of the flow, the boundary layer is disrupted, leading to errors in the measured static pressure. An error analysis based on the hole size established by manufacturing constraints was performed to quantify the accuracy with which static pressure could be calculated.

This effect was presented as pressure error non-dimensionalized by wall shear stress as a function of non-dimensionalized hole diameter $d*$ in [17].

$$\frac{\Delta P}{\tau} = f\left(\frac{u_\tau d}{\nu}\right)$$

$$P^* = f(d^*)$$

Where P* is the pressure error non-dimensionalized with wall shear stress and d* is the hole diameter non-dimensionalized with the friction velocity and kinematic viscosity. Data points from many different hole size and wall shear stresses were plotted and curve fit yielding the curve shown in Figure 4-12.

A representative Reynold's number was calculated based on the throat hydraulic diameter, speed of sound, and kinematic viscosity. A wall roughness of 2 microns was assumed (typical of a well milled surface). Assuming locally fully developed turbulent pipe flow, a Darcy friction factor of 0.01 was calculated using a Moody chart [35]. A maximum pressure error of 0.8% of total pressure was calculated using the estimated wall shear stress and an assumed asymptotic value of 4 for the curve in Figure 4-12. This error is included in the error analysis covered in Chapter 6.

Acoustic Analysis

In open air, the sensors have a cutoff frequency of 1.4 Mhz [5], however the installed frequency response can be significantly lower. The geometry was simplified to a Helmholtz resonator with an acoustic duct and a 1-D acoustic analysis was carried out to evaluate the performance of the geometry established by the manufacturing constraints laid out above.

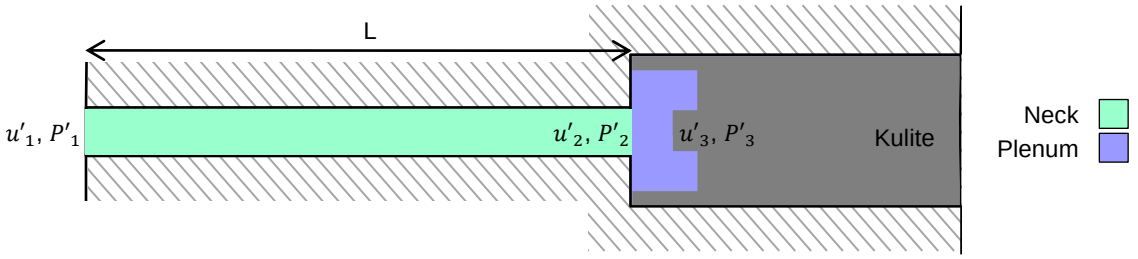

Figure 4-13: Acoustic model of the Kulite mounted in the test section

An initial assessment of the Kulite performance was made using the classic lumped mass Helmholtz resonator model. This model assumes the neck of the resonator is acoustically compact with a physical length much smaller than the wavelength of a sound wave at a representative frequency. This assumption was made, and subsequently evaluated for validity. The Helmholtz frequency is defined in [43] as

$$f_H = \frac{c}{2\pi}\sqrt{\frac{A}{V_0 L}}, \tag{4.1}$$

where c, A, V_0, and L represent the speed of sound, neck cross section, cavity volume, and neck length respectively. The speed of sound at 315K and 95.7bar (223m/s) was used in conjunction with the neck length and cross section of 10.2mm and 0.52mm^2 and cavity volume of 7.79mm^3 to calculate a natural frequency of 2876 Hz. The wavelength at this frequency is 12.4mm as calculated by

$$\lambda = \frac{c}{2\pi f_H}, \tag{4.2}$$

leading to a wavelength to neck length ratio of order 1 and a violation of the compact

neck assumption.

To include the effects of an acoustic neck, a 1-D acoustic model was constructed using the transfer/transmission matrix method outlined in [20]. A schematic of the model is shown in Figure 4-13. Models with and without viscous damping were evaluated. Using the transmission matrices for an inviscid acoustic duct and plenum, and appropriate boundary conditions, a matrix equation for the acoustic model without damping can be written as follows:

$$\begin{bmatrix} P_1' \\ \rho a u_1' \end{bmatrix} = \begin{bmatrix} cos\left(\frac{\omega L}{a}\right) & isin\left(\frac{\omega L}{a}\right) \\ isin\left(\frac{\omega L}{a}\right) & cos\left(\frac{\omega L}{a}\right) \end{bmatrix} \cdot \begin{bmatrix} 1 & 0 \\ \frac{i\omega V}{aA} & 1 \end{bmatrix} \cdot \begin{bmatrix} P_3' \\ \rho a u_3' \end{bmatrix} \tag{4.3}$$

The addition of viscous damping yields the following matrix equation:

$$\begin{bmatrix} \frac{P_1'}{\rho a} \\ u_1' \end{bmatrix} = \begin{bmatrix} e^{-CL} + e^{CL} & \frac{\nu}{C}\left(e^{-CL} i e^{CL}\right) \\ \frac{C}{D}\left(e^{-CL} i e^{CL}\right) & e^{-CL} + e^{CL} \end{bmatrix} \cdot \begin{bmatrix} 1 & 0 \\ \frac{i\omega V}{aA} & 1 \end{bmatrix} \cdot \begin{bmatrix} \frac{P_3'}{\rho a} \\ u_3' \end{bmatrix} \tag{4.4a}$$

$$C = \sqrt{(}\frac{i\omega}{\rho a^2}(\rho i\omega + \zeta) \tag{4.4b}$$

$$D = \rho i\omega + \zeta \tag{4.4c}$$

$$\zeta = K\frac{32\mu}{D^2} \tag{4.4d}$$

Equation 4.4d defines the viscous damping based on the friction factor for laminar axisymmetric Hagen-Poiseuille flow [48],[50]. The leading coefficient K in is an empirical constant used to tune the model to fit experimental data. Two key findings were made with the 1-D acoustic models

1. For a duct to wavelength ratio of 1, the effect of an acoustic vs. lumped neck is minimal: The lumped neck model predicted the resonant frequency to within 0.01% of the acoustic neck model

2. The proposed geometry is highly underdamped with very little sensitivity of

resonant frequency to damping K factor: a K factor on the order of 100 only changes the resonant frequency by less than 0.1%

Figures 4-14a and b shows the transfer function from P_1' (nozzle) to P_3' (Kulite) for a lumped neck, inviscid acoustic neck, and viscous acoustic neck with a K value of 10. A zoomed in plot is shown in Figure 4-14b to highlight the effects of viscosity on the transfer function. The final results show a resonant frequency of 2590 Hz, satisfying the requirement of a resonant frequency above 2500 Hz.

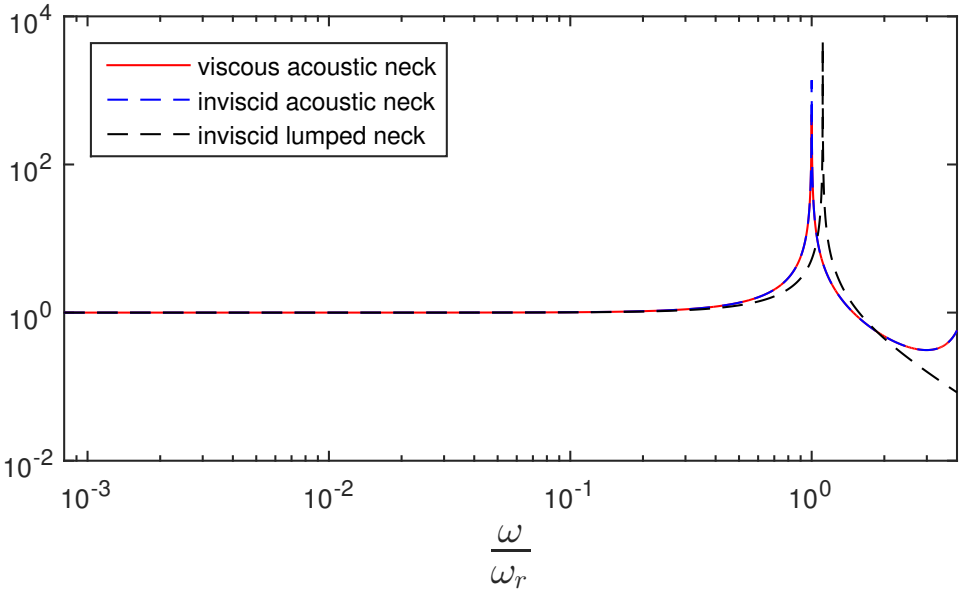

(a)

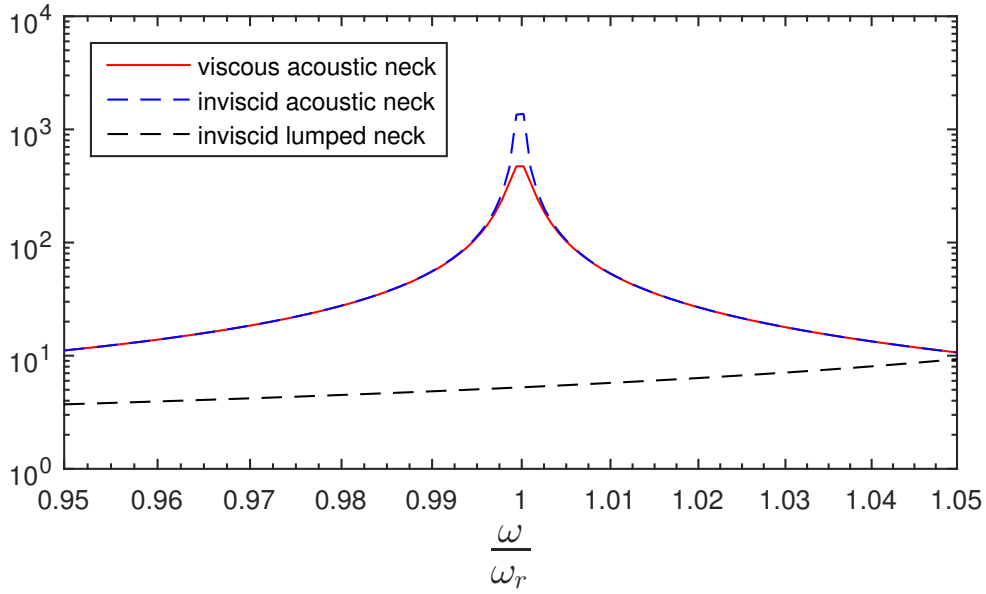

(b)

Figure 4-14: Comparison of Transfer functions for the acoustic model showing the minimal effects of acoustic compactness and viscosity assumptions on the resonant frequency (x-axis non-dimensionalized with the lumped neck Helmholtz resonance frequency)

4.5 Post Construction Test Section Design Changes

Three changes were made to the original design of the test section following initial testing: an updated sealing interface between the nozzle inserts and the windows, a modified downstream spacer geometry to prevent unintended choking, and a modification to the Kulite mounting holes to allow for both metric and standard sensors.

4.5.1 New Sealing Interface

The expanded Teflon gasket initially used between the windows and nozzle inserts proved to be unreliable in operation, and difficult to use during installation and removal of the windows. The combination of the S-CO_2 environment and the constant surface pressure from the windows caused the gaskets to adhere to the inside surface of the windows during disassembly. This made the gaskets only usable for one installation requiring a roughly hour long process of scraping and cleaning before reassembly with new gaskets could take place. In addition, the gaskets were difficult to orient correctly during installation leading to the edges protruding into the flow, disturbing both the nozzle flow and impeding the use of the interferometer across the entire channel. The gaskets also showed evidence of leakage in the downstream (diverging) section of the nozzle, although later analysis showed this was more likely due to Mach waves from imperfections in the nozzle, not leakage.

To alleviate these issues, the gasket sealing interface was replaced with an o-ring sealing gland along the contour of the nozzle. This had several advantages over the gasket: the ability to be reused for 10 or more reassemblies, a leak-free seal between regions of the nozzle, and no protrusions into the flow or obstructions of the field of view. The minor disadvantage with the design were increased manufacturing complexity due to each o-ring requiring a separate machining setup, and the creation of a leak path around the outside of the nozzle. Since the nozzles were made in house, machining complexity was not a major concern. The geometry of the o-ring gland provided a second path from inlet to outlet, but was isolated from both the main nozzle flow path and the ambient environment. The only effect this had on test rig

performance was a 2% increase in mass flow rate. To eliminate the space between the inserts and the windows, the inserts were made wider, leaving only a .075mm clearance between insert and window on both sides.

4.5.2 Downstream Choking

Initial tests showed fully subsonic flow in the nozzle indicating a second, smaller choke point downstream of the intended throat in the nozzle inserts. A run exhausting into open air (downstream valves and flex pipe removed) also failed to produce supersonic flow in the diverging section, indicating that the choke point was inside the test section. Figure 4-15 presents the results of a comparison between experimental pressure measurements and those calculated from a 1-D isentropic model showing a Mach number of approximately 0.7 at the throat.

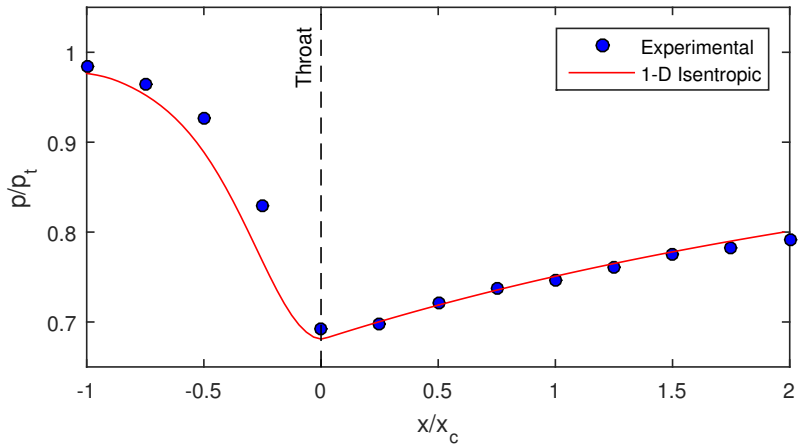

Figure 4-15: Comparison between experimental data and 1-D calculation showing subsonic flow in the diverging section indicating a second throat downstream of the nozzle.

Inspection of the insert design showed that the downstream spacer blocks and the square to circular transition created a second throat with a cross section only 10% larger than that of the intended nozzle throat. In a purely 1-D isentropic flow, this second contraction would not be small enough to prevent choking of the upstream flow, but it was assumed that flow separation at the sharp transition from a rectangular

to circular cross-section led to blockage and an effective area small enough to choke the flow. This concept is illustrated in Figure 4-16.

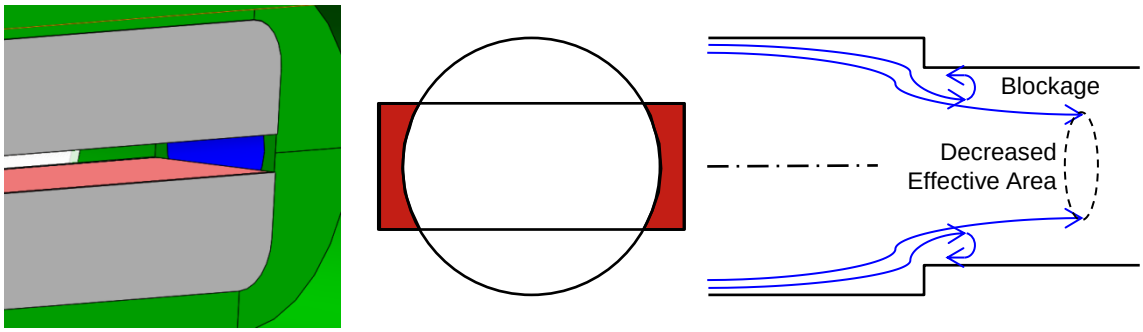

Figure 4-16: from left to right: Isometric, axial, and vertical view of the second throat caused by the transition between the nozzle spacers and the test section body.

To eliminate this choke point, the new nozzle inserts incorporate a sloped transition from the constant area rectangular duct following the diverging section to the circular outlet port. A comparison with the original and new spacer black CAD models is shown in Figure 4-17

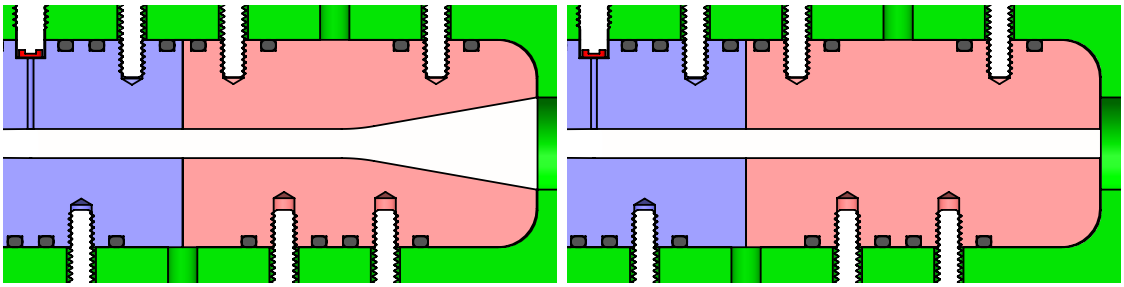

Figure 4-17: Sloping spacer block (a.) designed to eliminate choking compared with the original straight design (b.).

4.5.3 Other Changes

In addition to the minor geometric changes, all the new nozzle and spacer inserts were anodized flat black. This was done to prevent any reflections from the nozzle surfaces from blurring out the fringes created by the interferometer. Figure 4-18 shows the difference between the two versions of the nozzle inserts. Also modified

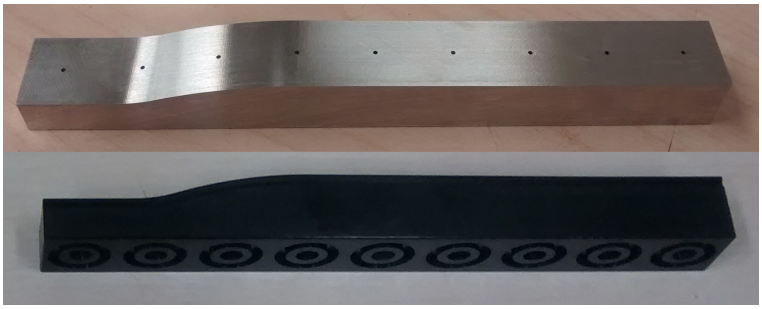

Figure 4-18: Comparison between original nozzle inserts and the second set of incorporating the o-ring groove and black anodization

from the original design are the mounting holes for the pressure transducers. Due to availability at the time of purchase, some of the transducers are metric thread and some are standard thread. To allow for the use of both, the test section was modified to have Metric Kulite mounting holes on top and standard mounting holes on the bottom.

4.6 Performance of Updated Test Section

Upon completion of the modifications listed above, the test section functioned without issue both in a structural/fluid and optical sense. Static pressure testing was performed up to 150bar to ensure reliable operation and through flow tests up to 101 bar showed no structural issues. Both the window and Kulite seals proved leak free at all operating pressures. In an optical sense, the windows provided a distortion free view of the test section allowing for both interferometer as covered in Chapter 5, and condensation visualization as shown in Chapter 7

Chapter 5

Optical Density Measurement

This chapter outlines the design and theory of the shearing interferometer which was used to measure density in the test section. As stated in Chapters 3 and 4, the main goal of the second generation rig and updated test section was to have the ability to fully characterize the thermodynamic state of the CO_2 in the nozzle. This required having the ability to measure another thermodynamic property in addition to static pressure. After the difficulties with the Helmholtz resonator based speed of sound measurement implemented in the first generation rig, a more established measurement method was desired. Optical analysis was chosen as it allowed for non-contact measurements to be made, and ensured that the flow was unaffected by these measurements. Furthermore, optical access to the test section allowed for the observation of condensation, removing the ambiguity that resulted from having only static pressure measurements to detect condensation in the first generation rig.

5.1 Optical Flow Analysis Techniques Considered

The main criteria used in evaluating potential optical analysis methods were as follows:

- Ability to provide quantitative data on thermodynamic state in the nozzle rather than simple visualization of flow phenomena

- Robustness to optical imperfections and vibrations
- Minimal effect on the fluid flow

The optical fluids analysis techniques considered for fully characterizing the flow in the test section can be divided into two main categories: velocity based methods, and density based methods.

Velocity Based Methods

The two velocity based methods considered for analyzing the nozzle flow were particle image velocimetry (PIV) and laser Doppler velocimetry/anemometry (LDV/LDA). Both of these methods measure the velocity of the flow. At a basic level, PIV works by measuring the incremental movement of small particles entrained in a fluid flow. In practice, two images are taken a short (relative to the through flow time of the test article) time step apart, and the movement of the different regions of particles are tracked to measure velocity [40]. LDV is a point velocity measurement method which utilizes the Doppler shift between a reference beam and a beam scattered from seeding particles in a flow [12]. While both of the above methods are capable of producing the quantitative information needed for this research, they were deemed unsuitable due to the potential effect of the required seeding particles on the onset of condensation.

Density Based Methods

Density based optical flow analysis methods utilize the dependence of refractive index on density in transparent media. The four methods considered for this research are Schlieren imaging (traditional and background-oriented), shadowgraphy, and interferometry. Schlieren and shadowgraphy utilize the bending of light rays through a medium with a gradient of refractive index perpendicular to the direction of light propagation. As such, only the spatial derivatives of density can be directly extracted from the resulting images. Shadowgraphy is the simplest method, yielding a qualitative image of the second derivative of density. While it is simple to set up (it

consists of only a focused light source and a projection screen or camera), it is not useful for gathering quantitative information on absolute density. Schlieren is similar to shadowgraphy, but incorporates a knife edge to block light that has been deflected by density gradients. This produces an image which represents the first derivative of density. While it is possible to integrate the density gradient field produced by Schlieren, it is commonly used only for qualitative imaging. Due to the qualitative nature of the data produced by Schlieren and shadowgraphy, and their sensitivity to sharp gradients, they are typically used to visualize shocks, expansion fans, and other flow features in supersonic and transonic flows[44]. Example of both Schlieren and Shadowgraphy images of supersonic flows are shown in Figures 5-1a, and 5-1b. Since quantitative information was desired, both traditional Schlieren imaging and shadowgraphy were deemed inappropriate for this research.

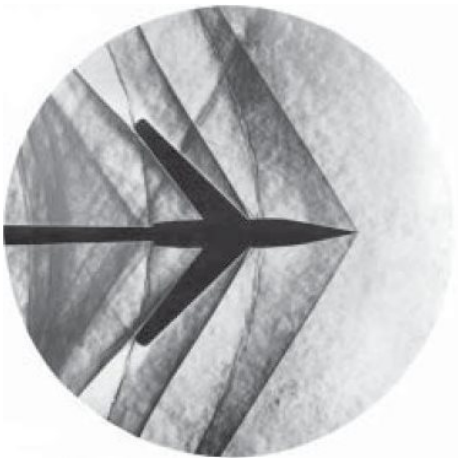

(a) Schlieren image of a sharp-nosed body in supersonic flow. Image credit NASA

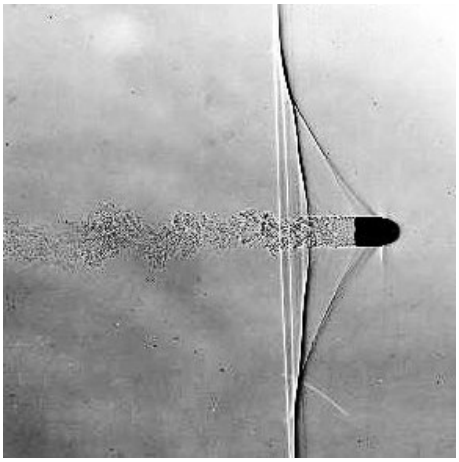

(b) Shadowgraph image of a bullet in flight: credit Danile P.B. Smith, 1962

Figure 5-1: Examples of qualitative density based optical flow analysis

Two methods which can be used to extract quantitative information are interferometry, and Background Oriented Schlieren (BOS). Background oriented Schlieren combines the refractive index bending of Schlieren with the particle tracking processing method of PIV. A known background pattern is placed behind the flow field to be investigated. Images taken of the background pattern through the test section with and without flow are compared and the shift of various regions caused by refractive

index bending is quantitatively measured through post processing [16]. An example image created with BOS using the ground below an aircraft as a pattern is shown in Figure 5-2b. Since the measured distortions of the background image are due to gradients in index of refraction, the results must be integrated from a known reference to find the absolute density.

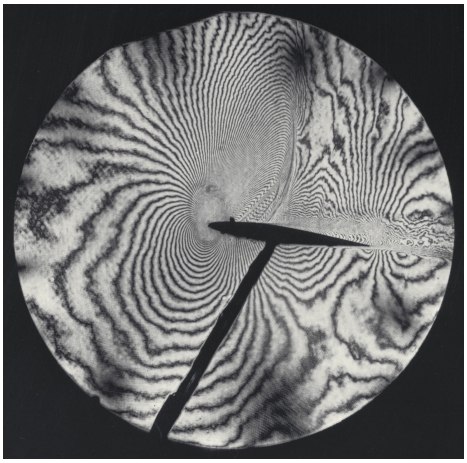

(a) Interferometric fringe image of a transonic airfoil. Image credit NASA A79-0054-4

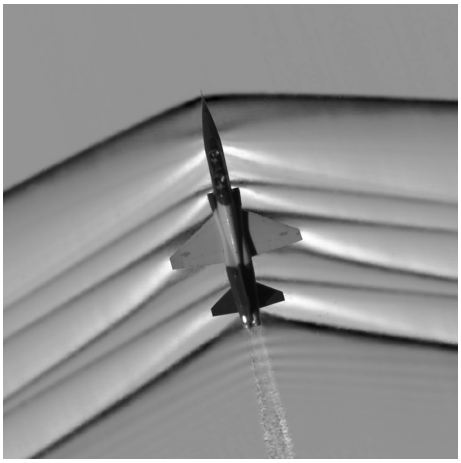

(b) Post-processed BOS image of a supersonic aircraft in flight. Image credit NASA

Figure 5-2: Examples of density based quantitative optical flow analysis

Interferometry also utilizes the change of refractive index with density. The distinguishing characteristic of interferometry is that it utilizes the phase lag of the wave fronts caused by a change in optical path length due to the absolute value of a medium's index of refraction rather than the bending caused by its gradient. Both ray bending and wavefront phase lag typically occur simultaneously in optical analysis, but the way in which the distorted light is recorded allows for the isolation of one phenomenon. Since interferometry is based on the absolute density of the medium, traditional Mach-Zehnder interferometers directly measure absolute density rather than the derivative.

Since the information, in an interferogram is represented by the physical location of fringes on the resulting interference pattern rather than the raw pixel (brightness) value, interferometry is much better suited for extracting quantitative information on the density of a flow. This addresses one of the key challenges in extracting quanti-

tative information from a traditional Schlieren photograph. Since the information in a Schlieren image is carried in the light intensity, there is ambiguity in the extracted information as one camera may register a different sensitivity or even have a non-linear output based on light intensity. Because of these reasons, interferometry was chosen as the appropriate method of measuring the density in the test section.

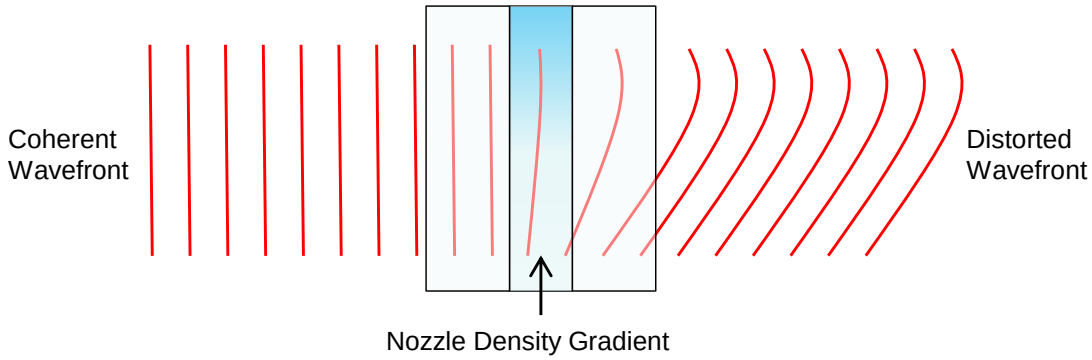

Figure 5-3: The basis of interferometry: wavefront distortion (phase lag) of a coherent beam as it travels through a density gradient

5.2 Shearing Interferometer Design

5.2.1 Interferometer Theory

A common application for interferometry is the analysis of external flows with minimal real-gas effects and typical densities two orders of magnitude lower than those seen in the present experiment [32]. The work of Lamanna on condensation shocks in a steam-nitrogen mixture was performed in a very similar geometry to that of the current research, but at densities and pressures three orders of magnitude lower than those seen in S-CO_2 [26]. Duff performed similar research with subcritical CO_2 condensation, but at pressures and densities approximately two orders of magnitude lower than the current research [15]. The high densities of CO_2 near the critical point are of order 1000 kg/m^3 introducing new challenges in image analysis. At these densities, the interference pattern from an absolute interferometer (commonly referred to as a fringe pattern or fringes) would become narrowly spaced, requiring

approximately 200 pixels per mm of view field. This necessitates a digital camera with a resolution on the order of 100 MP to capture the raw images of the region of interest in the test section.

The key idea utilized in the current research is to measure density gradients using a shearing interferometer instead of absolute density to allow for the use of a standard high-resolution DSLR camera (16MP). This method also satisfies the robustness requirement laid out above as a shearing interferometer is more tolerant of vibration optical defects than a conventional Mach-Zehnder interferometer or Schlieren imaging system [32].

In a standard Mach-Zehnder interferometer, the phase-shifted beam that passes through the test section is compared with a coherent reference beam [44]. Because there are two separate beams that must remain in phase, the system is susceptible to vibration and control of the path length at the sub-micron level is required. A shearing interferometer, as used in this experiment, is a common path interferometer where a single beam is divided into two beams after passing through the test section. The beams are then combined with a spatial displacement, creating interference fringes. The fringe pattern is a measurement of the density change between the two paths and can be numerically integrated to calculate the absolute density of the gas.

5.2.2 Interferometer Construction

The interferometer that was designed and built for the CO_2 test rig is shown in Figure 5-4. A 50 mW diode laser with a wavelength of 671 nm and coherence length greater than 1m is expanded and collimated through a microscope objective and a standard camera lens respectively. The beam passes through the test section and experiences a phase lag as well as an angular deflection caused by density changes within the gas. This deformation of the light is illustrated in Figure 5-3. Refractive index bending was minimized by focusing on a plane 1/3rd of the test section width from the beam entry point as described by [33]. After passing through the test section, the beam is split using a plate beam splitter. The beams are re-directed by two mirrors and then pass through a second beam splitter which recombines them

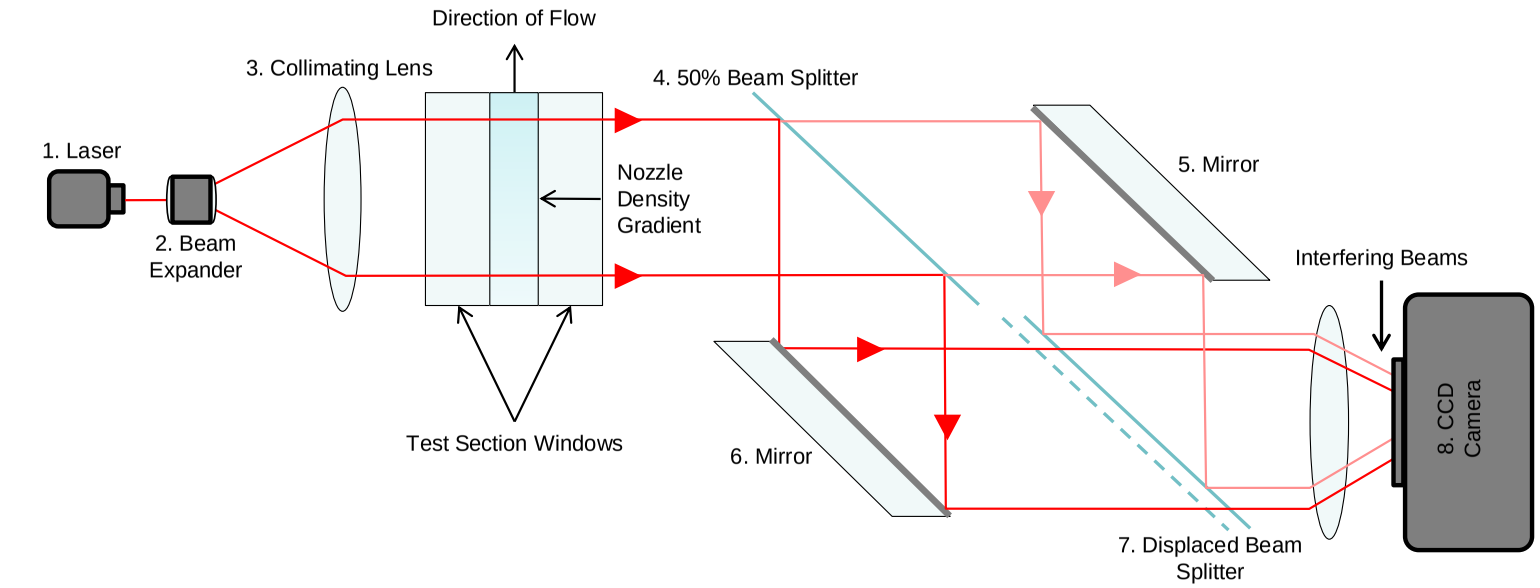

(a)

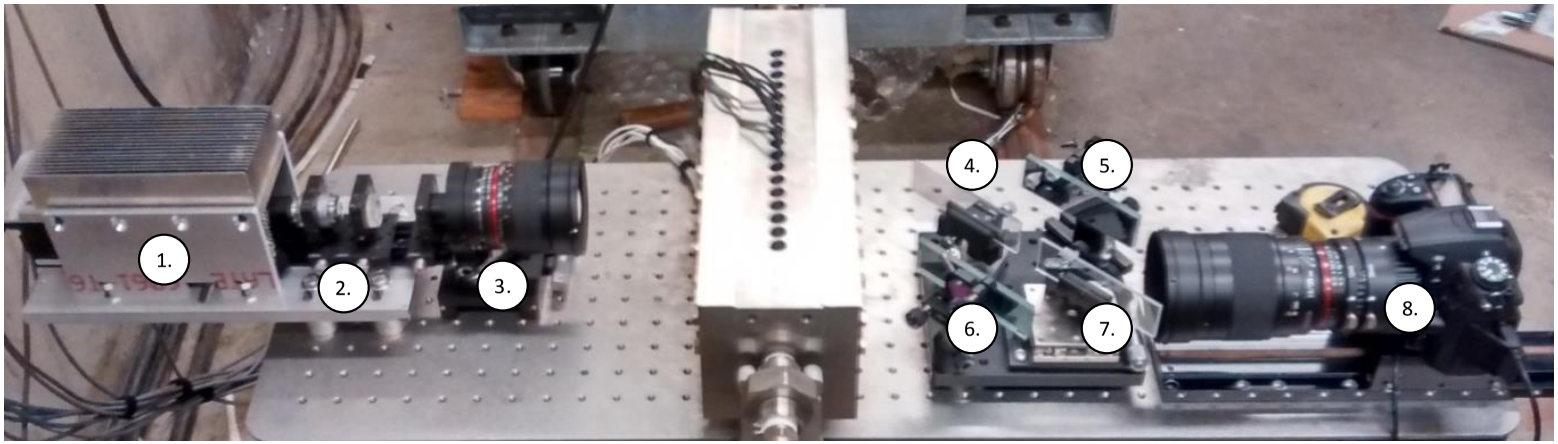

(b)

Figure 5-4: Schematic a and image b of the shearing interferometer used on the MIT CO_2 test rig

into a single beam. By changing the position of the second beam splitter, the spatial shift between the beams can be adjusted. The fringe pattern from these beams is then focused onto the CCD chip of a digital camera where the interference pattern is recorded.

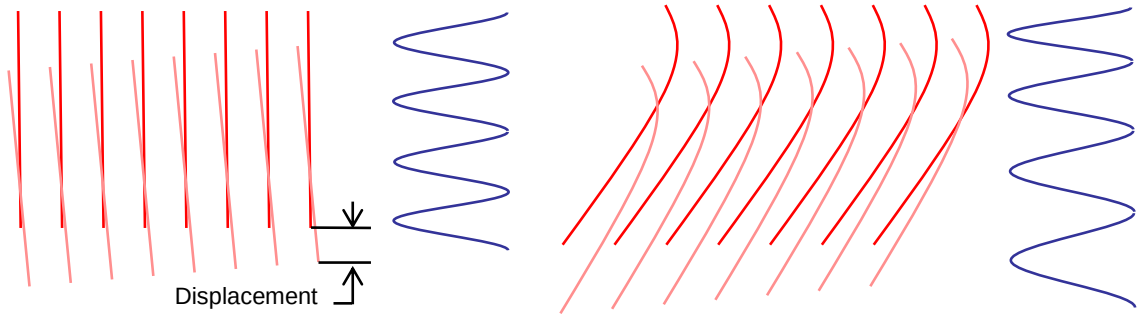

(a) Without flow in nozzle (undistorted) (b) With flow in nozzle (distorted)

Figure 5-5: Effect of wavefront distortion on resulting interference pattern. Sinusoidal fringe pattern becomes stretched due to distortion from variable density flow.

A static fringe pattern (carrier fringes) is created by applying a rotation about the vertical axis to one of the mirrors. A spatial displacement between the beams is created by moving the second beam splitter with a micrometer actuated optical traverse. The amount of spatial displacement between the two beams compares the different optical paths through the flow as a phase shift, which adds or subtracts to the phase of the carrier fringe pattern. This spatial shift enables the shearing interferometer to quantitatively measure the density gradient within the flow. The rotated and shifted beams with and without distortion from a density gradient are illustrated in Figure 5-5.

The beam-splitter setup is a variation of a Twyman-Green interferometer, typically used for the quantitative evaluation of optical components. Moving the final stage beam-splitter, creates a linear displacement of the shearing images, whereas, applying a tilt to one of the mirrors produces a non-linear shift more associated with conventional qualitative shearing systems [38]. The combination of these approaches has several advantages:

1. It incorporates an accurate and adjustable linear displacement between the

beams allowing for variable sensitivity over a wide range of operating conditions.

2. The path difference can be optimized, both to take account of the coherence of the light source and to accommodate the path length change due to density change experienced within the flow.

3. The sensitivity can be non-linear (variable across the image which simplifies the numerical integration stage where the density gradient in the flow changes substantially from the start of the channel to the throat.

Precise knowledge of the displacement between the beams is key in extracting accurate quantitative data from the interference images, and a novel method was developed specifically for this rig.

5.2.3 Determination of Beam Displacement

Typical displacements between the two legs of the beam-splitter, δ, are approximately 250 microns. An accuracy of 5 microns was required to achieve an uncertainty of 2% for density measurements. Each pixel of the image is approximately 11 microns, which means that sub-pixel resolution accuracy is required. The micrometer slide on which the second beam splitter was mounted could only provide relative displacement information, so developing a method for establishing the zero point of the beam splitter (where the images are exactly superposed) was the key challenge. Initially the beam displacement was determined by measuring the distance between tick marks on a double image of a high-resolution ruler. An example image of the ruler taken through the beam splitter is shown in Figure 5-6. This gave an accuracy of approximately 30 microns, and was limited to directly measuring displacements greater than 250 microns due to the finite width of the lines being imaged. The large errors were mostly due to the inconsistencies of edge detection of the tick marks on the ruler.

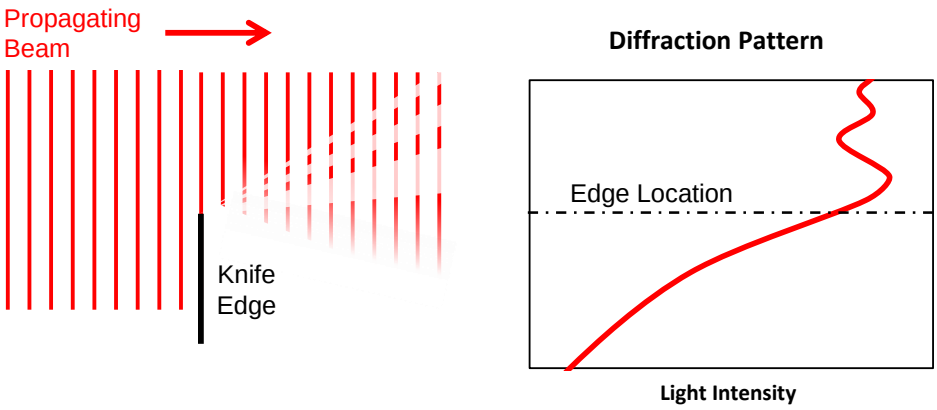

Figure 5-7: Qualitative illustration of a knife edge diffraction pattern showing both the wavefront view and the resulting 1-D interference pattern

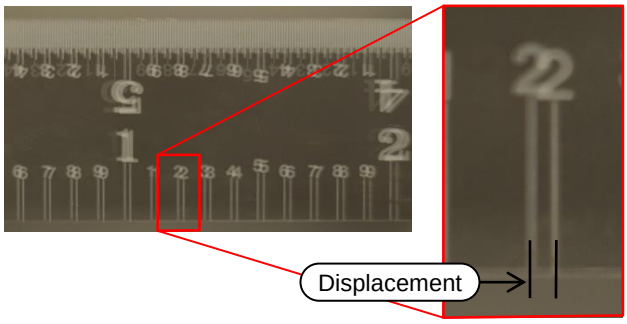

Figure 5-6: Calibration image of ruler used in original displacement finding method. Note the blurriness of the image and the large 200 micron width of the individual white strips

To alleviate the issues with edge detection, the ruler image was replaced with a knife edge, backlit by the laser described earlier. A knife edge lit in this manner creates a very distinct and repeatable interference pattern qualitatively illustrated in Figure 5-7. The theory behind the creation of a diffraction pattern rather than a sharp discontinuity by a knife edge is described in [11]. This diffraction pattern was recorded through both the fixed (left) and displaced (right) legs of the interferometer in two separate images. To isolate the two images of the knife edge, a blocking plate was used. In the raised and lowered positions, the left and right beams respectively, were each allowed to pass. A schematic and image of the setup is shown in Figure B-17a.

In addition to the edge diffraction pattern which moves away from the vertical

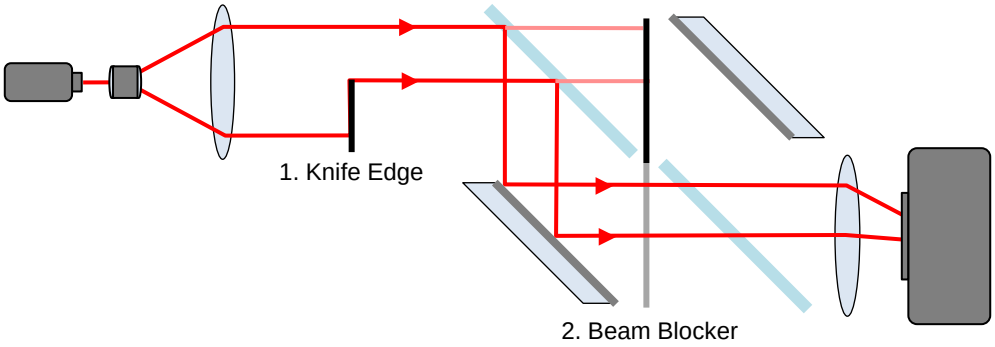

(a) Top view of the knife edge setup with the right (displaced) beam blocked

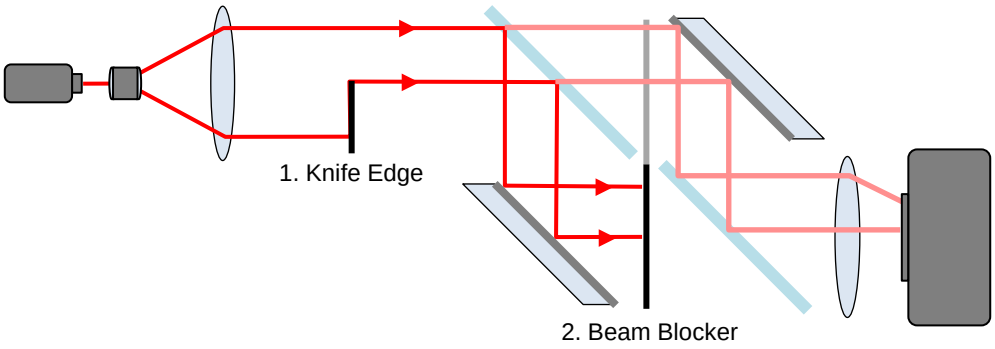

(b) Top view of the knife edge setup with the left (fixed) beam blocked

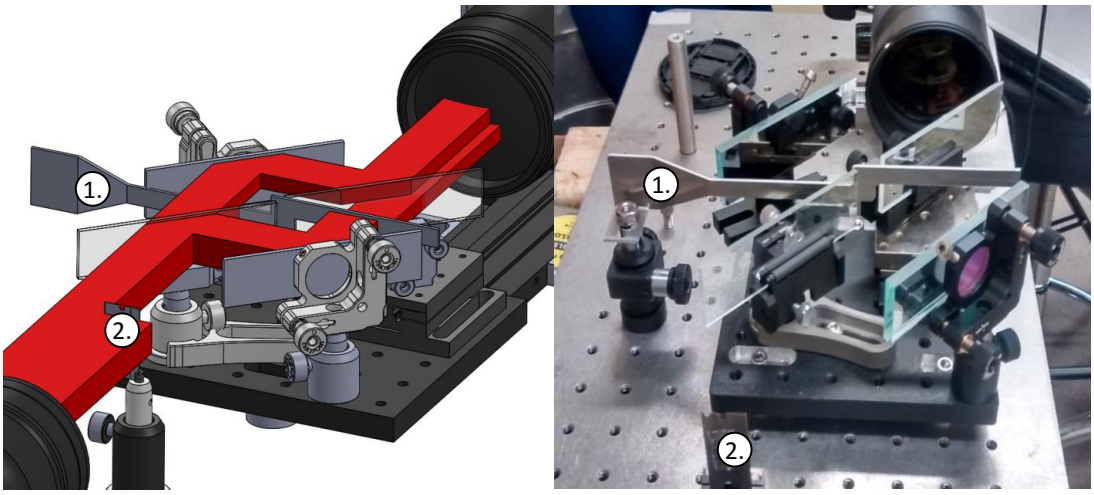

(c) CAD model and image of the interferometer with beam-blocker in place. The red solid on the left illustrates the collimated laser beam as it travels past the knife edge and through the beam-splitter. Note the displaced location of the top and bottom beams when they enter the lens

Figure 5-8

knife edge, there are additional edge diffraction patterns from the blocking plate as well as spherical diffraction patterns from imperfections in the optics. The combination of these unwanted patterns and speckle and noise make it difficult to track the location of the desired diffraction pattern in the raw image captured by the camera. An example of a raw image is included in Figure 5-9 (a).

To isolate the desired diffraction pattern, the images were smoothed in the vertical direction using a moving average filter. A comparison of a raw and smoothed image of the knife edge can be seen in Figure 5-9 (b) and (c) respectively. Row-by-row, the location of the brightest pixel was found. The target accuracy of 5 microns requires calculating the edge location to sub pixel accuracy, as such, a quadratic polynomial was fit to the points adjacent to the highest pixel value. The maximum value of this polynomial curve fit was then used to establish the location of the diffraction pattern in each row of the image. An example of the measured pixel values and the quadratic curve fit are shown in Figure 5-9 (c). The maxima in every row yield a curve which defines the location of the knife edge in the image. This procedure was performed on both the displaced and fixed images of the knife edge. The average distance between the two curves was taken as the beam displacement of the interferometer.

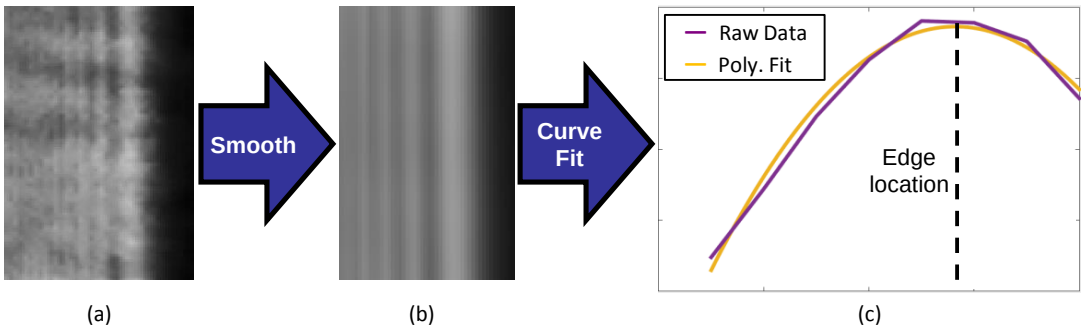

Figure 5-9: Image-processing required to determine displacement from the diffraction pattern illustrating the importance of the smoothing and curve fitting steps

The accuracy of this method was evaluated by calculating the displacement of the beam splitter for four different micrometer positions and comparing the linearity of the resulting measurements. The results from this test are outlined in Table 5.1. Maximum Error was 4.36 μm and average error was 3.5 μm. This is approximately

1/3 of a single pixel width exceeding the initial goal of <5 μm accuracy.

Table 5.1: Accuracy of knife-edge based measurement method

Micrometer Setting $[\mu m]$	**Calculated Displacement** $[\mu m]$	**Error** $[\mu m]$
0	0	0
50	47.12	2.88
100	103.26	3.26
150	154.36	4.36

5.2.4 Variation in Image Displacement

The procedure used to align the mirrors had an accuracy of approximately 300 μrad based on the limited length of optical lever that could be used in the confines of the test cell. Details on the alignment procedure for the interferometer are included in detail in Appendix B. These errors in initial setup and deflections of the beam splitters and the tilt used to achieve the carrier fringe pattern, resulted in a change in image displacement across the image of up to 50%. Variable beam displacement was not a problem, and was used as a way to adjust the sensitivity of the interferometer at different points in the nozzle. However, the requirement of <5 micron error in displacement established before had to be satisfied at all points in the image, requiring displacement measurement at multiple points. A method for determining this variation was developed to prevent displacement error being carried through to the density calculation process outlined below. Initially this was accomplished by executing the method outlined in Section 5.2.3 with a single knife edge at four locations spaced across the field of view. Figure 5-10 shows example images taken at four locations in the field of view.

Two images were taken at each location resulting in eight separate images that had to be saved and imported into MATLAB for post-processing. To simplify this process, a fixture to hold four separate knife edges at a predetermined spacing of 10mm was constructed. Four individual single-edge razor blades were cut down to

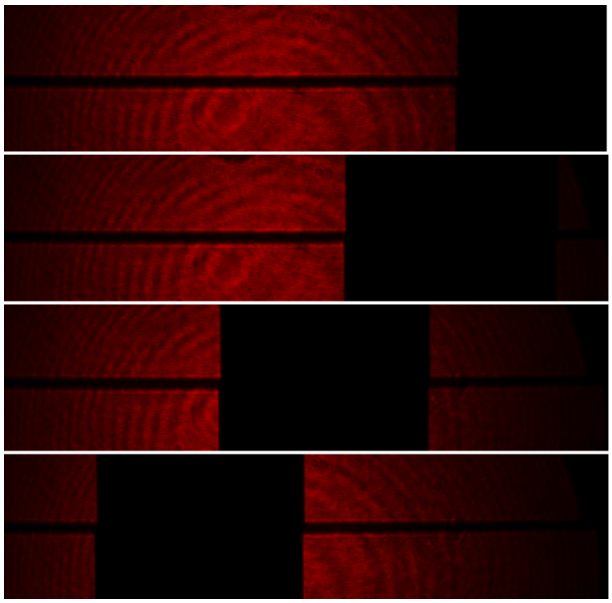

Figure 5-10: Images of the knife edge diffraction pattern taken at four different locations across the camera field of view

a width of approximately 8mm retaining their sharp edges. These four individual blades were epoxied into a block of aluminum with mounting slots to locate them. A picture of the multi-edge assembly and an example image using it is shown in Figure 5-11.

It was found that more than 4 data points were too widely spaced to capture the displacement measurements to the required 5 micron accuracy. By taking 4 separate images of the four blade knife edge fixture at a nominal spacing of 3mm, a total of 16 data points were taken, achieving the required accuracy across the entire field of view. These discrete data points were curve fit with a quadratic polynomial to yield image displacement as a function of horizontal location in the image. Figure 5-12 illustrates such a curve. This function was used in the integration process outlined in Section 5.3.

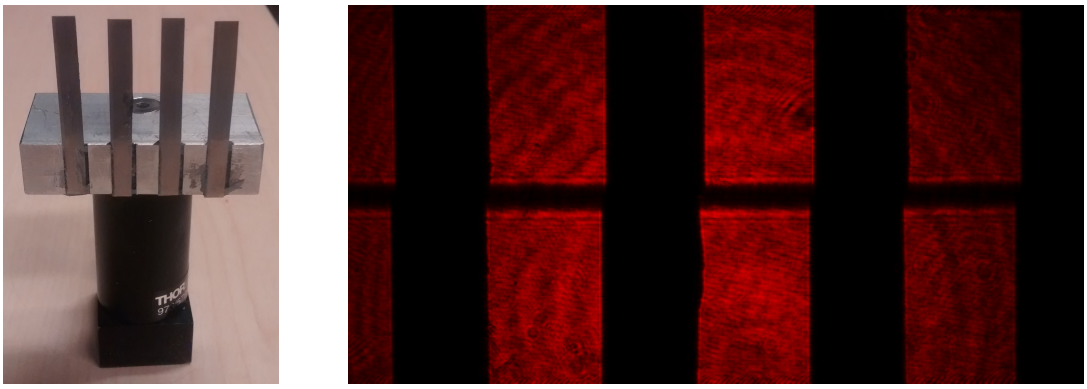

(a) (b)

Figure 5-11: Multi knife-edge fixture (a.) and resulting raw image (b.)

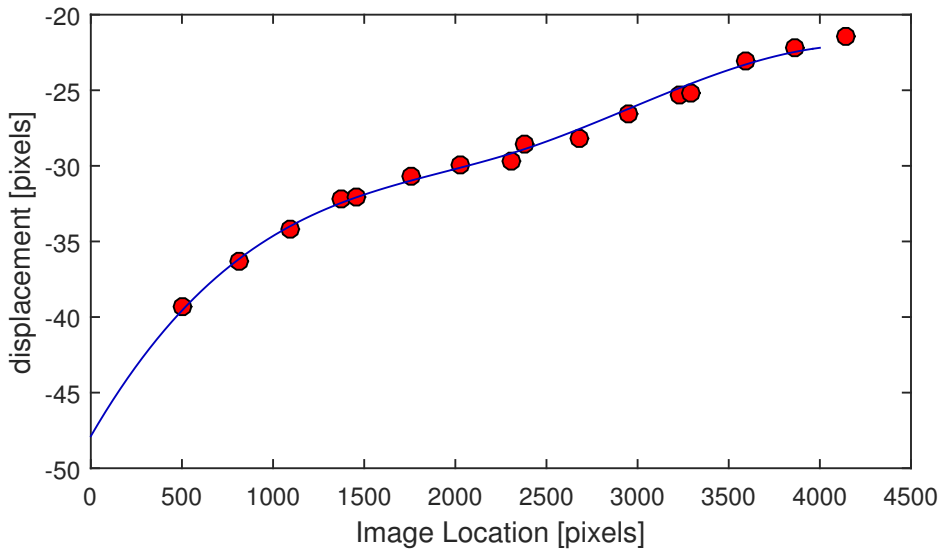

Figure 5-12: Plot of displacement across the entire camera field of view

5.3 Data Extraction Through Image Processing

For this research, the desired output of the interferometer was a 1-D centerline density measurement which could be compared with discrete density values calculated from measured wall pressures. The process outlined below can be extended to evaluate the full 2-D flow field, but this has not been attempted at this time. Calculating only 1-D data allowed for simplifications in the post processing procedure as averaging across the channel height could be used. The post-processing procedure was divided into two distinct sets of operations: FFT based image filtering and analysis to extract the desired phase information from the raw interference fringes, and a 1-D calculation of density from the extracted information. These two processes are covered in the following two sections.

5.3.1 Image Processing

Raw fringe images were post-processed using a Fourier transform based fringe analysis with the software Package UU [31]. The FFT filtering process removes the high frequency noise and speckle as well as low frequency modulations allowing for the isolation and extraction of the phase information at the relevant (carrier) frequency. This analysis technique as well as other relevant methods of fringe image analysis are outlined in detail in [24]. The key advantage of this method over fringe tracking/counting methods is the fact that it can be completely automated, requiring no human input or interpretation.

The raw fringe images were first cropped to a centerline strip of the nozzle and equalized along the length of the nozzle to bring the average brightness to a constant value yielding an image such as that seen in Figure 5-15a. The now equalized before, during, and after images of a given run were then combined into a single composite image. This was done to ensure that the FFT filtering process was identical for all images. An example composite image and the region in the nozzle from where it was cropped is shown in Figure 5-13

After equalization, the 2-D fast Fourier transform (FFT) of the image was taken

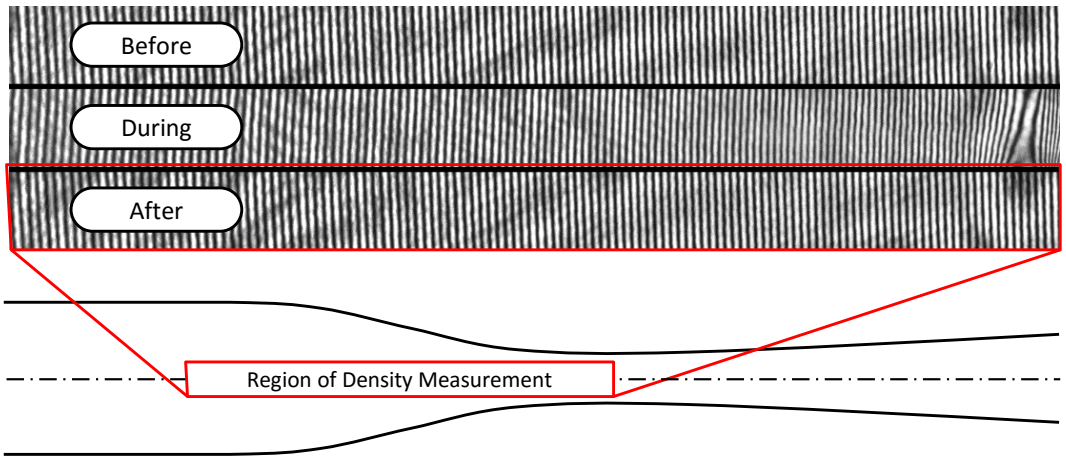

Figure 5-13: Nozzle crop location and resulting composite image

to convert from the spatial domain to the frequency domain. This resulted in three images: the imaginary and real components of the FFT and the FFT power spectrum (complex magnitude). To isolate the phase information in the desired frequency range, a Fourier coefficient pass window was used. The Fourier coefficients outside the pass window were set to zero eliminating them from the set of harmonics which represent the original image. A quantitative study on the size and location of the pass window, included in Section 5.3.2, found that a window height of 50% image height and a width and location which exactly contained the edges of the power band surrounding the carrier frequency yielded potential errors below 0.1%. Figure 5-14 shows the complete power spectrum in the top left and the pass window in the inset.

The inverse FFT (IFFT) was utilized to bring the now filtered set of Fourier harmonics from the frequency domain back to the spatial domain allowing for the calculation of image phase versus location. The IFFT was performed separately on the filtered imaginary and real parts of the FFT and the argument of the two taken yielding a discontinuous phase map (Figure 5-15b). Along any given row, the phase map resembles a sawtooth wave in the range of [0-2Π] as illustrated in Figure 5-16(b). The phase information needed was not the phase value in the images, but the difference between the during and after or during and before phase maps caused by the density gradient in the nozzle during the run. To facilitate subtraction between the two maps, A continuous phase map (Figures 5-15c, and 5-16(c)) was produced

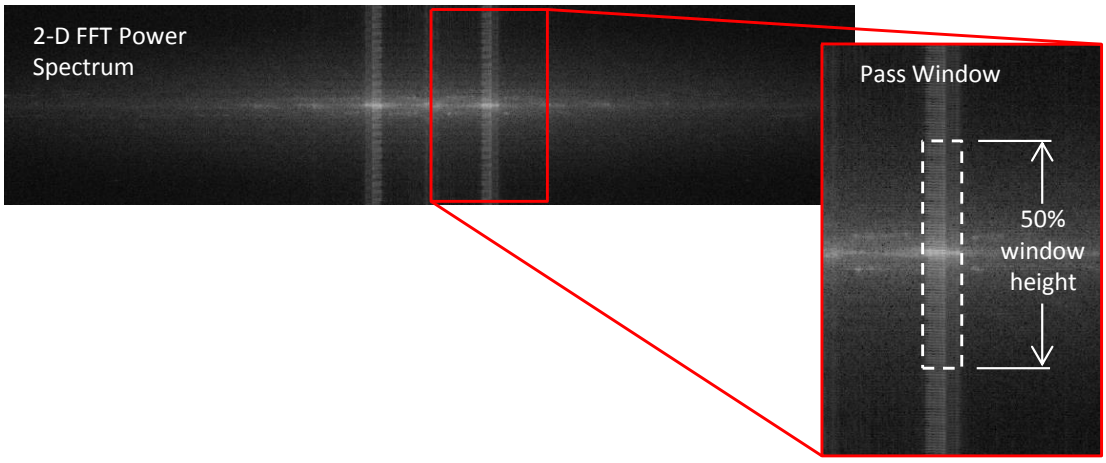

Figure 5-14: FFT power spectrum and filter window showing the well-defined bands at the spatial frequency of the carrier fringe pattern

by unwrapping the discontinuous map using the unwrapping feature of UU. The quality-guided unwrapping method was initially used, but was found to provide a poor result for the composite images yielding different unwrapped phase maps for the before and after images when they should have been effectively identical. To alleviate this issue, the simpler left-to-right method was chosen. In a more complex image, a quality-guided approach would be required, but for the simple 1-D nozzle flow, it was unnecessary. A progression of a no-flow images through the various stages of image processing is shown in Figure 5-15 for reference.

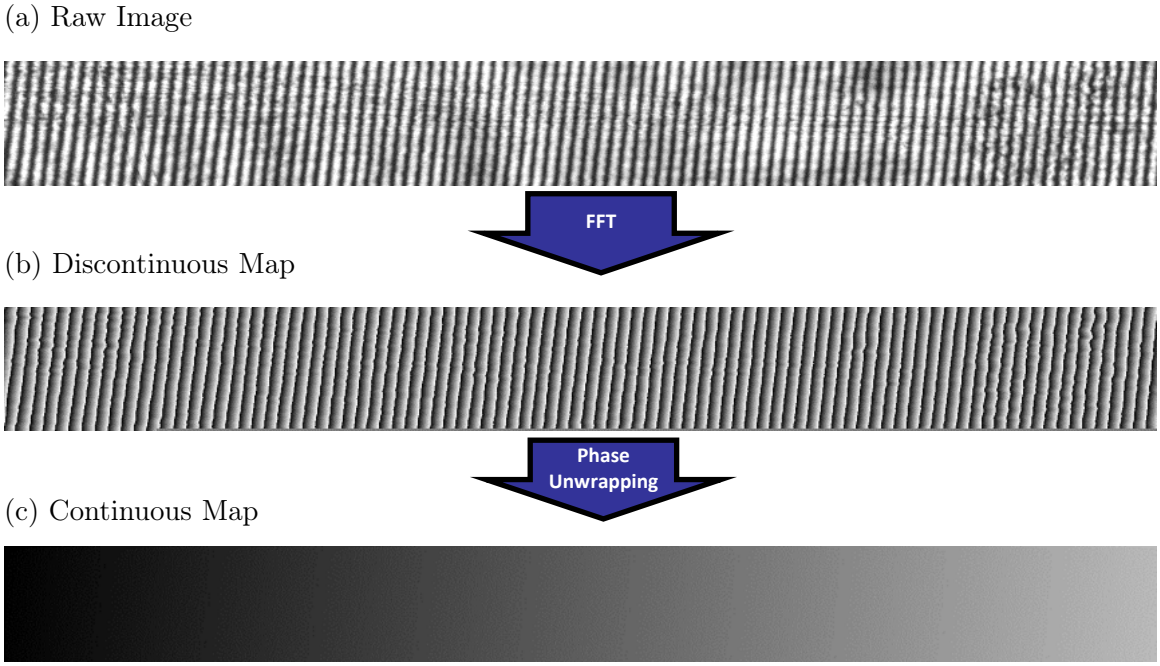

Figure 5-15: The steps of FFT image processing of interferometric images

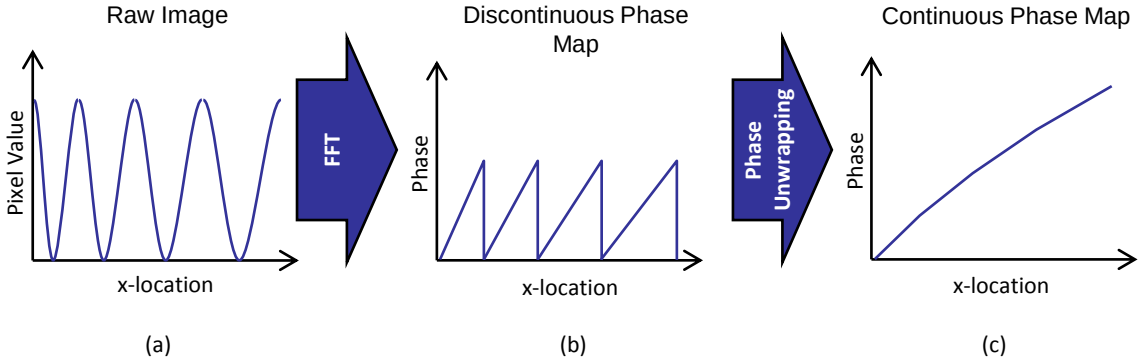

Figure 5-16: Qualitative 1-D Illustration of the fringe filtering and unwrapping process

5.3.2 FFT Window Sensitivity

One of the key sources of uncertainty in the post-processing procedure is the FFT filtering procedure. Consistent filtering was achieved by simultaneously filtering the before, during, and after images as one composite image, but defining the relevant frequencies from the image required further analysis. A quantitative approach was developed to determining the required filter window and assess the potential errors introduced by the filtering process. In the x-direction, the edges of the filter window were set at the edges of the power band surrounding the carrier frequency. The sharp edges of this band provided an unambiguous and repeatable reference for creating the pass window for all runs.

Without a natural boundary for the relevant Fourier information in the y-direction, a sensitivity analysis was used to establish the window height in the Y direction. Any of the three images are effectively 1-D since there is little cross-channel variation in the flow, especially at the centerline. However, in the composite image, the phase information at any given x-location resembles a square wave: similar constant values across the before and after images, with a different constant value across the during image. To determine the number of Fourier harmonics required to accurately capture this information, a 1-D analysis was performed. An illustration of this square wave concept is shown in Figure 5-17.

A 1-D square wave with the same vertical resolution was used as a surrogate for any given column in the composite image. An FFT was performed, and a subsequent IFFT was performed on an increasing number of Fourier harmonics. Figure 5-18 shows the original square wave and the resulting approximations using a selection

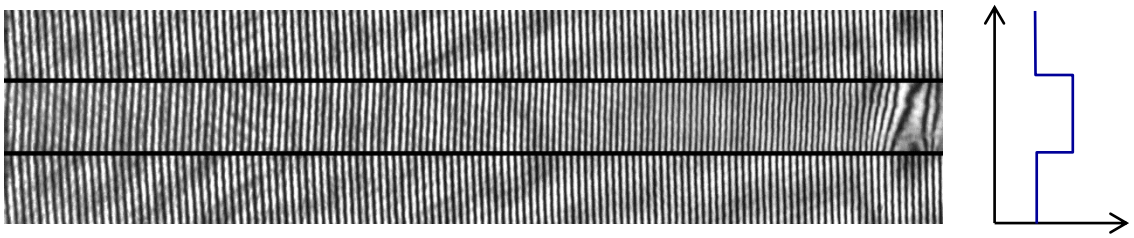

Figure 5-17: Qualitative illustration of the way in which phase information in the vertical direction is in the form of a square wave in the composite image

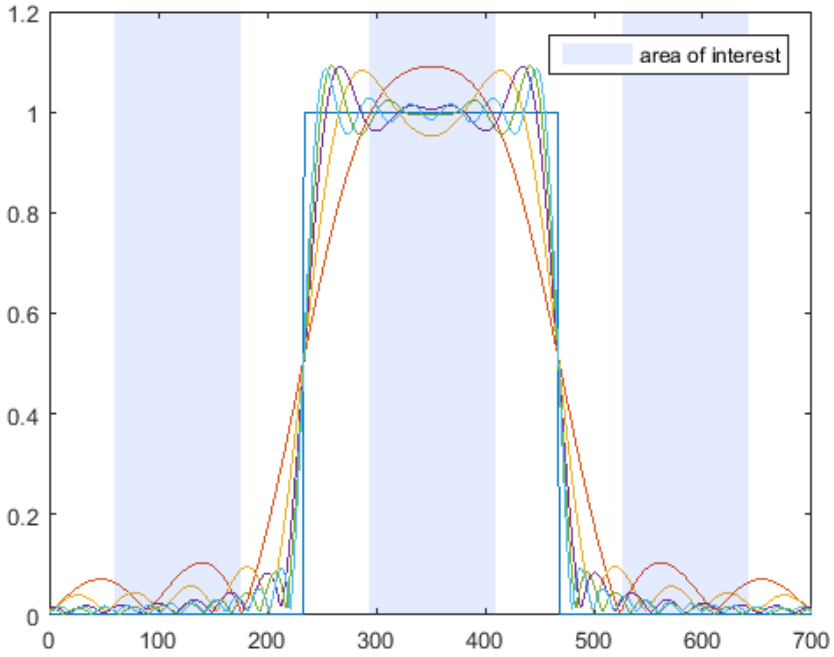

Figure 5-18: Square wave approximations using various numbers of Fourier harmonics used to determine the required height of the FFT pass window

of Fourier harmonics. The resulting filtered approximations were compared with the original square wave and the average error over the middle 50% of each strip was calculated. The resulting errors are plotted in Figure 5-19. It was found that the first 350 Fourier harmonics capture the original square wave to an accuracy of approximately 0.1 % which is of sufficient accuracy given the other sources of error in the density calculation process. This equates to a filter window half the height of the original power spectrum. This window height was used for all post processed results in this thesis.

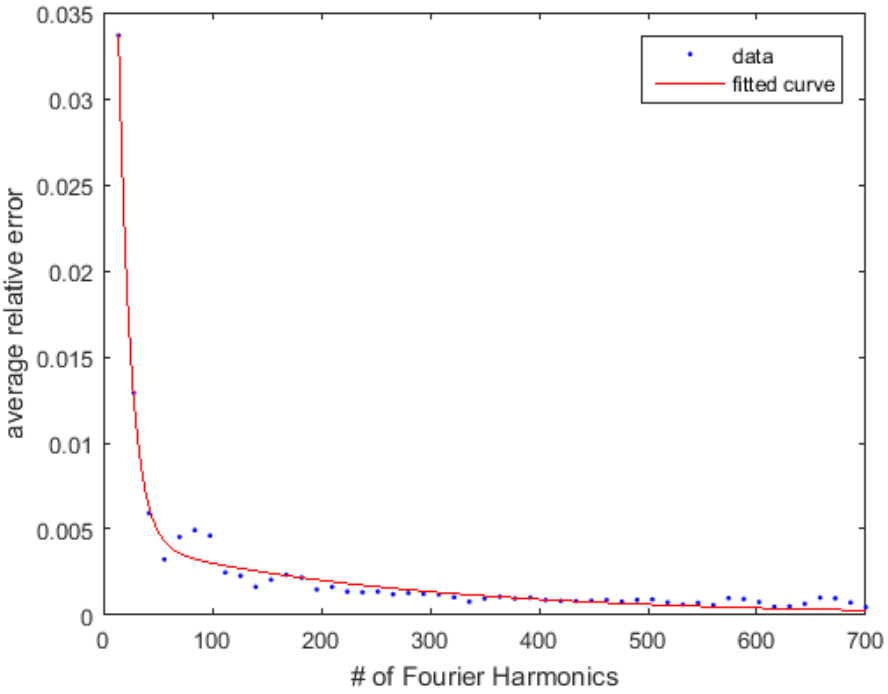

Figure 5-19: Square wave approximations error vs number of Fourier harmonics used resulting in the use of a 350 harmonic (50% height) pass window for all image processing

5.3.3 1-D Density Extraction with MATLAB

The three different phase maps (before, during, and after) were extracted the composite continuous phase map. Both the before and after maps represent the no-flow case; however the after image was exclusively used for all post processing for consistency. Comparison between using the before and after image showed less than 1% difference for all runs. From this point forward, any reference to the "no-flow" case is referring to the after image. The flow and no-flow phase maps were subtracted from one another yielding the derivative of optical phase difference due to the density gradient in the nozzle. This difference map was then average along the columns (channel height) resulting in a 1-D vector of phase lag values along the nozzle centerline.

By taking the difference between the flow and no-flow phase maps ($\Delta\Phi_{flow}$ and $\Delta\Phi_{noflow}$) and dividing by the spatial shift between the two images δ, the spatial derivative of phase lag was calculated via

$$\frac{\partial(\Delta\Phi)}{\partial x} = \frac{\Delta\Phi_{flow} - \Delta\Phi_{noflow}}{\delta}. \tag{5.1}$$

In the above equation, δ is not a constant, but a function of location. A polynomial fit of the measured displacement data similar to that shown in Figure 5-12 was used to calculate the displacement at every point in the image. Equation 5.1 yields a vector of phase lag derivative values at each point in the image. Trapezoidal integration was implemented to calculate the phase lag due to the density gradient in the nozzle. Using the wavelength of the laser λ_{laser} and the known optical path length at the initial location Δl_0, the phase lag $\Delta\Phi$ was converted to the optical path length difference l by

$$\Delta l = \frac{\Delta\Phi}{2\pi}\lambda_{laser} + \Delta l_0. \tag{5.2}$$

Using the physical path length through the test-Section w, and the definition of the index of refraction,

$$n = 1 + \frac{\Delta l}{w}, \tag{5.3}$$

the index of refraction at all points in the nozzle was determined. Finally, the Lorentz-Lorenz relation between refractive index and density,

$$\rho = \left(\frac{n^2-1}{n^2+2}\right)\left(\frac{3M}{4\pi\alpha N_A}\right), \tag{5.4}$$

was used to determine density ρ. The second quantity on the right-hand side which contains the molecular mass (M), mean polarizability (α), and Avogadro constant (N_A), is traditionally referred to as the Lorentz-Lorenz function, L [34]. For typical densities, this function can be considered a constant, but for the high densities of CO_2 near the critical point, a constant formulation introduced accuracies of up to 2%. In order to account for this, experimental data from both [34] and [10] were used to determine L as a function of index of refraction for densities from 10-1000 kg/m^3. The experimental data and the curve fit are shown in Figure 5-20. This changes the Lorentz-Lorenz equation from the simplified form,

$$\rho = L\left(\frac{n^2-1}{n^2+2}\right), \tag{5.5}$$

to a more accurate form with L as a function of n based on experimental data,

$$\rho = L(n)\left(\frac{n^2-1}{n^2+2}\right). \tag{5.6}$$

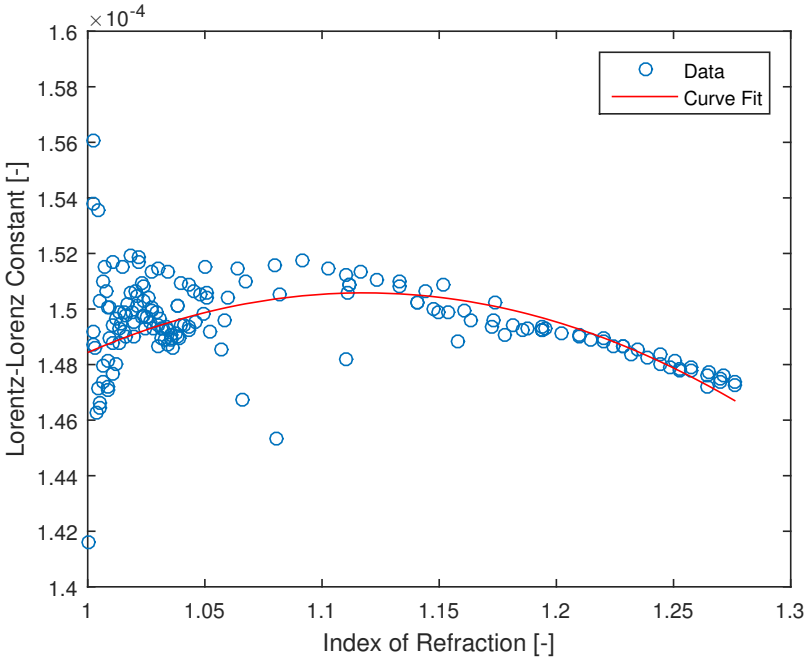

Figure 5-20: Lorentz-Lorenz function L as a function of index of refraction calculated from [34] and [10]

5.4 Summary

A novel shearing interferometer design was created to allow for the measurement of the density of CO_2 for both equilibrium and metastable flows in a converging diverging nozzle. Interferometer sensitivity was adjustable allowing for density measurement in the range of 10-1000 kg/m^3. Error analysis showed less than a 1% error in density introduced by the image FFT post processing and data extraction method. 1-D centerline density distributions were calculated from 2-D fringe images by averaging across the channel height of a centerline strip equal to the height of the throat. The thermodynamic state calculated from interferometer derived density measurements are compared with those calculated from wall pressure measurements to assess the performance of different metastable property extrapolation methods in Chapter 7.

Chapter 6

Test Rig Operation

The key challenges in running the test rig were determining the uncertainty in total conditions and synchronizing the pressure and density measurements. Characterization of the uncertainties in the tank conditions and a method of determining nozzle total conditions through 1-D compressible flow were used to limit the maximum error in the tank and nozzle entropies throughout the blowdown runs to 0.3 and 1.3% respectively. Synchronization of the pressure and density measurements was achieved to microsecond accuracy through closed loop control of the camera. The details of the above solutions as well as other challenges encountered while running the test rig are covered in this chapter.

6.1 Synchronization of Test Rig Measurements

As a blowdown facility, the behavior of the CO_2 test rig is fundamentally unsteady. In order to produce meaningful data, all measurements must be synchronized. Static pressure and density in the nozzle as well as tank total conditions are all dynamic, and as such, the relative time at which measurements are made must be known. With total conditions changing at up to 3% per second over a nominally 1 second blowdown, mismatch between data points due to incorrect time sampling can be significant. Synchronization was achieved by sampling all sensors at the same frequency (10 kHz) starting at the same time. This ensured that any points at a certain time step in the

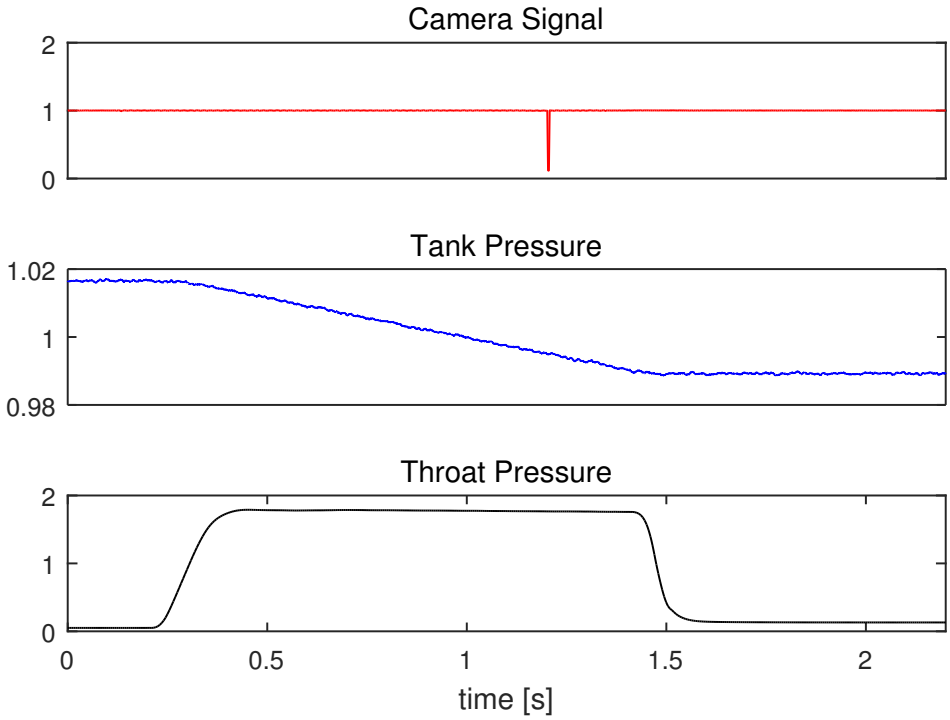

Figure 6-1: Typical blowdown showing the valve opening and closing as well as the camera trigger

resulting data could be compared.

To synchronize the single image taken by the interferometer with the high speed data, a separate channel was added to allow for the tracking of the time instances when the camera shutter opened and closed. This was accomplished by logging the camera's external flash trigger. This provided microsecond accuracy between the measured pressures and density. Figure 6-1 shows a time history of a representative nozzle static pressure, tank total pressure, and camera signal for a typical 1.2 second blowdown. All quantities have been non-dimensionalized by their mean values to facilitate comparison of their relative changes throughout the run.

6.2 Determination of Tank Total Conditions

The tank total conditions were measured using three properties: temperature, using both external and internally mounted thermocouples, pressure, using a pressure

transducer, and density, through a load cell determining CO_2 mass and the known tank volume. A sensitivity study was carried out to determine the uncertainty of the true total conditions for different combination of measured total conditions. Table 6.1 contains information on the sensors used and their respective accuracies.

Table 6.1: Sensor models and uncertainties

Property Measured	Sensor Model	Uncertainty
Temperature	Omega: KQXL-116U-12	0.25 K
Pressure	Omega: PX409-2.5KGV	0.1 bar
Mass	Omega: LC501-2K	1.2 kg

During a run near the critical point, the temperature, pressure and density were recorded. All combinations of two properties were taken and the third calculated using RefProp. It was found that temperature calculated from the measured density and pressure produced the best agreement with the measured value. The results of this study are shown in Table 6.2.

Table 6.2: Summary of calculated errors for different measured total properties: (T = 309.77 K, p = 87.7 bar, ρ = 605 kg/m^3)

Properties Taken as True		Calculated Property	% Error
ρ	T	p = 88.6 bar	1%
ρ	p	T = 309.4K	0.12%
p	T	ρ = 591.7 kg/m^3	2.2%

The above results were taken directly above the critical point where the high total density (609 kg/m^3) lead to a mass of CO_2 representing approximately 20% of the total tank mass. To ensure that the most accurate method of determining total conditions was used for all total conditions, an error analysis was performed for the entire range of entropies seen in a typical set of blowdown runs. With three available thermodynamic properties in the tank (p, ρ, T) and two needed to fully

characterize the state, there were three possible pairs of properties that could be used to determine the desired property of entropy: ρ-p, ρ-T, and T-p. The uncertainties in entropy calculated from these three property pairs at 315K and a range of typical tank entropies were determined by perturbing the theoretical conditions and recording the deviations in Figure 6-2 shows that above and below a reduced entropy of 1.16, ρ-p and T-p respectively yield the lowest uncertainty in calculated entropy. ρ-T produced higher uncertainty than one of the other pairs at all point, but is included for completeness. It should be noted that the intersection of all three curves at a single point is purely coincidental.

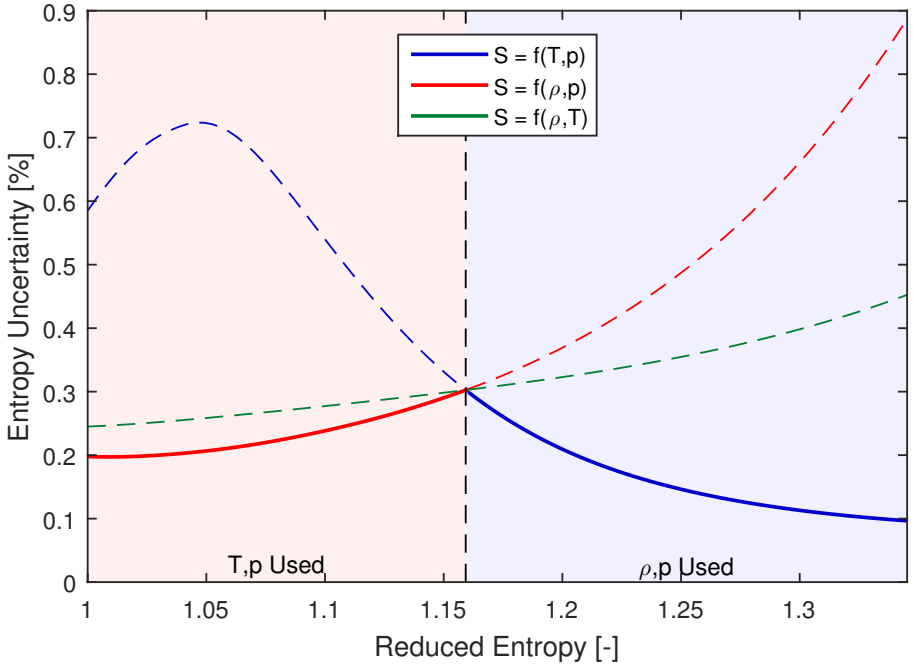

Figure 6-2: Uncertainty in tank entropy for a range of reduced entropies showing the benefit of a pressure-temperature based measurement at high entropies vs. a pressure-density based measurement at low entropies

The entropy could only be determined at the start of the run as only the tank pressure could be monitored during the blowdown process. The response time of the thermocouple was too slow to maintain an accurate measurement of the total temperature in the tank and the load cell was inaccurate due to forces on the tank while connected to the test section. To allow determination of the total conditions at

all points, it was assumed that the tank was isentropic throughout the blowdown. To confirm this assumption, an experimental confirmation was carried out. The initial and final masses and pressures of the tank during a blowdown run were recorded. Using the density calculated from the tank mass and the measured temperatures initial and final entropies were calculated. A deviation in entropy of less than 0.1% was shown for all runs leading to the confirmation of an isentropic tank.

Using the constant known value of entropy in the tank, and the assumption of an adiabatic blowdown, the total enthalpy was calculated at every instant in time using the 10kHz recorded tank total pressure and the SW EOS through RefProp.

$$H_t(t) = SW(S_{tank}, p_{tank}(t)) \tag{6.1}$$

6.3 Determination of Nozzle Total Conditions

In the first generation rig, it was assumed that entropy was constant between the tank and the nozzle [50]. It was found that this was not the case for the second generation rig, with runs showing up to a 4% drop in total pressure from tank to nozzle inlet. This was caused by two changes to the rig: the introduction of additional upstream components (illustrated in Figure 6-4), and the higher upstream Mach numbers resulting from a larger throat cross section; $M_{inlet} \simeq 0.15$ in the current rig, $M_{inlet} \simeq 0.05$ in the first generation rig.

A new method was developed to determine the total conditions in the nozzle using relevant upstream and downstream measurements. The following assumptions were made for this method:

- Adiabatic flow at all points from charge tank through nozzle outlet
- Isentropic and one-dimensional flow in the test section

Details on the calculations supporting these assumptions can be found in [50].

The key unknown in the test rig was the entropy generated in the ducts, valves, and other components upstream of the nozzle which was manifested as a loss of

total pressure from tank to nozzle. The measured static pressures in and the known geometry of the nozzle were exploited to determine the total pressure in the nozzle.

Assuming quasi-steady flow, mass conservation dictates that mass flow is identical at all nozzle stations;

$$\dot{m}(const.) = \rho u A. \tag{6.2}$$

The definition of total enthalpy,

$$h_t = h + \frac{u^2}{2}, \tag{6.3}$$

allows for a constraint between static and total enthalpy and the velocity.

Using the static pressure values and cross sectional areas at any two nozzle stations along with equations 6.2 and 6.3, the following system of equations can be constructed:

$$\dot{m} = \rho_1 u_1 A_1 = \rho_2 u_2 A_2 \tag{6.4a}$$

$$h_t = h_1 + \frac{u_1^2}{2} = h_2 + \frac{u_2^2}{2} \tag{6.4b}$$

$$S = SW(p_t, h_t) \tag{6.4c}$$

$$h_1 = SW(p_1, S) \tag{6.4d}$$

$$h_2 = SW(p_2, S) \tag{6.4e}$$

$$\rho = SW(p_2, S) \tag{6.4f}$$

Equations 6.4(a,b) are equations 6.2 and 6.3 applied to two specific nozzle stations, while equations 6.4(c-f) are simplified representations of the SW EOS through RefProp. This system is solved iteratively by guessing a total pressure, establishing the

total conditions through RefProp, and then checking for violation of mass and energy conservation.

This process was carried out for every possible combination of the 5 Kulite locations in the converging section. It was found that Kulites 1-3 produced the most repeatable and consistent results with typical discrepancies in the calculated total pressure of 0.1% or less. The average of the three total pressures calculated from these Kulites was used as the accepted value for all later calculations.

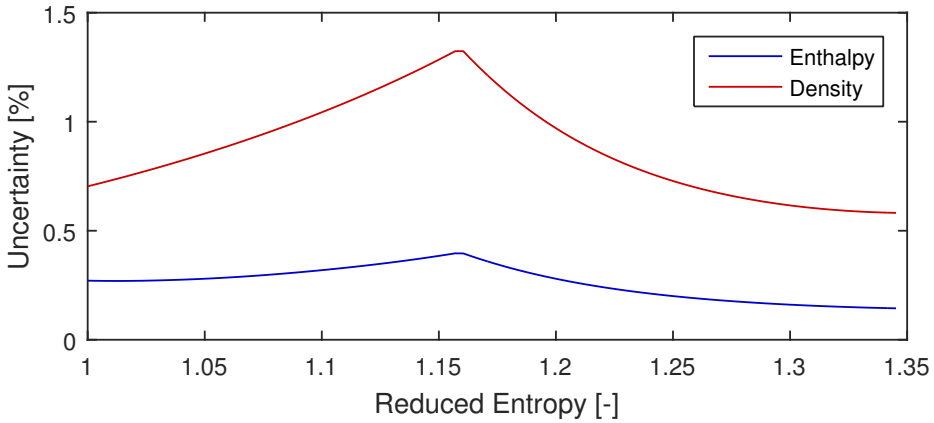

Figure 6-3: Uncertainty in test rig total enthalpy and nozzle total density resulting from the errors in nozzle total pressure and tank total entropy determination.

The key parameter that was needed in the nozzle is the density in the constant area inlet as this was used for the constant of integration in determining the density distribution as outlined in Chapter 5. The errors from both the nozzle total pressure determination and tank total enthalpy determination above. These errors were carried through a total density calculation for the same range of reduced entropies considered in Figure 6-2 which results in the plot shown in Figure 6-3. Due to the high sensitivity to density near the vapor dome and the compounding nature of the errors, the worst case uncertainty in density is quite high; approximately 1.4% at the maximum value. It should be noted that this is a worst-case scenario, and the agreement of the experimental data covered below suggests that the real-world errors are significantly lower.

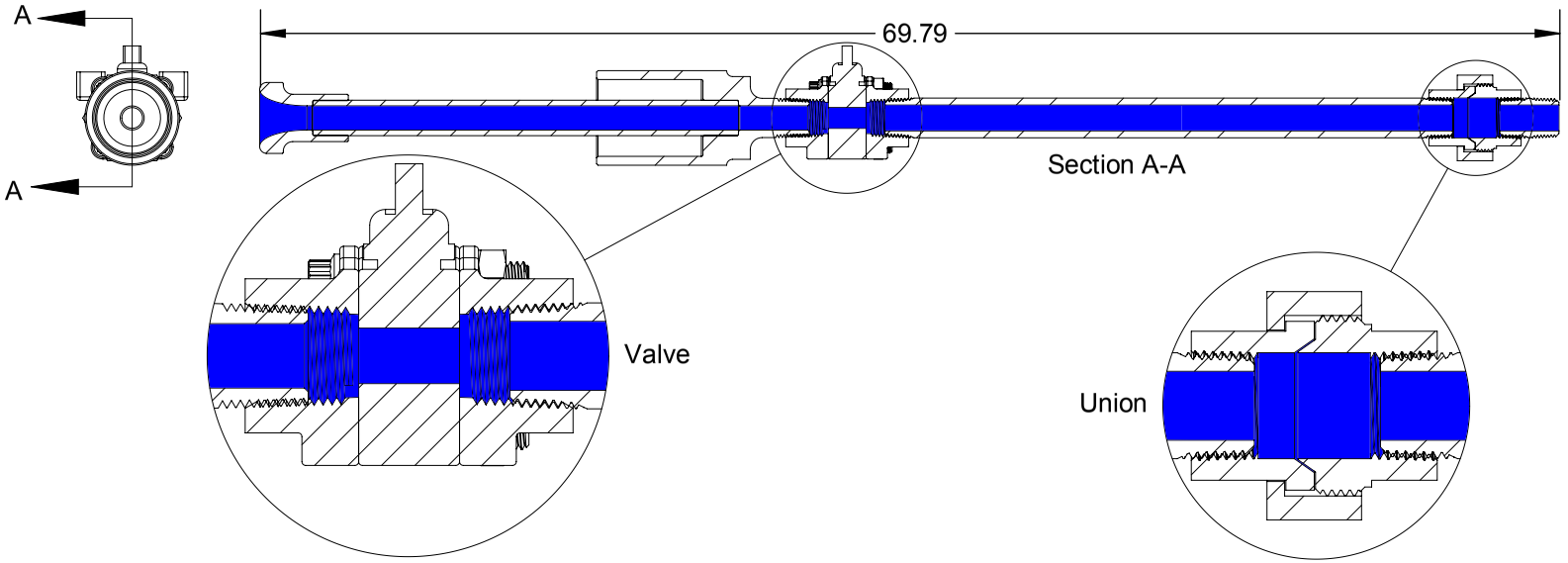

(a) Illustration of area discontinuities at nozzle (center) and union (right)

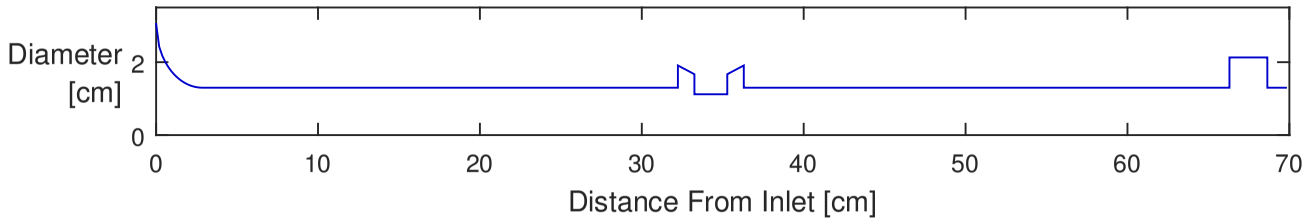

(b) quantitative data on diameter discontinuities

Figure 6-4: Area discontinuities in the upstream components which result in significant total pressure drop from tank to nozzle

6.4 Challenges

6.4.1 Cavitation in CO_2 Transfer Pump

The change from high pressure 50 lb. cylinders to low pressure 180 L Dewars for CO_2 storage and the addition of a liquid CO_2 pump for filling greatly reduced the time needed to fill the tank (roughly 2 hours compared with the original fill time of 2 days), but the new procedure introduced unforeseen challenges. A liquid Dewar stores CO_2 as a two phase mixture at a temperature significantly below ambient. While the container is vacuum sealed, inevitable heat loss leads to the need for small amounts of the liquid CO_2 to be boiled off to maintain temperature. Because the fluid is on the saturated vapor curve, there is no margin on cavitation and as such, any heat addition or pressure loss from the hoses connecting the Dewar to the pump will immediately cause the fluid to vaporize and prevent the positive displacement pump from functioning.

This phenomenon was discovered after installing the pump, so it was desirable to alleviate the issues without major modifications to the CO_2 plumbing. The pump manufacturer recommended either a chiller or a small vane pump between the Dewar and piston pump, both costly options. To provide a quick solution to the problem, a new filling procedure was implemented. Before pumping, the Dewar was purged to allow a portion of the liquid to vaporize and to bring the equilibrium temperature and pressure down to approximately 24 bar and 260 K. To provide a margin on cavitation, a separate cylinder of CO_2 at approximately 60 bar and 295 K (ambient) was used to back-pressure the Dewar through the vent. Sufficient flow rate of the CO_2 was achieved such that the pressure was maintained at a regulated 30 bar.

6.4.2 Mach Waves in Diverging Section

Initial testing of the test rig away from the critical point and without phase change showed distortion of the interferometer fringes in the diverging section of the nozzle. Initially it was thought that this was due to leakage past the expanded Teflon seals into

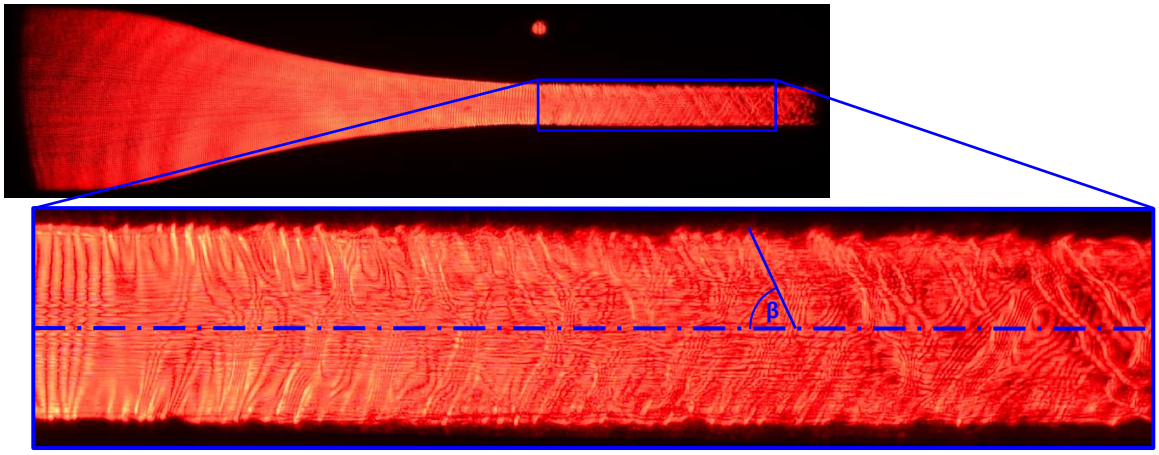

Figure 6-5: Nozzle image with Mach waves evident in the diverging section

the low-pressure diverging section, but the addition of a redesigned sealing interface using an o-ring failed to show an improvement in the downstream image quality. After noting the angular nature of the disturbances, it was hypothesized that the disturbances were due to Mach waves resulting from surface imperfections in the nozzle.

The angle of the disturbances in the image were recorded and were compared with the limiting oblique shock angle β for the theoretical Mach number at that point in the nozzle. The Mach number distribution was calculated from a simple 1-D constant n_s isentropic blowdown. Figure 6-5 illustrates the wave angles measured in the image, and Figure 6-6 shows the comparison between these measurements and the theoretical wave angle based on Mach number. The good agreement between the two confirms the presence of Mach waves in the diverging section.

The nozzle inserts were anodized black after machining, preventing them from being polished to reduce the strength of the Mach waves. The degree to which the surface needs to be polished to prevent distortion of the fringes is unknown and should be investigated in future work.

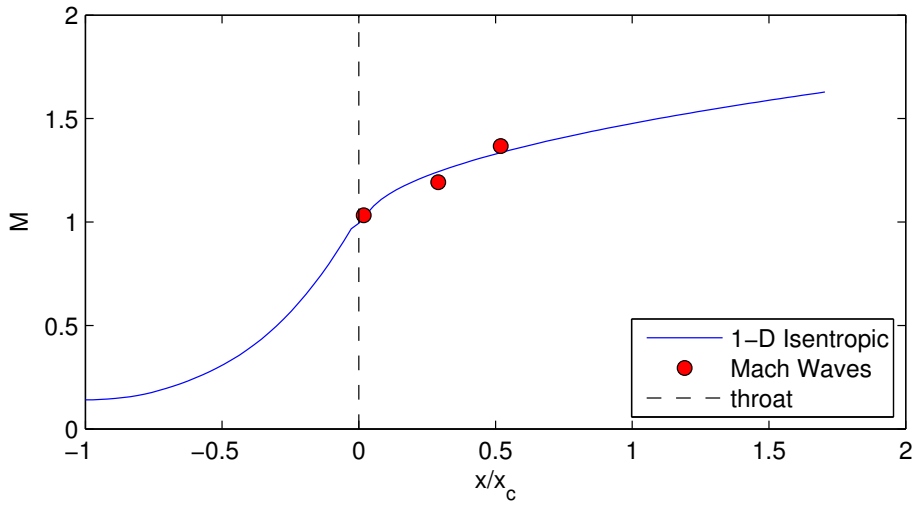

Figure 6-6: Comparison between measured Mach wave angle and theoretical angle calculated from 1-D isentropic blowdown

Chapter 7

Assessment of Non-Equilibrium Condensation Behavior

The main goals of this research were to determine the accuracy of tabular and EOS based metastable property extrapolation and to assess the Wilson line for CO_2. The former was successful away from the critical point where a large metastable region below the vapor dome allowed for direct comparison between measured and extrapolated metastable properties. The errors in EOS based extrapolation in this region were found to be below 2% while tabular extrapolation showed large errors of up to 15%. Near the critical point, the vanishing metastable region in EOS based extrapolation and the influence of high property gradients in the tabular extrapolation made valid comparisons between extrapolated and experimentally measured properties impossible. The Wilson line was derived from the degree of subcooling observed in a set of blowdown runs across a range of reduced entropies. These results were non dimensionalized and curve fit yielding a continuous Wilson line in T-s coordinates. This continuous line was used to establish a new, experimentally derived condensation limit for compressor operation.

7.1 Outline of Run Total Conditions

Two sets of blowdown runs are analyzed below. A set of runs in which pressure, density and condensation location were all measured, and a second set of runs to look at the condensation front location and shape in detail (denoted Sets I and II respectively). Both sets of runs were made from the same nominal total conditions: 8 equally spaced points ranging from a reduced entropy of 1 to approximately 1.3 and all at a reduced temperature of 1.04 (315 K). Achieving the exactly desired total conditions was impossible due to the unknown total pressure drop in the upstream components and the sensitivities due to real gas effects near the critical point. The unequal spacing in the resulting nozzle total conditions is illustrated in Figure 7-1. Note that the arrows starting at each total condition point are of an arbitrary length and are only meant to illustrate the thermodynamic process through the nozzle qualitatively. Quantitative information on the total conditions for all 16 runs in Set I is shown in Table 7.1. Errors in the acquisition of static pressures in set II led to their use only for qualitative analysis of the boundary layer shape outlined in Section 7.5.2

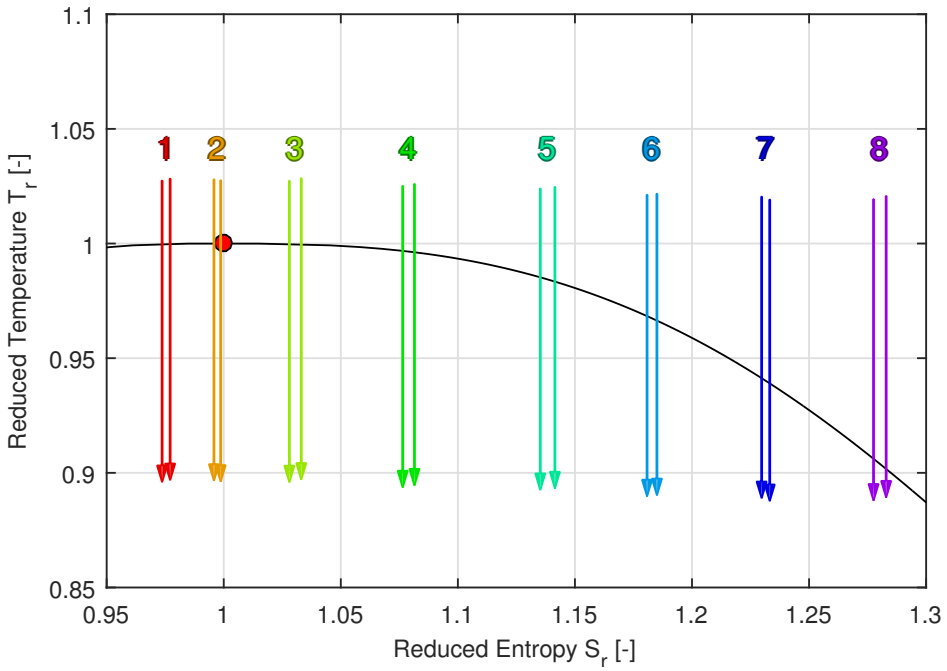

Figure 7-1: T-S Diagram of total conditions showing close grouping between successive runs at each set point

Table 7.1: Set I. Total Conditions

Run Number	**Dimensional Total Conditions**			**Reduced Total Conditions**		
	Temperature $[K]$	Pressure $[bar]$	Entropy $[J/kg \cdot K]$	$T_r[-]$	$p_r[-]$	$S_r[-]$
1a	312.5	92.61	1396	1.027	1.255	0.974
1b	312.7	92.84	1401	1.028	1.259	0.977
2a	312.6	90.67	1428	1.028	1.229	0.996
2b	312.5	90.14	1432	1.028	1.222	0.999
3a	312.4	88.01	1474	1.027	1.193	1.028
3b	312.8	88.36	1481	1.028	1.198	1.033
4a	311.8	84.34	1543	1.025	1.143	1.076
5b	312.0	84.44	1550	1.026	1.145	1.081
5a	311.4	79.93	1627	1.024	1.083	1.135
5b	311.6	79.66	1636	1.025	1.080	1.141
6a	310.6	74.46	1693	1.021	1.009	1.181
6b	310.7	74.11	1699	1.022	1.005	1.185
7a	310.3	67.64	1763	1.020	0.917	1.230
7b	309.9	66.77	1768	1.019	0.905	1.233
8a	310.0	59.45	1832	1.019	0.806	1.278
8b	310.4	58.81	1839	1.021	0.797	1.283

7.2 Assessment of Interferometry for Metastable Density Measurement

To compare the pressure measurements made at discrete points along the nozzle with the continuous centerline density measurements, the SW EOS implemented through RefProp was used to calculate point density values from the known entropy calculated using the method outlined in Section 6.3 and the measured pressure. Using this method, shearing interferometry was successful in measuring the equilibrium density to within the uncertainty outlined in Figure 6-3 plus that of the density post-processing method for all run conditions in Set I

With results on the accuracy of interferometry for measuring the equilibrium density of CO_2 near the critical point, the comparison was extended into the metastable region where both the extrapolated SW EOS and tabular extrapolation methods outlined in Chapter 2 were evaluated.

7.2.1 Comparison Near the Critical Point

Interferometry showed limited value for validating the metastable extrapolation methods outlined in Chapter 2 near the critical point. For runs 1-4, the vanishing region of metastable properties that could be calculated using the extrapolated SW EOS prevented any direct comparisons between measured density and calculated values. While use of extrapolated values generated by the lookup method outlined in Chapter 2 allowed comparison at any conditions, even those past the spinodal limit, the calculated properties showed inconsistencies as outlined in the condensation onset analysis in Section 7.3. Further attempts were made to use tabular extrapolation as outlined in Chapter 2 and utilized in [50] and [29], but this method showed errors up to 15% even with modest excursions into the metastable region. Figure 7-2 illustrates typical errors for the tabular extrapolation method with results from Set 1 run 6a. With these large errors when compared with RefProp calculated metastable properties, the SW EOS was used for all calculations of the Wilson Line below.

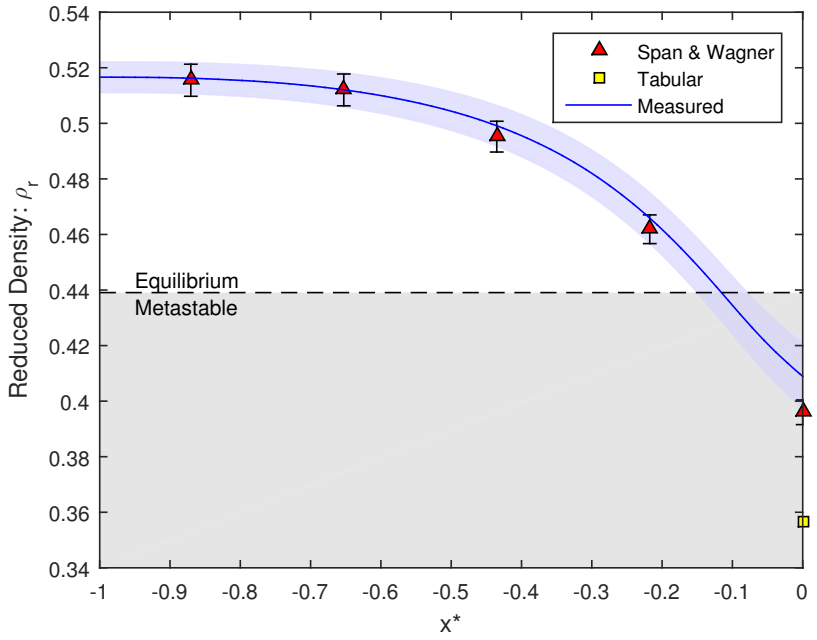

Figure 7-2: Comparisons between measured density and those calculated from both the SW EOS and from the tabular extrapolation discussed in Chapter 2 for run 6a yielding errors of up to 15%

7.2.2 Comparison Away from the Critical Point

Away from the critical point (runs 5-8), the errors between measured and calculated metastable density are of similar magnitude to those of equilibrium vapor ($<$2%). At the highest entropy runs (7-8), the interferometric data was used to demonstrate a maximum error of approximately 0.5% in the metastable region. Runs 4 and 5 did not have a Kulite pressure measurement in the metastable region to which the density could be compared. While two data points does not represent a rigorous assessment of the accuracy of the metastable properties extrapolated from the SW EOS, the successful use of a similar methodology for the calculation of metastable steam properties led to further confidence in its use for the condensation assessment below.

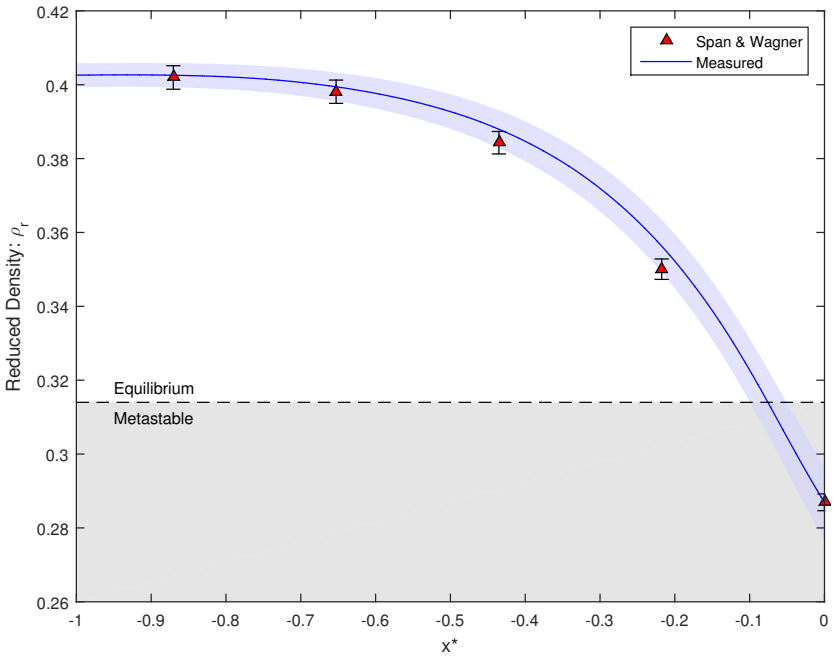

(a) Set I run 7b

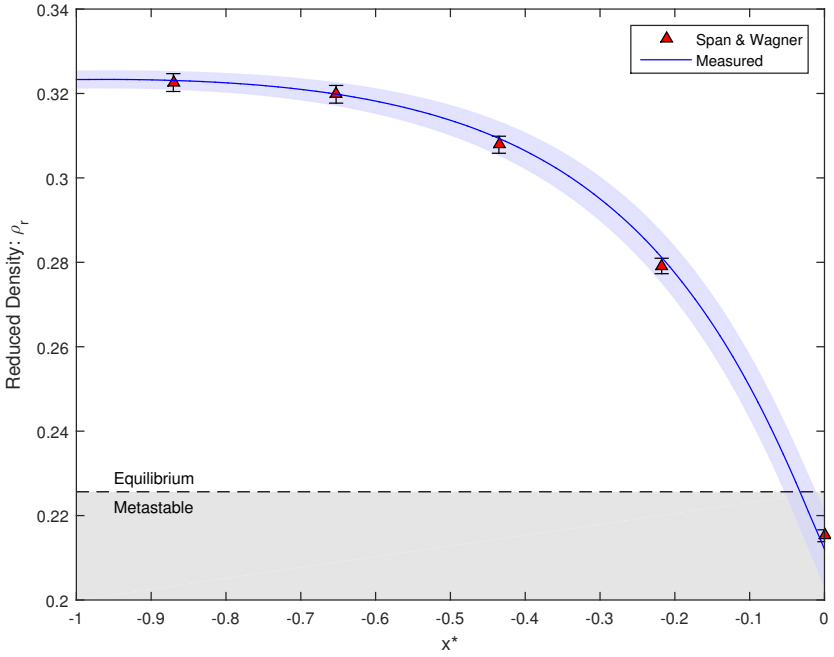

(b) Set I run 8a

Figure 7-3: Comparison between measured density and that calculated by the SW EOS for both equilibrium and metastable conditions away from the critical point yielding errors less than 2% for run 7b (a) and 0.5% for run 8a (b)

7.2.3 Conclusions and Further Work on Metastable Properties

The best agreement between experimental values and those calculated from RefProp were found at the highest entropy runs (furthest away from the critical point). The maximum entropies seen in sets I and II were limited to values relevant to a supercritical CO_2 compressor, but future work could include higher entropy runs with larger excursions into the two phase dome, and a more complete assessment of EOS based metastable property extrapolation using the SW EOS. Further recommendations to improve the accuracy of the density measurement through absolute density measurement, higher total conditions, and modified nozzle geometries are given in Chapter 8.

7.3 Experimentally Derived Wilson Line for CO_2

One of the key goals of this research was to identify the condensation limit for CO_2 for total conditions Representative of a typical compressor. The limit of spontaneous condensation for a supersaturated metastable vapor is known as the Wilson line, named after C.T.R. Wilson who published the first controlled measurements of spontaneous condensation in water vapor [49]. The Wilson line for CO_2 was determined by tracking the location of the condensation front in the nozzle and determining the local static pressure at that point using interpolation between the two adjacent discrete static pressures. This method is illustrated in Figure 7-4.

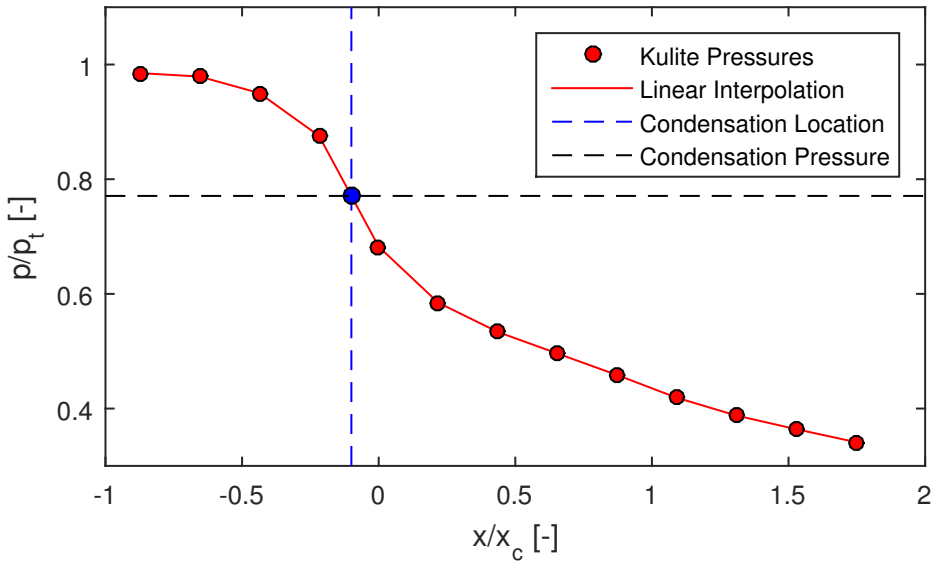

Figure 7-4: Qualitative illustration of the method used to establish the pressure at condensation onset

To nozzle entropy, known from the total conditions, and the pressure calculated using the above method fully defined the state of the fluid prior to condensation. The tabular method outlined in Chapter 2 was used to determine the temperature from the entropy and pressure allowing the flow condensation conditions for all 16 runs in set I to be plotted on a T-S diagram shown in Figure 7-5 To the authors knowledge, this represents the first experimentally derived measurement of the Wilson line for CO_2.

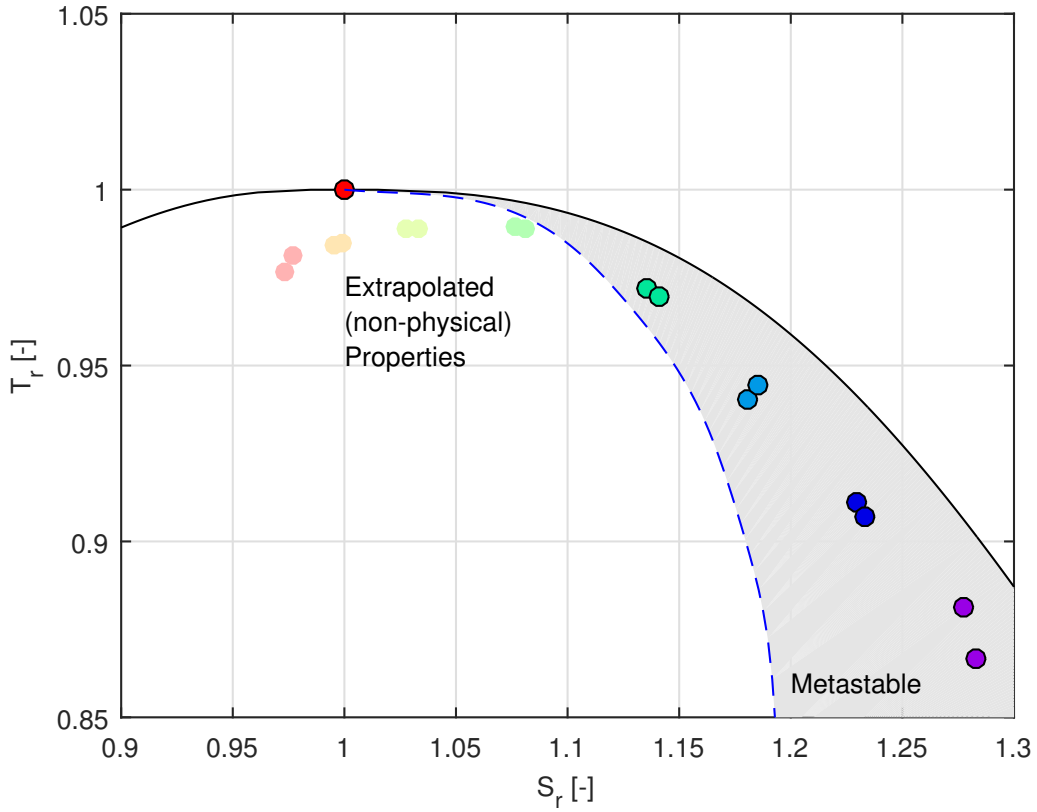

Figure 7-5: Condensation conditions for all runs in set I showing larger and larger excursions into the two phase dome as the total conditions increase in reduced entropy

Runs 1-4(a,b) show condensation limits inconsistent with traditional non-equilibrium condensation theory. The spinodal limit on the vapor side is shown in both Figure 7-7, however the accompanying spinodal limit on the liquid side is not included. Both these limits must coincide at the critical point, leading to a vanishing metastable region there. Because of the lack of metastable properties from the extrapolated SW EOS, the condensation pressures for runs 1-4 were calculated from the extrapolated, non-physical properties described in Chapter 2.

Runs 5-8(a,b) and to some extent, run 4 due to its vicinity to the SW spinodal limit, follow a much more traditional pattern of increased subcooling before condensation as the total conditions move away from the critical point. The degree of subcooling is defined as

$$\Delta T_{sub} = T_{sat.}|_s - T_{cond.}|_s \tag{7.1}$$

This value can be non-dimensionalized by the critical temperature

$$\Delta T^*_{sub} = 1 - \left(\frac{T_{sat.}|_s}{T_{cond.}|_s} \right), \tag{7.2}$$

which is plotted against reduced entropy in Figure 7-6. With the intercept set at the critical point, the degree of subcooling seems to follow a linear trend with entropy. This linear fit is used to plot a continuous Wilson line on a T-s diagram in Figure 7-7.

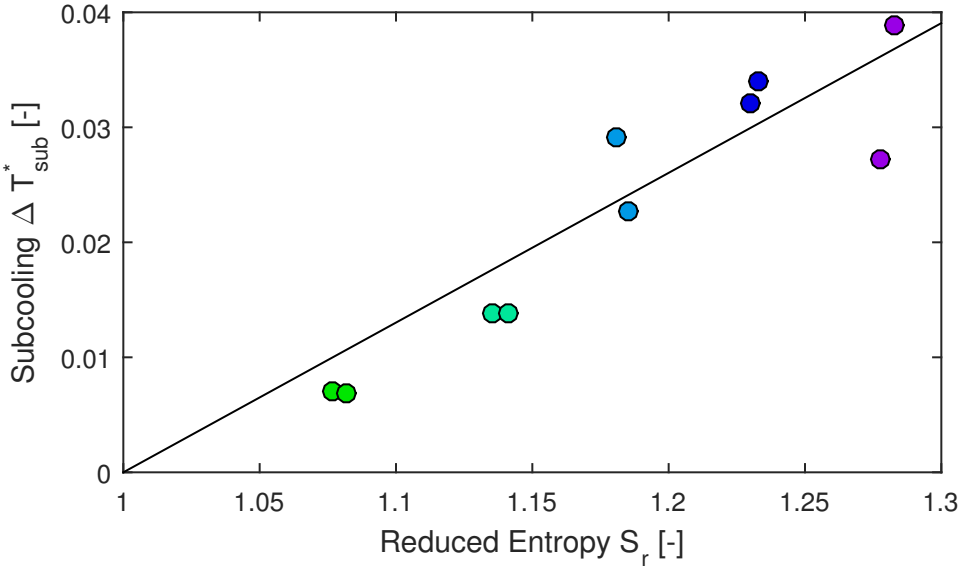

Figure 7-6: Non-dimensionalized subcooling for Set I runs 4-8(a,b) showing typical behavior of increased subcooling with increased reduced entropy

7.4 Derived Limit on Compressor Inlet Conditions

Using the experimentally derived Wilson line shown in Figure 7-7, a limit on compressor total conditions based on condensation onset was derived. Because the Wilson Line conditions are outside the theoretical metastable region defined by the SW spinodal, condensation limited total conditions could only explicitly be calculated for reduced entropies greater than approximately 1.12.

For points above this limit, the total condition limits on compressor inlet were

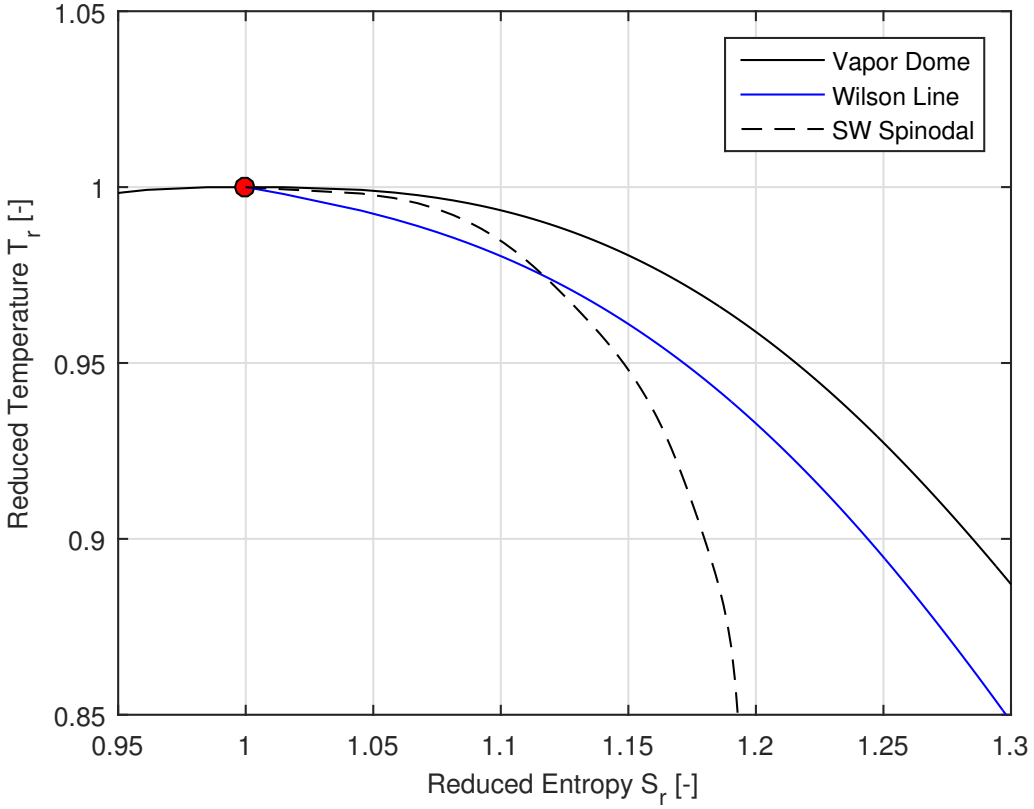

Figure 7-7: Continuous Wilson line derived from a linear fit of subcooling in runs 4-8

determined using 1-D compressible flow and an assumed maximum Mach number at the impeller. Speed of sound and enthalpy at all points along the Wilson line were calculated using extrapolated values from the SW EOS. Assuming a Mach number, a velocity was calculated. Equation 6.3 was used to calculate a total enthalpy from the velocity and static enthalpy. With the entropy and total enthalpy known, the total conditions were calculated using the equilibrium SW EOS. Condensation limits for various Mach numbers are illustrated in Figure 7-8.

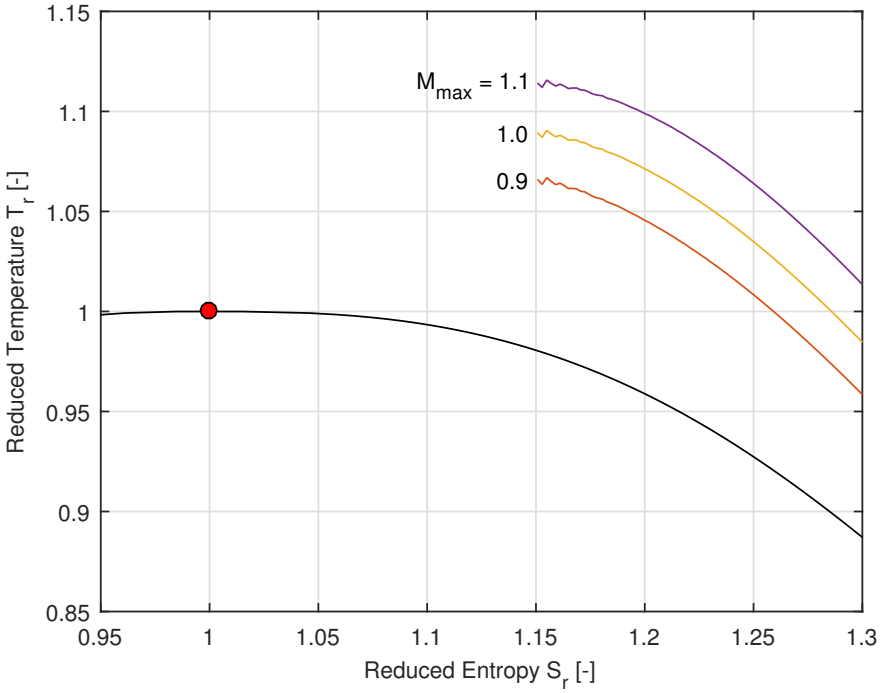

Figure 7-8: Experimentally derived condensation limits on compressor inlet conditions for various maximum Mach numbers

The condensation limit for a maximum Mach number of 1 is taken as a new, experimentally derived limit typical for transonic S-CO_2 compressors. This new boundary is compared on a T-s diagram with the computationally and empirically derived compressor safety boundaries described in Chapter 1 in Figure 7-9. Successful operation points for the compressor for which the boundaries were derived are also shown. It can be seen that the previous computationally derived safety boundary both under or over predicts the total conditions necessary to achieve condensation depending on

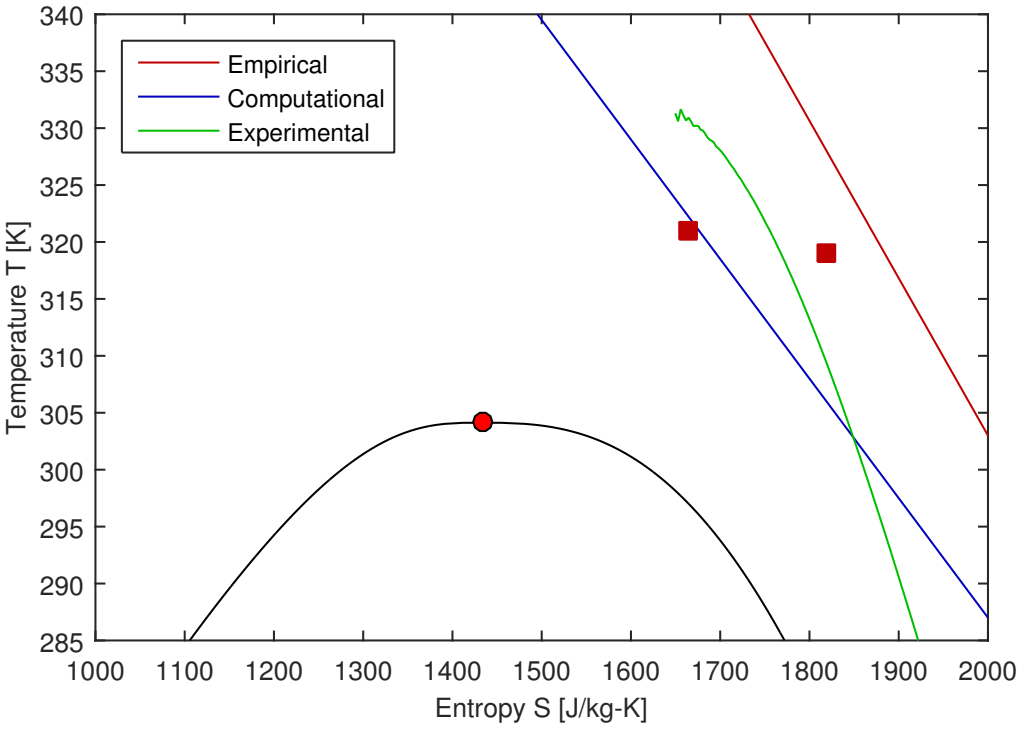

Figure 7-9

the vicinity to the vapor dome, and the empirically derived boundary over predicts the condensation limit for all points. Also of note is the fact that the compressor was operated below the experimentally derived boundary. This is most likely due to the small degree of condensation which occurs during the short residence time of the fluid in the metastable region. Future work to establish a boundary that takes this into account will is covered in Chapter 8

7.5 Boundary Layer Behavior Near the Critical Point

The interferometer was not used to measure the density in all runs of Set II Instead, traditional photographs were taken of the nozzle with front lighting and a black background. This allowed for the illumination and photography of the condensation front in the nozzle.

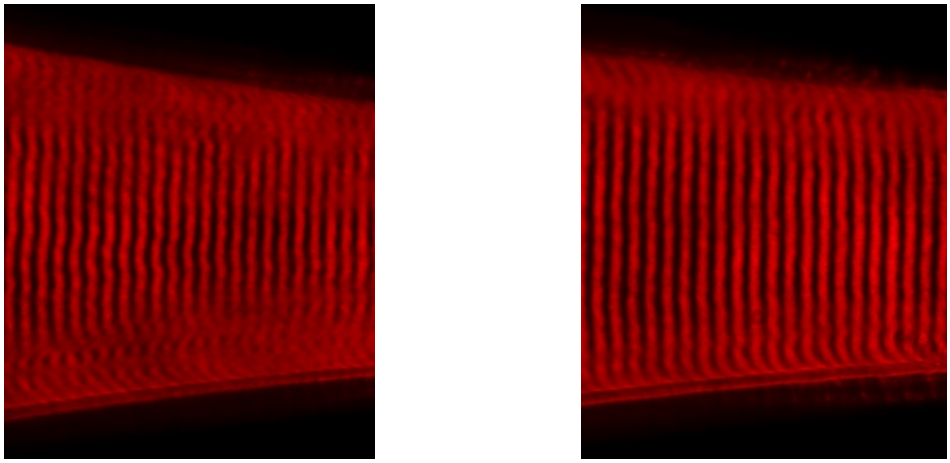

(a) Set I. run 1a (near critical) (b) Set I. run 6b (away from critical)

Figure 7-10: Comparison between the larger blurred region in the boundary layer in runs near the critical point (a) and thinner region away from the critical point (b)

7.5.1 Blurring along nozzle walls

Blurring near the edges of the images, as seen in Figure 7-10, was observed in the runs with the interferometer near the critical point. It was assumed that this was due to boundary layers along the nozzle walls. It was predicted that the boundary layers would shrink as the total conditions approached the critical point since the Reynolds number increases, however the opposite was observed. Figure 7-10 shows the comparison of the interferometric image taken during the blowdown for Set I runs 1a, and 6b showing the thicker blurred region in the former of the two. The high resolution images of the nozzle captured in Set II, were used to track the shape of the condensation front to gain insight into the boundary layer behavior

7.5.2 Cross-Channel Condensation Front Shape

A sample raw image from Set II is shown in Figure 7-11. The nozzle throat is approximately 150 pixels across in the images leading to a usable resolution even zoomed in to just the condensation front. Cropped images from set points 1-6 are compiled in a composite image in Figure 7-12. Runs 7 and 8 were not included as the condensation front was too diffuse to identify a shape.

Due to the resolution of the images is difficult to distinguish between flow non-

uniformity across the channel due to streamline curvature and that caused by boundary layer effects. Since all the condensation fronts occurred within 10% of the throat however, streamline curvature effects should be minimal. The shape of the condensation fronts for runs 2-5 are all planar to within 1% of channel height across the middle 80% of the channel with up to 8% variation near the wall. At the extremes of the operating range (runs 1a, and 6b) however, the variation in condensation location is significantly larger and not limited to the near wall region. The condensation front in run 1a shows up to a 15% variation in location while run 6b shows up to 20%. The odd behavior of apparent thickening of the boundary layers near the critical point as well as the dramatic change in height-wise variation in condensation front curvature between runs 5 and 7 should be investigated in further work.

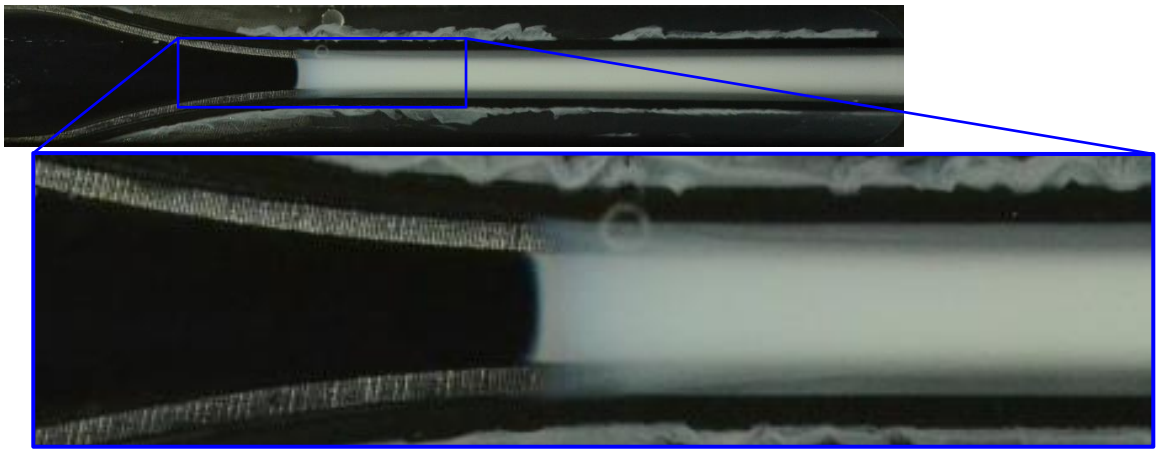

Figure 7-11: Example image of the condensation front using a traditional front-lit image as was used in Set II.

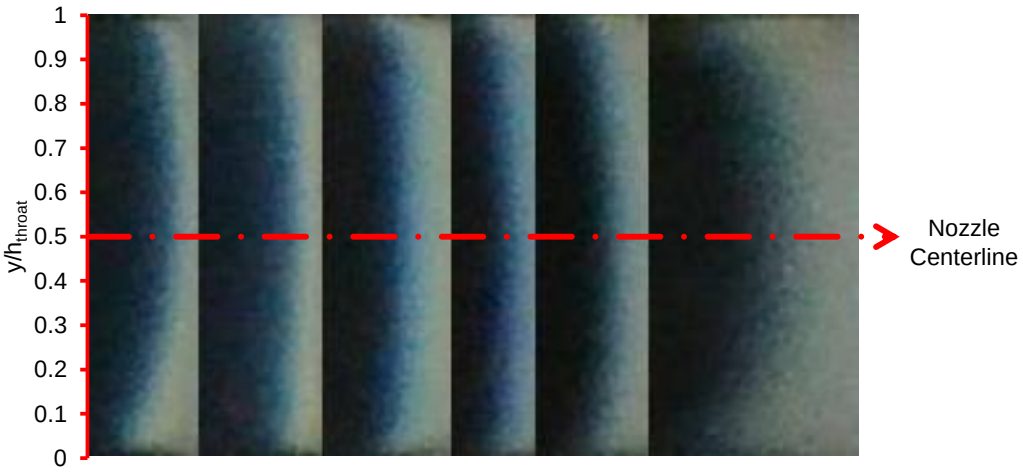

Figure 7-12: Cropped images of the condensation front for Set II runs 1-6 (runs 7 and 8 did not have a well defined condensation front)

Chapter 8

Summary & Recommendations for the Future

8.1 Thesis Contributions

This thesis focused on the experimental characterization of the behavior of supercritical CO_2 undergoing non-equilibrium condensation The design methodology of the new test rig was focused on usability and modularity, and this capability should be exploited in the future to further knowledge on non-equilibrium condensation and other supercritical CO_2 phenomena. The main contributions of the thesis can be summarized as follows:

New Experimental Capability

1. Commissioned a blowdown test facility with a nozzle test section with optical access tested to 150 bar enabling the investigation of metastable CO_2 expansion in a transonic flow near the critical point.

2. Demonstrated the use of interferometry for measuring the density of supercritical CO_2 near the critical point to within 2% allowing for the assessment of metastable extrapolation schemes.

Findings from Blowdown Testing

1. Established the accuracy of EOS based extrapolation to within 2% in the region of interest for S-CO_2 compressors enabling the full characterization of the thermodynamic state prior to condensation.

2. Made first of its kind measurements of the Wilson line for CO_2 at total conditions representative of an S-CO_2 compressor providing insight into the behavior of CO_2 undergoing non-equilibrium condensation.

3. Utilized the measured Wilson line to construct a new, experimentally derived safety boundary for compressor inlet conditions indicating the possibility of increased compressor efficiency through operation at inlet conditions below those established by a previously utilized empirical safety boundary.

8.2 Recommendations for the Future

Several proposed testing campaigns which would build on the findings outlined in this thesis are given below. Throughout testing, several shortcomings were identified with the rig operation and density measurement method. Many of these can be solved with simple modifications but were not implemented due to time constraints. These proposed solutions are included below.

8.2.1 Future work on Condensation

One of the key features of the test section that was not utilized in the work for this thesis was the ability to quickly implement changes in the nozzle geometry. Future work should utilize multiple nozzle geometries in order to investigate the result of time scales on the Wilson line. A parametric study utilizing a range of nozzle lengths and expansion and contraction rates would allow for a complete characterization of non-equilibrium condensation near the critical point.

Another aspect of the test section that was not utilized was the high pressure measurement resolution in the diverging section of the nozzle. This was due to two

reasons. First, the Mach waves discussed in Chapter 6 prevented density measurements in the supersonic flow. This can be fixed by simply making new nozzle inserts with a polished finish. Second, the condensation Mach number from representative total conditions was close to 1, leading to most condensation fronts occurring between the two pressure taps immediately adjacent to the throat. By raising the total conditions, the condensation front can be pushed towards the diverging section, where lower spatial gradients in static conditions and increased Kulite resolution will lead to easier determination of the pre-condensation properties.

Future work should also include 2 and 3-D CFD utilizing the extrapolated SW metastable properties to validate the improvements over the previously used tabular extrapolated properties. If the computational results show good agreement with the experiment, full compressor CFD modelling should also be performed.

8.2.2 Improvements to interferometry Method

Further Validation of Existing interferometer

While the interferometer performed well in the upstream section, further validation should be done to get more rigorous error bounds for both sub- and supersonic flows. One method which could be used to further validate the accuracy of the current interferometer is to measure a density profile that is more complex than that of a simple converging nozzle. By placing a restrictor downstream of the test section, the density profile could be adjusted while maintaining a constant total density. This would allow for the simultaneous measurement of negative and positive density gradients in the converging and diverging sections respectively. In addition, it would prevent the Mach waves currently present in the diverging section, allowing for accuracy determination at all points in the interferometer field of view.

Alternative Density Measurement Methods

Uncertainty in the density measurements could be accomplished by converting from a shearing interferometer to an absolute interferometer. This would remove the

integration step in the post processing procedure and also eliminate the need for a known constant of integration in converting to absolute density. Since knowledge of the upstream density is not needed, the field of view could be placed at any point along the nozzle contour. While the required resolution would limit the field of view, the interferometer could be positioned such that the region of interest was completely visible.

An alternative to the current shearing interferometer that would remove much of the uncertainty introduced by the many post-processing steps is a point density measurement rather than the field density measurement currently in use. This is commonly used in an isolated, static laboratory environment [25], but could most likely be adapted measuring density in a high speed flow. There are not currently any off the shelf sensors for point density measurement, but it may be possible to use off the shelf optical distance measurement devices to measure the average density at a single point in the nozzle. See [2] for more information on such a device.

Point density measurement could either be used in conjunction with shearing interferometry, BOS, or another gradient based density measurement method to provide an experimentally measured constant of integration (upstream density) to replace the currently pressure-derived value. Alternatively, multiple point absolute density sensors could be positioned along the nozzle to yield data with which the pressure contours could be compared.

8.2.3 General Rig Improvements

One of the most difficult challenges with the rig was the determination of the nozzle total conditions. The previous generation rig did not suffer from this issue as the Mach numbers and associated losses were low enough to be considered negligible allowing for the use of statically measured tank total conditions in nozzle calculations. The large pressure drops seen in the second generation rig could easily be decreased by an order of magnitude with a modest increase in diameter and decrease in length of all upstream components (bellmouth, valve, connecting pipe, and union). Currently all fittings are 1/2" and upgrading all components to 3/4" or 1" could decrease the

pressure drop significantly. Further analysis should be done to see if a negligible upstream pressure drop could be achieved with reasonably sized components.

Another key challenge was determining the tank total conditions. One way the accuracy with which the conditions could be improved is by increase the accuracy of the density and temperature measurement methods. The pressure transducers have a quoted maximum error 0.08% error and more accurate options are not readily available. The temperature accuracy could be improved by utilizing a thermistor to replace the current internal thermocouple. Thermistors can be sourced with much higher off the shelf accuracies than thermocouples.

Uncertainty in the measured tank mass using the current method results from the fact that the mass of CO_2 represents a relatively small percentage of the total tank and frame mass (typically 5-20%). Tank mass is measured with a load cell, which, as is the norm, has an accuracy quoted as a percentage of full scale output (0.07%). In the current configuration, the load cell is one of three points of contact and supports roughly half the load of the tank. With a 1200 kg load cell being used to measure 50-200 kg of CO_2 the sensor uncertainty introduces errors of up to 5%. by installing a large spring to support the mass of the empty tank, a smaller, and more accurate load cell could be used. Assuming the support spring is much less stiff than the load cell, the load cell can be sized for only the additional mass of the CO_2 decreasing total error by up to an order of magnitude. Figure 8-1 below illustrates the current configuration and the proposed change.

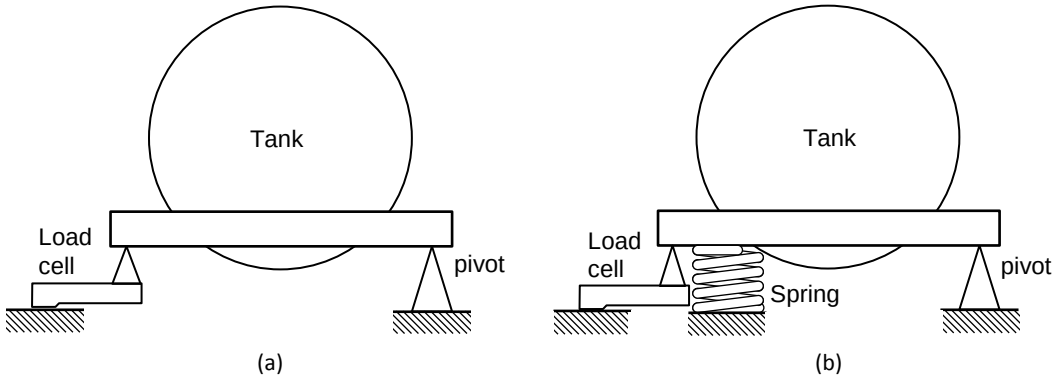

Figure 8-1: Current tank mounting method (a) and proposed modification to improve accuracy (b)

Bibliography

[1] High pressure viewport case study. http://mpfpi.com/project-examples/high-pressure-viewport.aspx.

[2] Micro-head spectral-interference laser displacement meter. http://www.keyence.com/products/measure/spectral/si-f/index.jsp.

[3] Office of fossil energy: Enhanced oil recovery. http://energy.gov/fe/science-innovation/oil-gas-research/enhanced-oil-recovery.

[4] Corning hpfs 7979, 7980, 8655 fused silica:. Optical Materials Product information Specialty Materials Division, 2014.

[5] Miniature ruggedized pressure transducer: Xt190 (m) series. http://www.kulite.com/docs/products/XT-190.pdf, 2014.

[6] G. Angelino. Real gas effects in carbon dioxide cycles. In *ASME 1969 Gas Turbine Conference and Products Show*, pages V001T01A071–V001T01A071. American Society of Mechanical Engineers, 1969.

[7] N. D. Baltadjiev, C. Lettieri, and Z. S. Spakovszky. An investigation of real gas effects in supercritical co2 centrifugal compressors. *Journal of Turbomachinery*, 137(9):091003, 2015.

[8] N. D. Baltadjiev. An investigation of real gas effects in supercritical coâĆĆ compressors. Master's thesis, Massachusetts Institute of Technology, 2012.

[9] G. Bansal, W. Duckworth, and D. Niesz. Strength analysis of brittle materials. Technical report, DTIC Document, 1977.

[10] G. J. Besserer and D. B. Robinson. Refractive indexes of ethane, carbon dioxide, and isobutane. *Journal of Chemical and Engineering Data*, 18(2):137–140, 1973.

[11] M. Born and E. Wolf. *Principles of optics: electromagnetic theory of propagation, interference and diffraction of light*. CUP Archive, 2000.

[12] A. Boutier. *Laser velocimetry in fluid mechanics*. John Wiley & Sons, 2013.

[13] Y. A. Çengel, M. A. Boles, and M. Kanoğlu. *Thermodynamics: an engineering approach*. McGraw-Hill Education, 2015.

[14] N. E. Dowling. *Mechanical behavior of materials: engineering methods for deformation, fracture, and fatigue*. Prentice hall, 1993.

[15] K. M. Duff. Condensation of carbon dioxide in supersonic nozzles. Master's thesis, Massachusetts Institute of Technology, 1964.

[16] G. Elsinga, B. Van Oudheusden, F. Scarano, and D. Watt. Assessment and application of quantitative schlieren methods: Calibrated color schlieren and background oriented schlieren. *Experiments in Fluids*, 36(2):309–325, 2004.

[17] R. Franklin and J. M. Wallace. Absolute measurements of static-hole error using flush transducers. *Journal of Fluid Mechanics*, 42(01):33–48, 1970.

[18] H. Furukawa, Y. Kato, Y. Inoue, T. Kato, Y. Tada, and S. Hashimoto. Correlation of power consumption for several kinds of mixing impellers. *International Journal of Chemical Engineering*, 2012, 2012.

[19] V. N. Gorbunov. *Nonequilibrium condensation in high-speed gas flows*. CRC Press, 1989.

[20] E. M. Greitzer, C. S. Tan, and M. B. Graf. *Internal flow: concepts and applications*, volume 3. Cambridge University Press, 2007.

[21] A. Guha. Thermal choking due to nonequilibrium condensation. *Journal of fluids engineering*, 116(3):599–604, 1994.

[22] S. Harvey. United states energy information administration frequently asked questions. http://www.eia.gov/tools/faqs/faq.cfm?id=77t=11, 2016.

[23] P. Hill, K. Miyagawa, and J. Denton. Fast and accurate inclusion of steam properties in two-and three-dimensional steam turbine flow calculations. *Proceedings of the Institution of Mechanical Engineers, Part C: Journal of Mechanical Engineering Science*, 214(7):903–919, 2000.

[24] T. R. Judge and P. Bryanston-Cross. A review of phase unwrapping techniques in fringe analysis. *Optics and Lasers in Engineering*, 21(4):199–239, 1994.

[25] V. Kulesh. Measurement of gas density by heterodyne interferometry. *Measurement techniques*, 39(2):162–167, 1996.

[26] G. Lamanna, J. Van Poppel, and M. van Dongen. Experimental determination of droplet size and density field in condensing flows. *Experiments in fluids*, 32(3):381–395, 2002.

[27] B. I. Lee and M. G. Kesler. A generalized thermodynamic correlation based on three-parameter corresponding states. *AIChE Journal*, 21(3):510–527, 1975.

[28] E. Lemmon, M. Huber, and M. Mclinden. Nist standard reference database 23: Reference fluid thermodynamic and transport properties-refprop, version 9.1. National Institute of Standards and Technology, 2013.

[29] C. Lettieri, D. Yang, and Z. Spakovszky. An investigation of condensation effects in supercritical carbon dioxide compressors. *Journal of Engineering for Gas Turbines and Power*, 137(8):082602, 2015.

[30] K. H. Lüdtke. *Process centrifugal compressors: basics, function, operation, design, application*. Springer Science & Business Media, 2013.

[31] C. Lujie. Cross-platform image-processing program âĂŞ uu. Singapore Inst. of Tech. Design, 2014.

[32] C. R. Mercer and G. Raman. Quantitative interferometry in the severe acoustic environment of resonant supersonic jets. *AIAA journal*, 40(3):438–442, 2002.

[33] W. Merzkirch. *Flow visualization*. Elsevier, 2012.

[34] A. Michels and J. Hamers. The effect of pressure on the refractive index of co 2: The lorentz-lorenz formula. *Physica*, 4(10):995–1006, 1937.

[35] L. F. Moody. Friction factors for pipe flow. *Trans. Asme*, 66(8):671–684, 1944.

[36] R. Parsons. *The Early Days of the Power Station Industry*. Cambridge University Press, 1940.

[37] E. L. Paul, V. A. Atiemo-Obeng, and S. M. Kresta. *Handbook of industrial mixing: science and practice*. John Wiley & Sons, 2004.

[38] B. Pelliccia-Kraft and D. Watt. Three-dimensional imaging of a turbulent jet using shearing interferometry and optical tomography. *Experiments in fluids*, 29(6):573–581, 2000.

[39] B. Proctor, I. Whitney, and J. Johnson. The strength of fused silica. In *Proceedings of the Royal Society of London A: Mathematical, Physical and Engineering Sciences*, volume 297, pages 534–557. The Royal Society, 1967.

[40] M. Raffel, C. E. Willert, J. Kompenhans, et al. *Particle image velocimetry: a practical guide*. Springer, 2013.

[41] E. Rinaldi, R. Pecnik, and P. Colonna. Steady state cfd investigation of a radial compressor operating with supercritical co2. In *ASME Turbo Expo 2013: Turbine Technical Conference and Exposition*, pages V008T34A008–V008T34A008. American Society of Mechanical Engineers, 2013.

[42] I. Secretariat, B. Dooley, and P. A. C. EPRI. Revised release on the iapws formulation 1985 for the thermal conductivity of ordinary water substance. 1997.

[43] S. N. Sen. *Acoustics, waves and oscillations*. New Age International, 1990.

[44] G. Settles. *Schlieren and Shadowgraph Techniques*. Springer, 2001.

[45] C. Söller, R. Wenskus, P. Middendorf, G. Meier, and F. Obermeier. Interferometric tomography for flow visualization of density fields in supersonic jets and convective flow. *Applied optics*, 33(14):2921–2932, 1994.

[46] R. Span. *Multiparameter Equations of State: An Accurate Source of Thermodynamic Property Data*. Springer, 2010.

[47] R. Span and W. Wagner. A new equation of state for carbon dioxide covering the fluid region from the triple-point temperature to 1100 k at pressures up to 800 mpa. *Journal of physical and chemical reference data*, 25(6):1509–1596, 1996.

[48] F. White. *Fluid Mechanics*. McGraw-Hill Education, 2010.

[49] C. T. R. Wilson. Condensation of water vapour in the presence of dust-free air and other gases. *Proceedings of the Royal Society of London*, 61(369-377):240–242, 1897.

[50] D. Yang. Experimental assessment of the internal flow behavior of supercritical carbon dioxide. Master's thesis, Massachusetts Institute of Technology, 2014.

[51] J. Young. Two-dimensional, nonequilibrium, wet-steam calculations for nozzles and turbine cascades. *Journal of Turbomachinery*, 114(3):569–579, 1992.

Appendix A

Technical Drawings

SECTION A-A

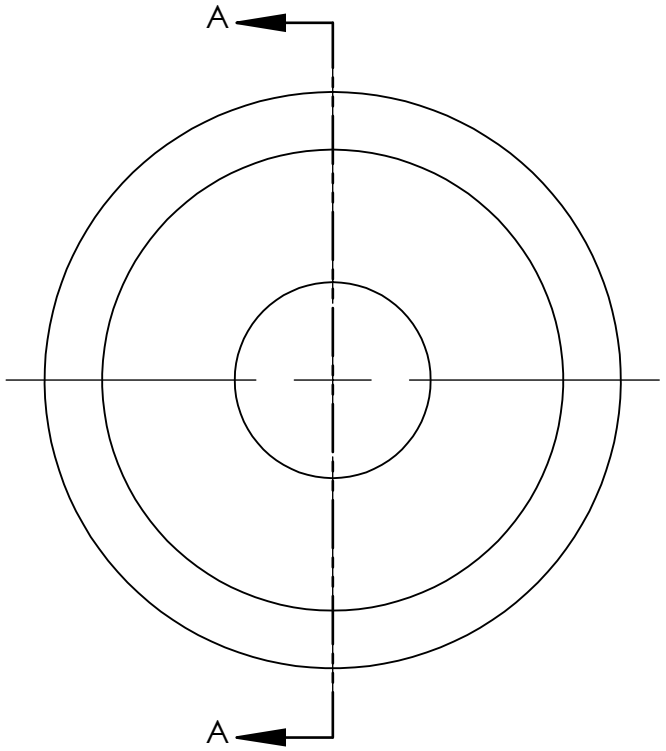

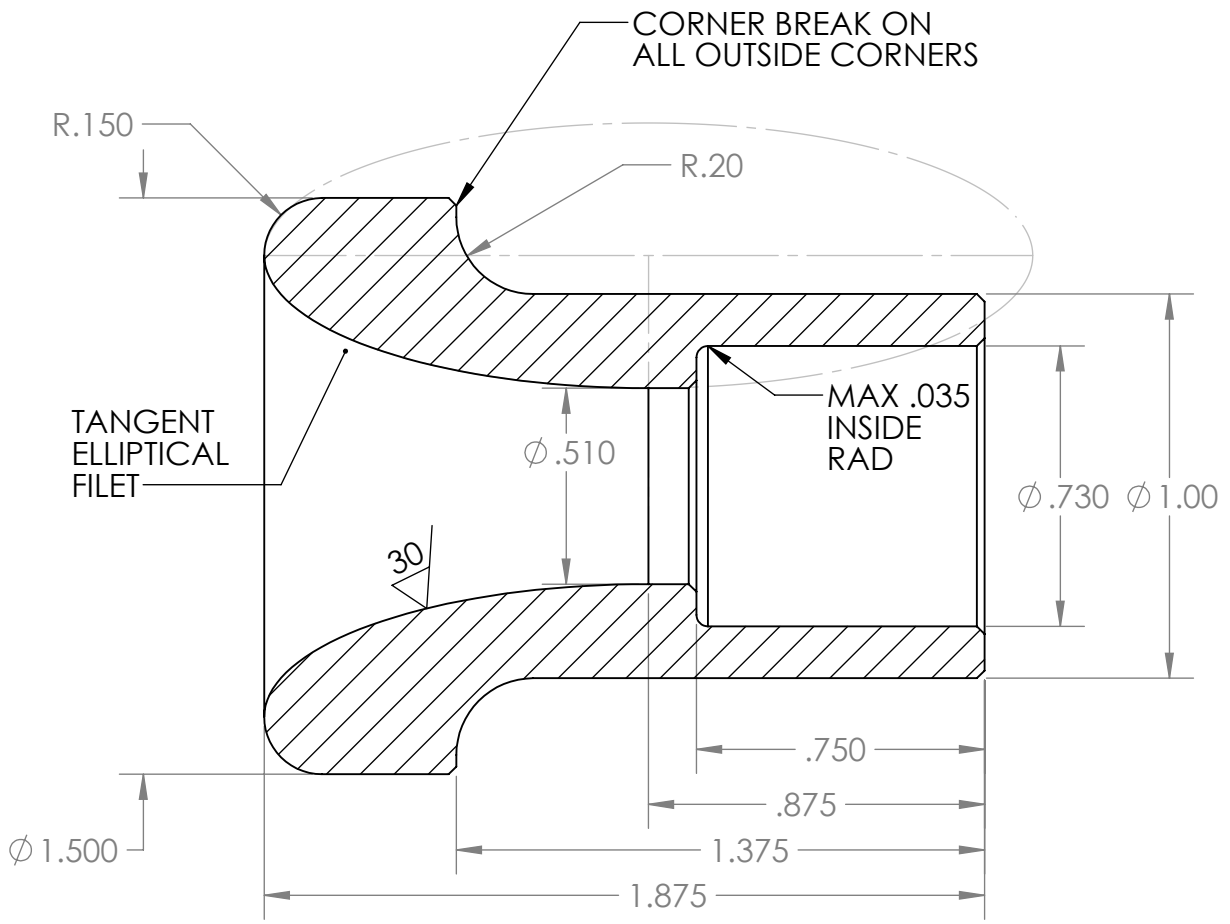

		UNLESS OTHERWISE SPECIFIED:		NAME	DATE
		DIMENSIONS ARE IN INCHES TOLERANCES: FRACTIONAL ± ANGULAR: MACH ± BEND ± TWO PLACE DECIMAL ± THREE PLACE DECIMAL ±	DRAWN	D.PAXSON	3-16-15
			CHECKED		
			ENG APPR.		
			MFG APPR.		
		INTERPRET GEOMETRIC TOLERANCING PER:	Q.A.		
		MATERIAL 304 STAINLESS	COMMENTS: 303 STAINLESS CAN BE SUBSTITUTED FOR MACHINABILITY		
NEXT ASSY	USED ON	FINISH			
APPLICATION		DO NOT SCALE DRAWING			

TITLE:

BELLMOUTH

SIZE	DWG. NO.	REV
A	003	
SCALE: 2:1	WEIGHT:	SHEET 1 OF 1

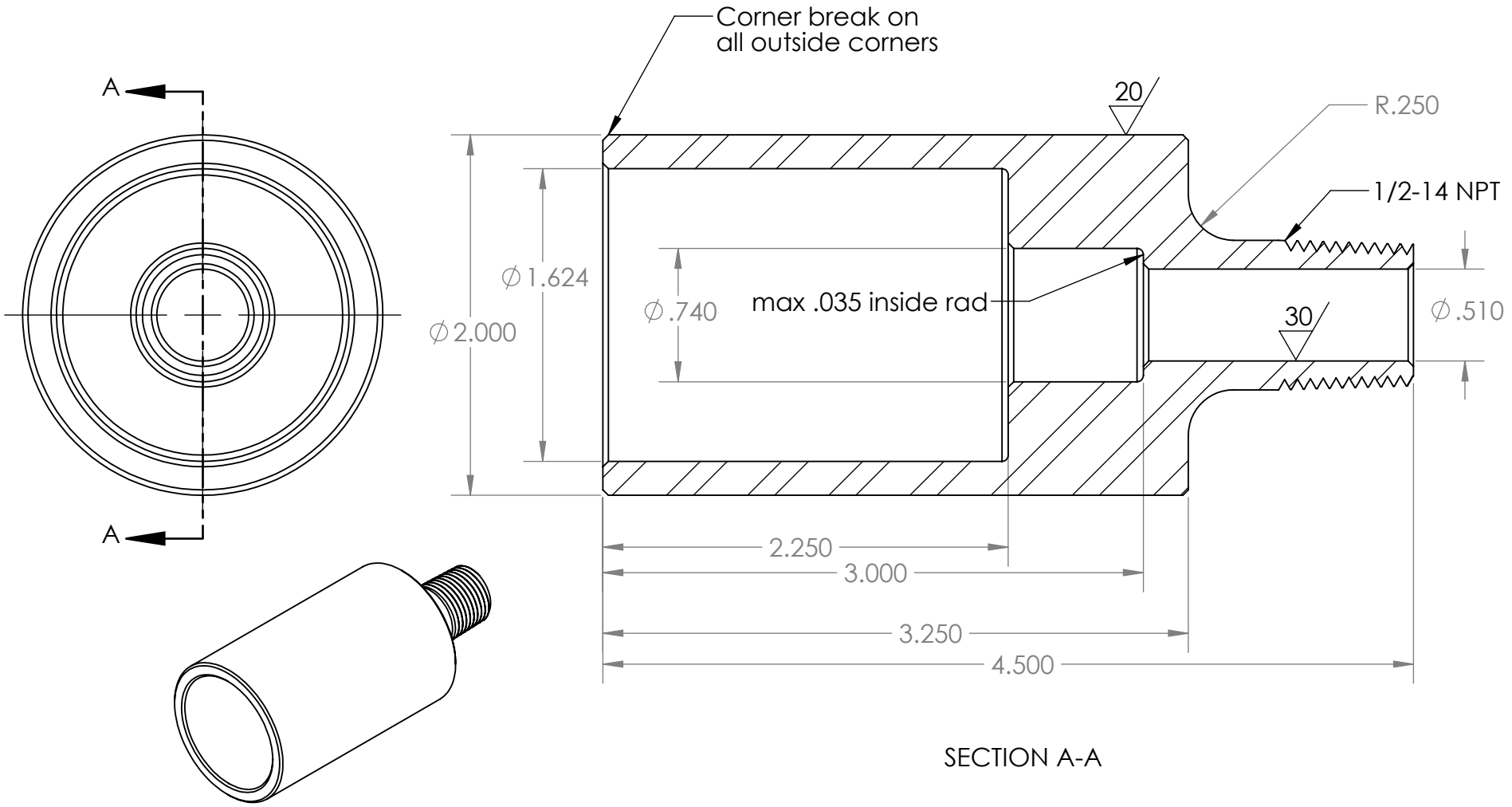

SECTION A-A

		UNLESS OTHERWISE SPECIFIED:		NAME	DATE
		DIMENSIONS ARE IN INCHES TOLERANCES: FRACTIONAL ± ANGULAR: MACH ± BEND ± TWO PLACE DECIMAL ± THREE PLACE DECIMAL ±	DRAWN	D.PAXSON	3-16-15
			CHECKED		
			ENG APPR.		
			MFG APPR.		
		INTERPRET GEOMETRIC TOLERANCING PER:	Q.A.		
		MATERIAL 304 Stainless	COMMENTS: 303 STAINLESS CAN BE SUBSTITUTED FOR MACHINABILITY		
NEXT ASSY	USED ON	FINISH			
APPLICATION		DO NOT SCALE DRAWING			

TITLE:

SWAGELOK ADAPTER

SIZE	DWG. NO.	REV
A	001	

SCALE: 1:0.85 | SHEET 1 OF 1

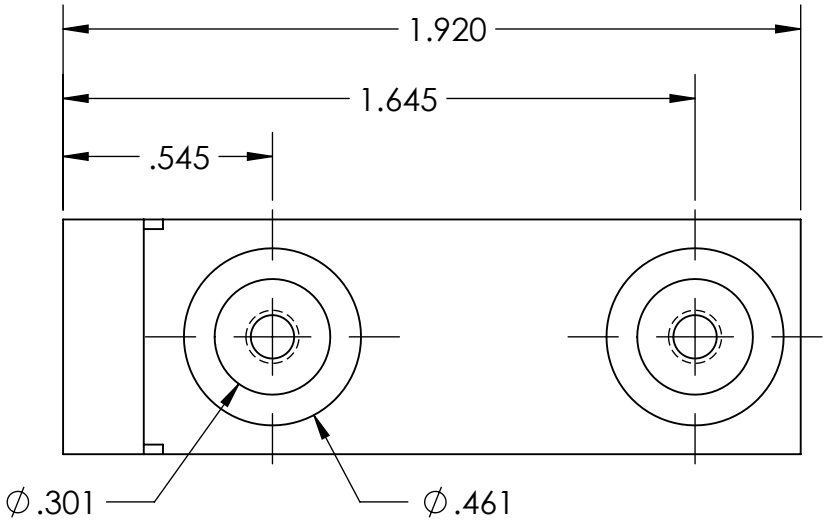

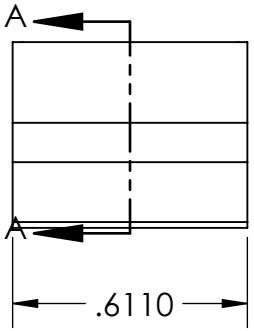

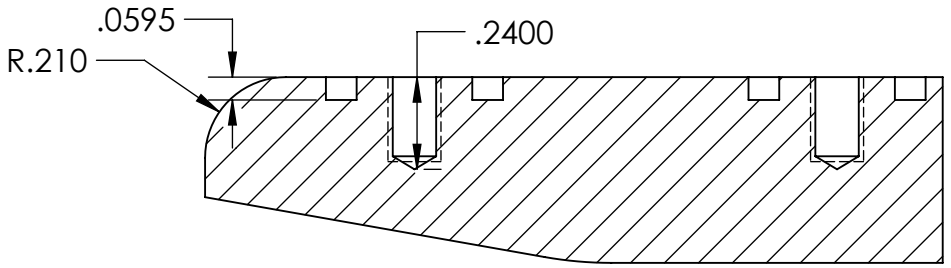

SECTION A-A

		UNLESS OTHERWISE SPECIFIED:		NAME	DATE
		DIMENSIONS ARE IN INCHES TOLERANCES: FRACTIONAL ± ANGULAR: MACH ± BEND ± TWO PLACE DECIMAL ± THREE PLACE DECIMAL ±	DRAWN		
			CHECKED		
			ENG APPR.		
			MFG APPR.		
		INTERPRET GEOMETRIC TOLERANCING PER:	Q.A.		
		MATERIAL	COMMENTS:		
NEXT ASSY	USED ON	FINISH			
APPLICATION		DO NOT SCALE DRAWING			

TITLE:

SIZE	DWG. NO.	REV
A	dummy_block_back	

SCALE: 2:1 | WEIGHT: | SHEET 1 OF 2

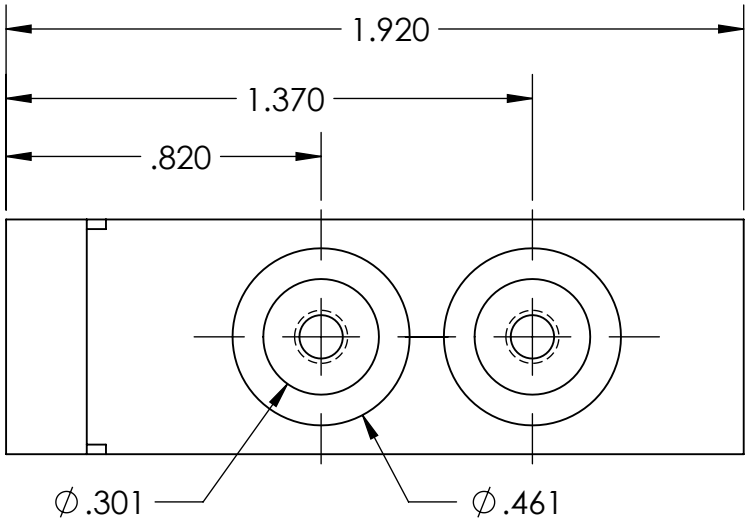

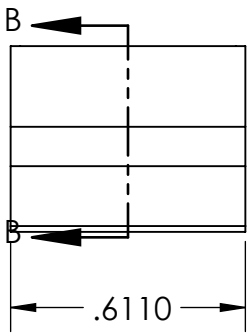

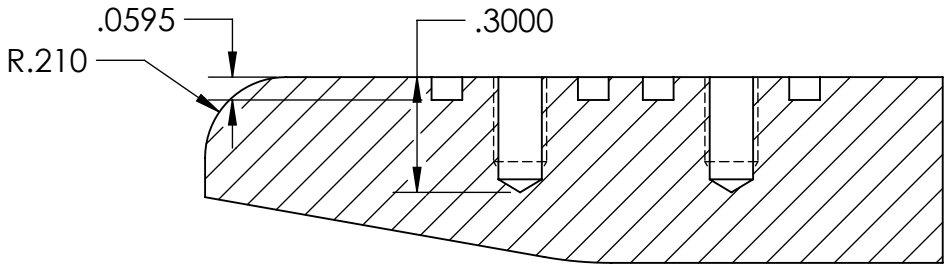

SECTION B-B

		UNLESS OTHERWISE SPECIFIED:		NAME	DATE
		DIMENSIONS ARE IN INCHES TOLERANCES: FRACTIONAL ± ANGULAR: MACH ± BEND ± TWO PLACE DECIMAL ± THREE PLACE DECIMAL ±	DRAWN		
			CHECKED		
			ENG APPR.		
			MFG APPR.		
		INTERPRET GEOMETRIC TOLERANCING PER:	Q.A.		
		MATERIAL	COMMENTS:		
NEXT ASSY	USED ON	FINISH			
APPLICATION		DO NOT SCALE DRAWING			

TITLE:

SIZE	DWG. NO.	REV
A	dummy_block_back	

SCALE: 2:1 | WEIGHT: | SHEET 2 OF 2

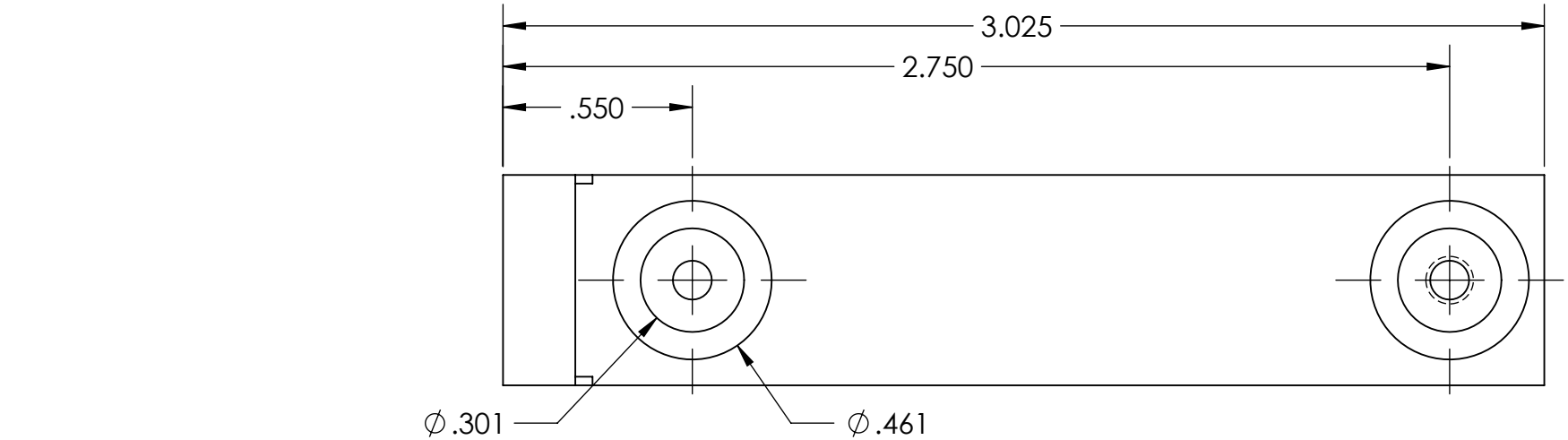

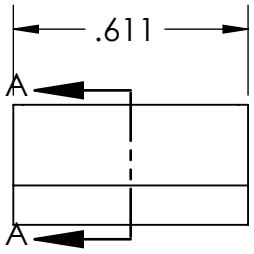

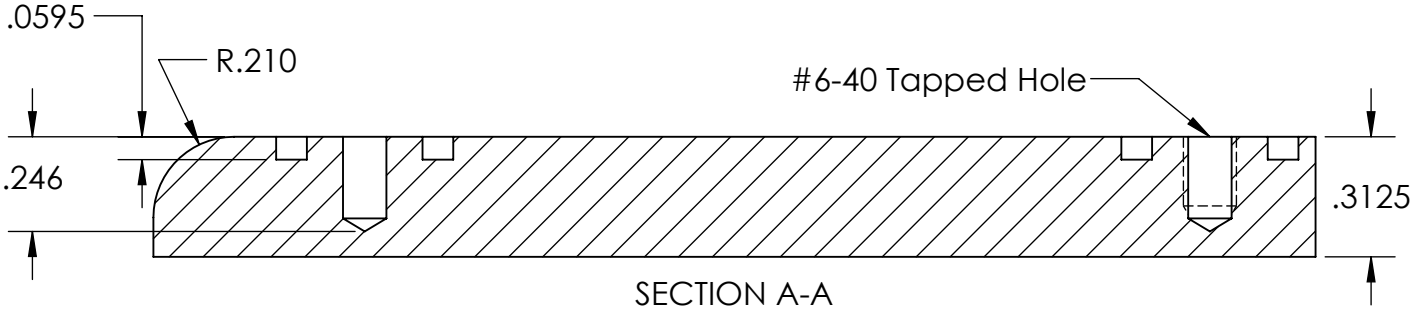

SECTION A-A

		UNLESS OTHERWISE SPECIFIED:		NAME	DATE
		DIMENSIONS ARE IN INCHES TOLERANCES: FRACTIONAL ± ANGULAR: MACH ± BEND ± TWO PLACE DECIMAL ± THREE PLACE DECIMAL ±	DRAWN		
			CHECKED		
			ENG APPR.		
			MFG APPR.		
		INTERPRET GEOMETRIC TOLERANCING PER:	Q.A.		
		MATERIAL	COMMENTS:		
NEXT ASSY	USED ON	FINISH			
APPLICATION		DO NOT SCALE DRAWING			

TITLE:

SIZE	DWG. NO.	REV
A	dummy_block_front	

SCALE: 2:1 | WEIGHT: | SHEET 1 OF 2

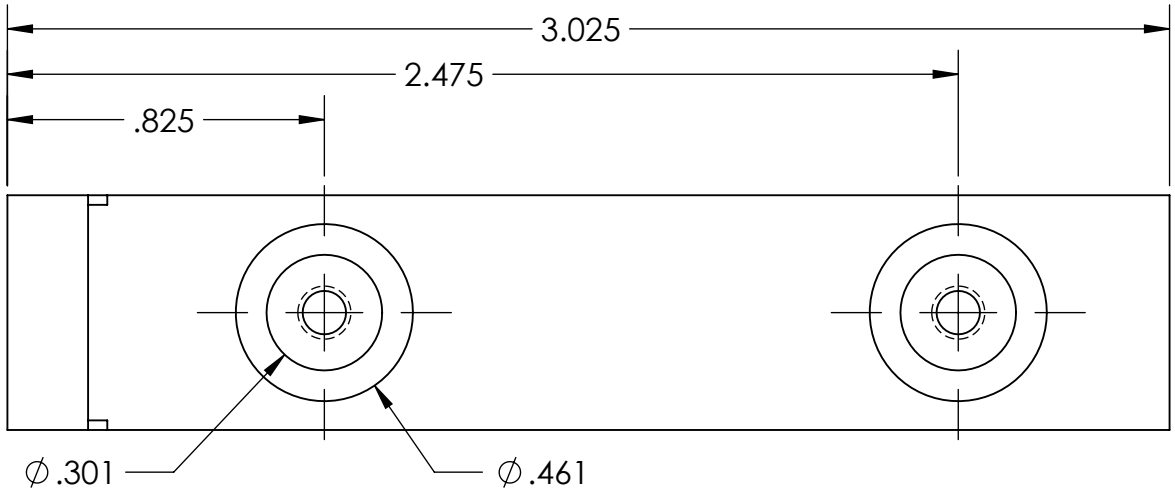

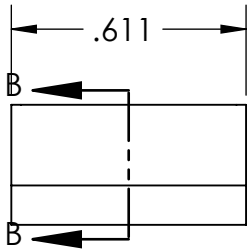

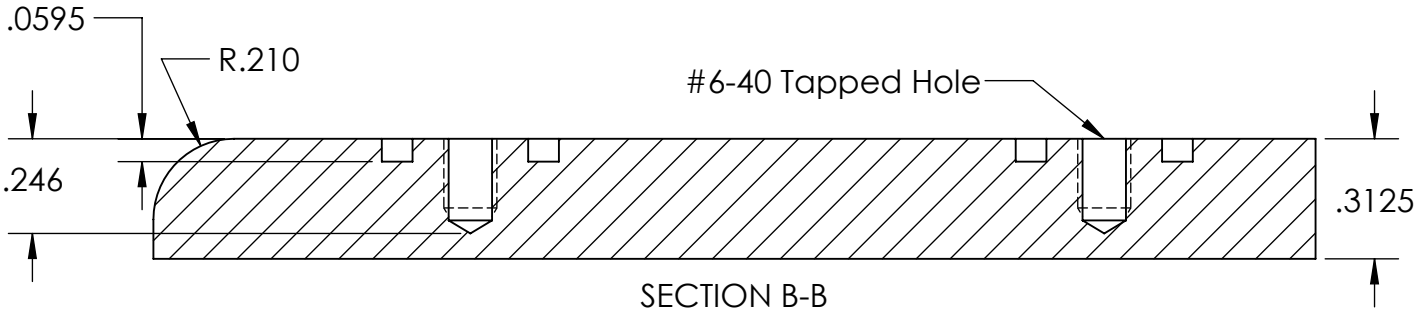

SECTION B-B

		UNLESS OTHERWISE SPECIFIED:		NAME	DATE
		DIMENSIONS ARE IN INCHES TOLERANCES: FRACTIONAL ± ANGULAR: MACH ± BEND ± TWO PLACE DECIMAL ± THREE PLACE DECIMAL ±	DRAWN		
			CHECKED		
			ENG APPR.		
			MFG APPR.		
		INTERPRET GEOMETRIC TOLERANCING PER:	Q.A.		
		MATERIAL	COMMENTS:		
NEXT ASSY	USED ON	FINISH			
APPLICATION		DO NOT SCALE DRAWING			

TITLE:

SIZE	DWG. NO.	REV
A	dummy_block_front	
SCALE: 2:1	WEIGHT:	SHEET 2 OF 2

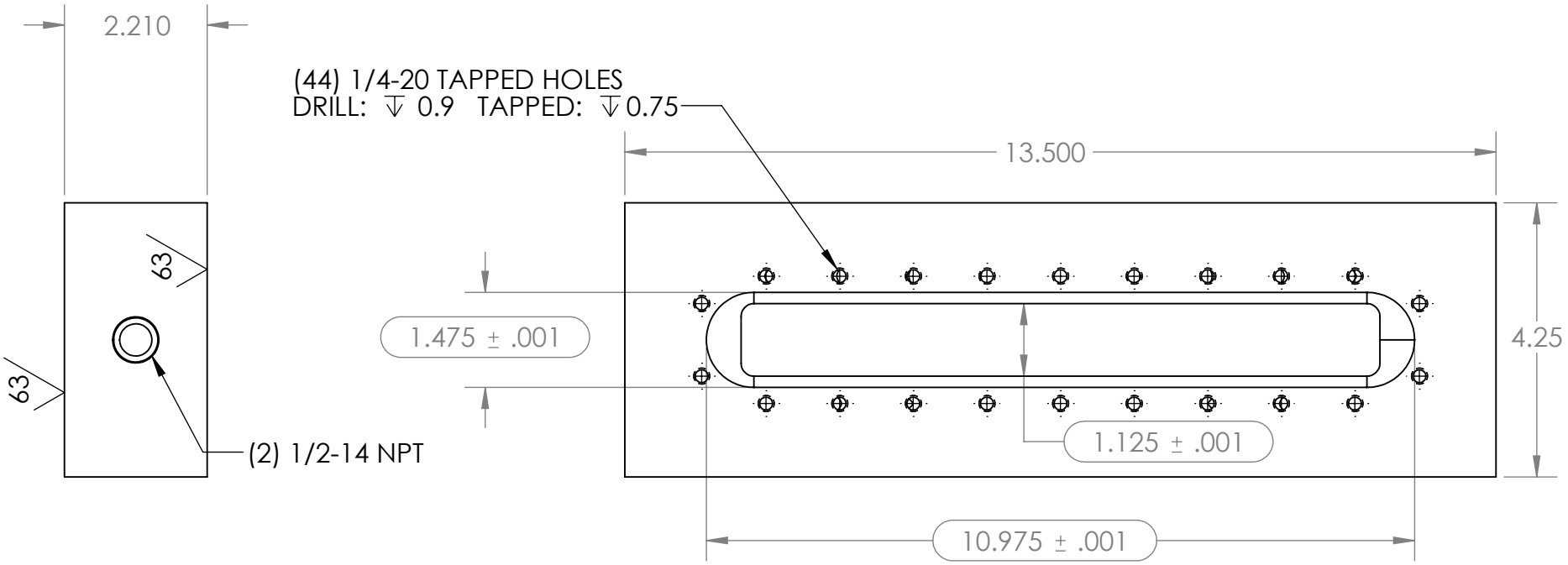

UNLESS OTHERWISE SPECIFIED:		NAME	DATE
DIMENSIONS ARE IN INCHES TOLERANCES: TWO PLACE DECIMAL ± .005 FROM CAD MODEL ± .005	DRAWN	D. PAXSON	5/11/15
	CHECKED		
	ENG APPR.		
	MFG APPR.		
INTERPRET GEOMETRIC TOLERANCING PER:	Q.A.		
MATERIAL 17-4 STAINLESS	COMMENTS: 17-4 STAINLESS CAN BE IN ANNEALED OR H900 STATE BASED ON MACHINING PREFERENCE		
FINISH			
DO NOT SCALE DRAWING			

TITLE:

TEST SECTION BODY

SIZE	DWG. NO.	REV
A	002	
SCALE: 1:2.5	WEIGHT:	SHEET 1 OF 2

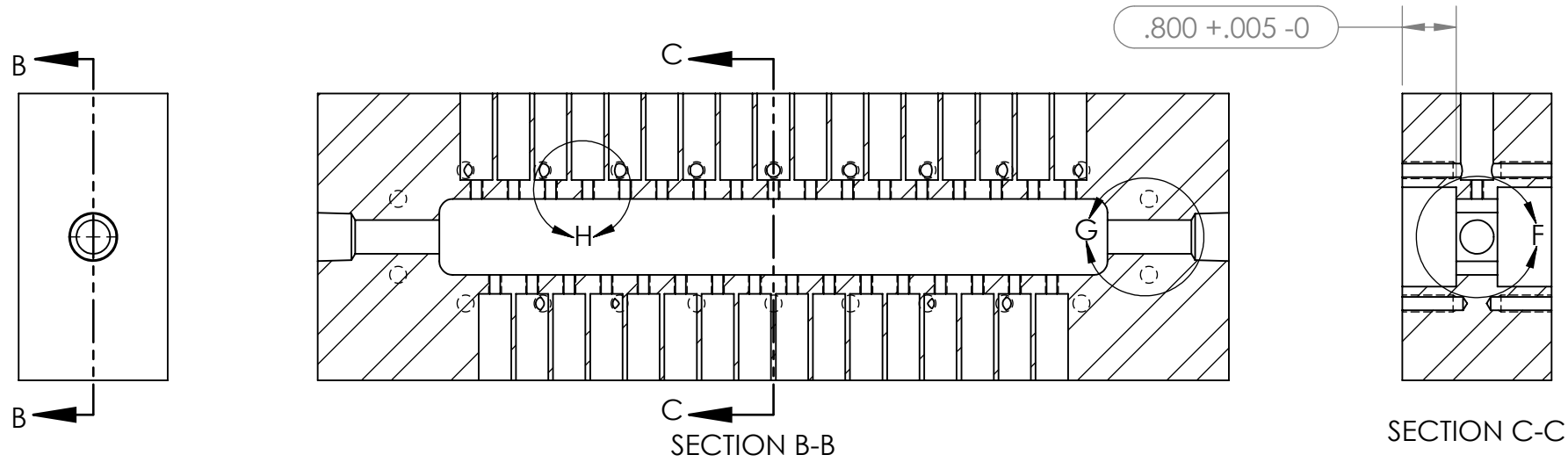

SECTION B-B

SECTION C-C

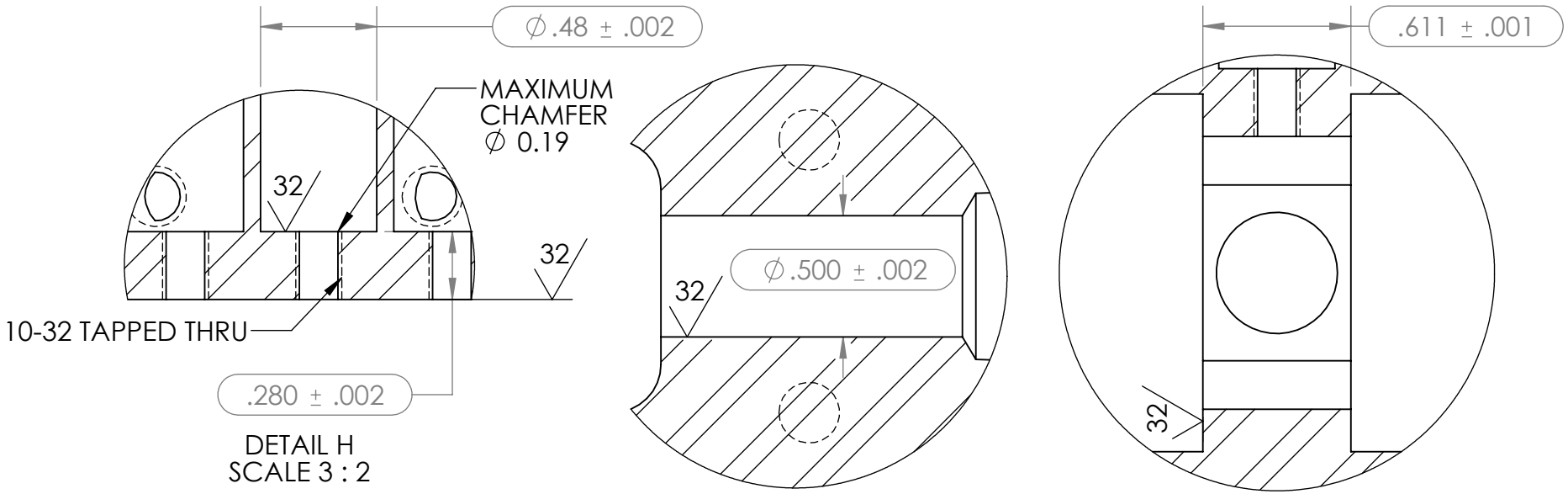

DETAIL H
SCALE 3 : 2

DETAIL G
SCALE 3 : 2

DETAIL F
SCALE 3 : 2

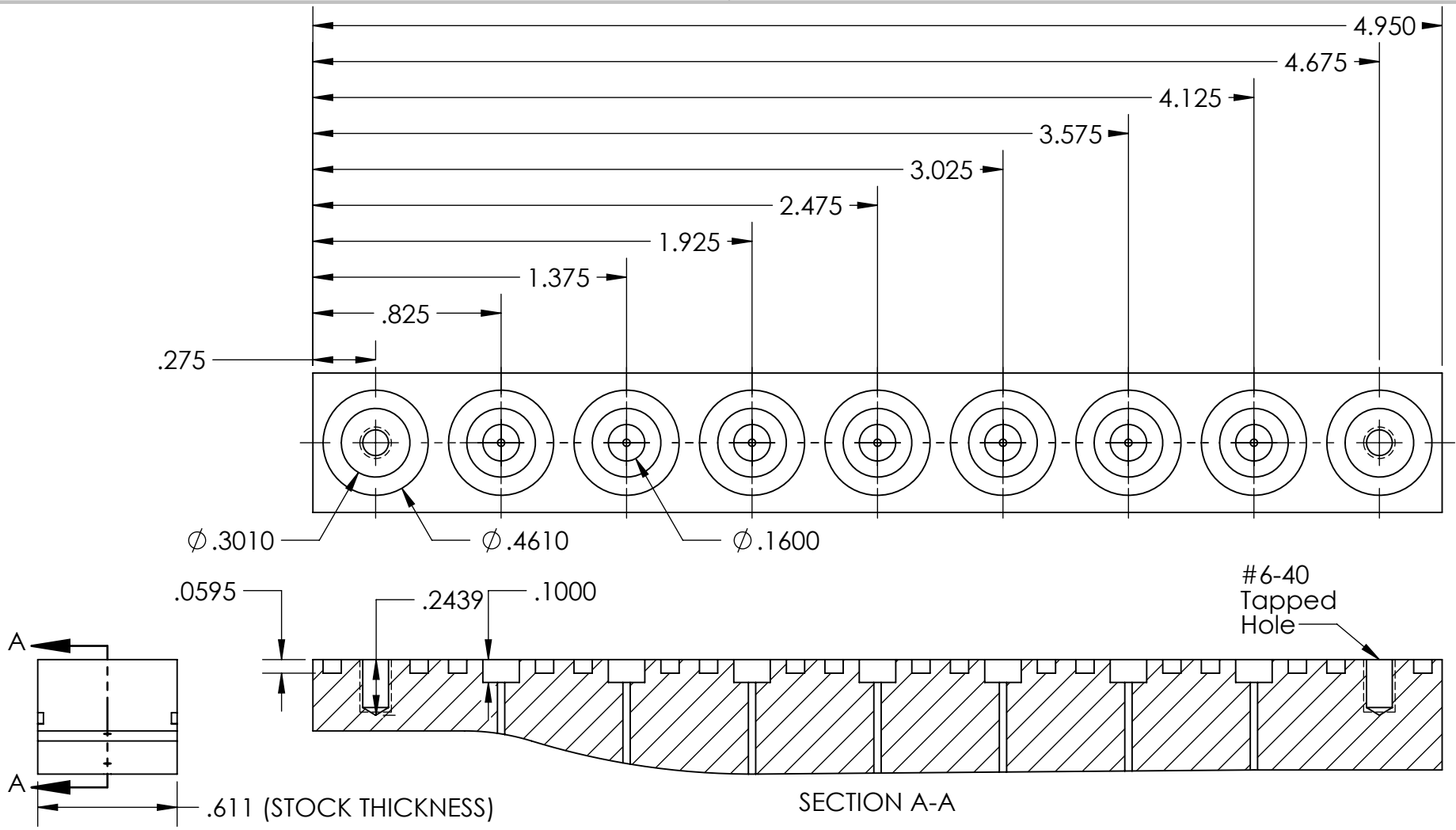

		UNLESS OTHERWISE SPECIFIED:		NAME	DATE
		DIMENSIONS ARE IN INCHES TOLERANCES: FRACTIONAL ± ANGULAR: MACH ± BEND ± TWO PLACE DECIMAL ± THREE PLACE DECIMAL ±	DRAWN		
			CHECKED		
			ENG APPR.		
			MFG APPR.		
		INTERPRET GEOMETRIC TOLERANCING PER:	Q.A.		
		MATERIAL	COMMENTS:		
NEXT ASSY	USED ON	FINISH			
APPLICATION		DO NOT SCALE DRAWING			

TITLE:

SIZE	DWG. NO.	REV
A	con_di_insert_007	
SCALE: 3:2	WEIGHT:	SHEET 1 OF 2

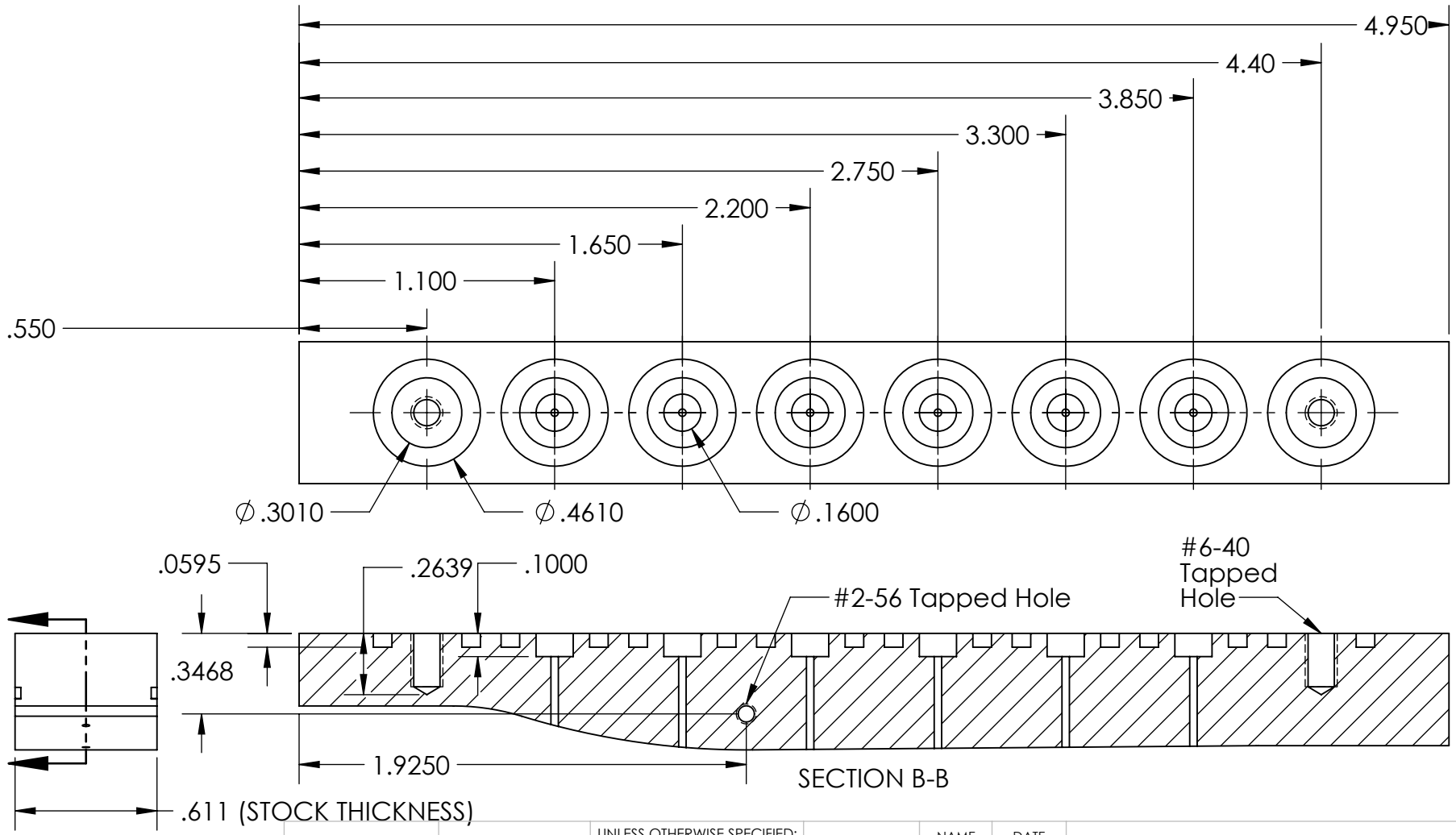

		UNLESS OTHERWISE SPECIFIED:		NAME	DATE
		DIMENSIONS ARE IN INCHES TOLERANCES: FRACTIONAL ± ANGULAR: MACH ± BEND ± TWO PLACE DECIMAL ± THREE PLACE DECIMAL ±	DRAWN		
			CHECKED		
			ENG APPR.		
			MFG APPR.		
		INTERPRET GEOMETRIC TOLERANCING PER:	Q.A.		
		MATERIAL	COMMENTS:		
NEXT ASSY	USED ON	FINISH			
APPLICATION		DO NOT SCALE DRAWING			

TITLE:

SIZE	DWG. NO.	REV
A	con_di_insert_007	
SCALE: 3:2	WEIGHT:	SHEET 2 OF 2

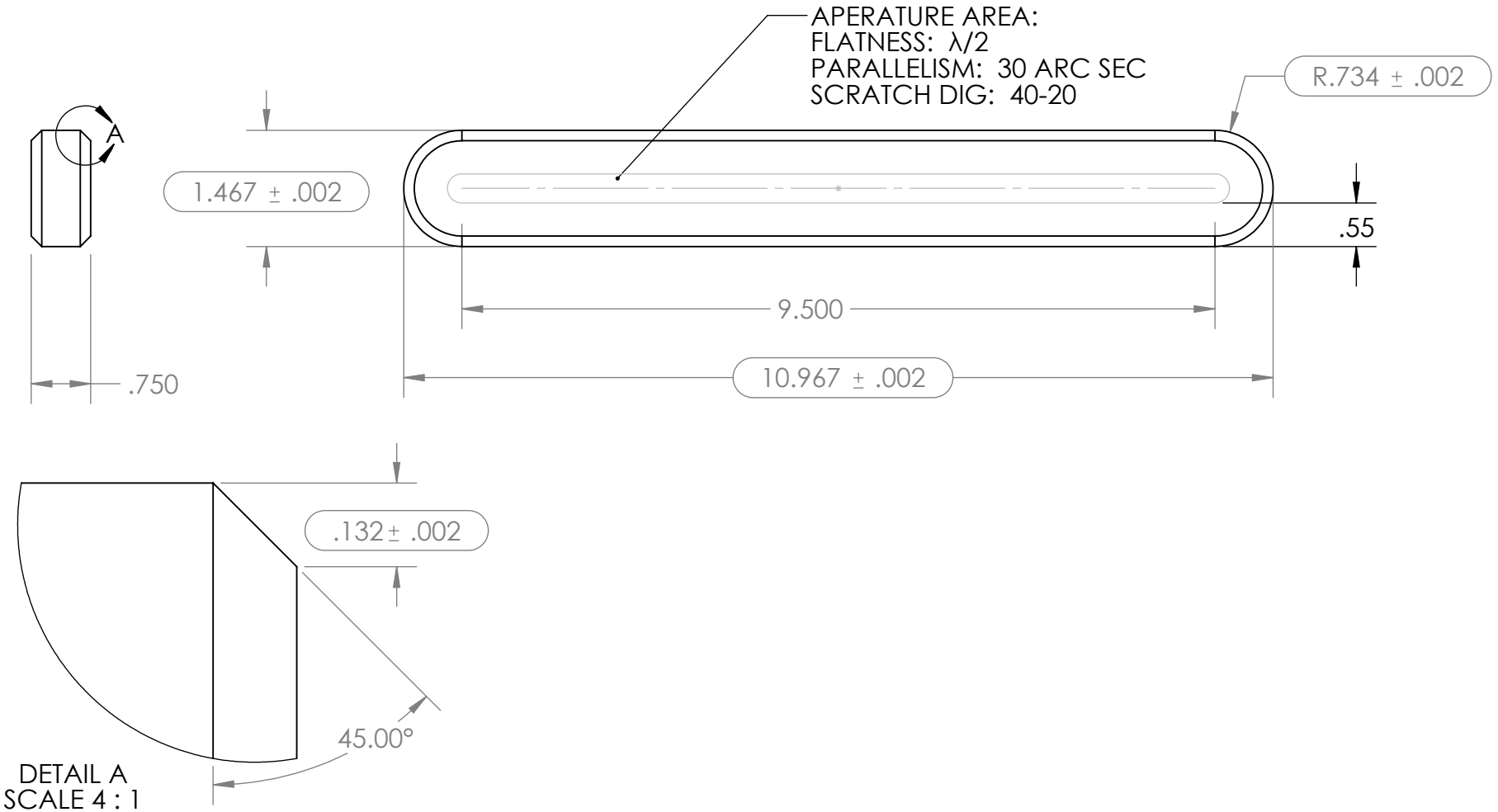

		UNLESS OTHERWISE SPECIFIED:		NAME	DATE	
		DIMENSIONS ARE IN INCHES TOLERANCES: FRACTIONAL ± ANGULAR: MACH ± BEND ± TWO PLACE DECIMAL ± THREE PLACE DECIMAL ± .005	DRAWN	D. Paxson	5-5-15	TITLE: Test Section Window
			CHECKED			
			ENG APPR.			
			MFG APPR.			
		INTERPRET GEOMETRIC TOLERANCING PER:	Q.A.			
		MATERIAL: Fused Silica	COMMENTS:			SIZE: A / DWG. NO.: 001 / REV: D
NEXT ASSY	USED ON	FINISH				
APPLICATION		DO NOT SCALE DRAWING				SCALE: 1:2 / WEIGHT: / SHEET 1 OF 1

Appendix B

User Manual

B.1 Setting up the Optics

B.1.1 Aligning the Interferometer

Minor adjustments can be made to the optical setup using the adjustable mirror mounts and the observed fringe pattern, but if any component is accidentally moved or removed from the beam splitter setup, the procedure below must be used to establish an initial alignment. The accuracy to which the mirrors and beam splitters can be adjusted is directly proportional to how far away the angular displacement of the beams can be measured. This is due to the principal of an optical lever; small angular deflections are manifested as large spatial deflections at a large distance from the source. To maximize the distance from the source, the alignment procedure is performed with the optical table on a workbench away from the rig. It is set up on pieces of wood to prevent movement during alignment which would be likely to happen if it were set on its rubber vibration damping mounts.

First Beam Splitter

The initial alignment is performed with the unexpanded laser beam. This requires removing all the components outlined in Section B.1.2. If the laser has been removed, it should be aligned such that the beam is parallel to the long sides of the optical

table with less than 1 mm deviation over the 90 cm length of the table.

With the beam orientation relative to the table set, the interferometer can be installed, if necessary. If the interferometer base has been removed from the optical table, it must first be bolted down using the three slotted mounting holes and cylindrical posts. With The first plate beam splitter installed and oriented at approximately a 45 ° angle to the table, the interferometer should be positioned such that the beam hits directly in the center of the beam splitter. Location of the beam relative to the plate beam splitter is not critical and as such a precision of only ± 3 mm is needed.

With the first beam splitter in place, the beam is divided into two separate beams. The orientation of the first beam splitter is adjusted using the mirror mount knobs until the beam is horizontal and the reflected and transmitted beams are perpendicular. Perpendicularity is ensured by measuring the sides of the triangle formed by the two beams. This is illustrated in Figures B-2 and B-1.

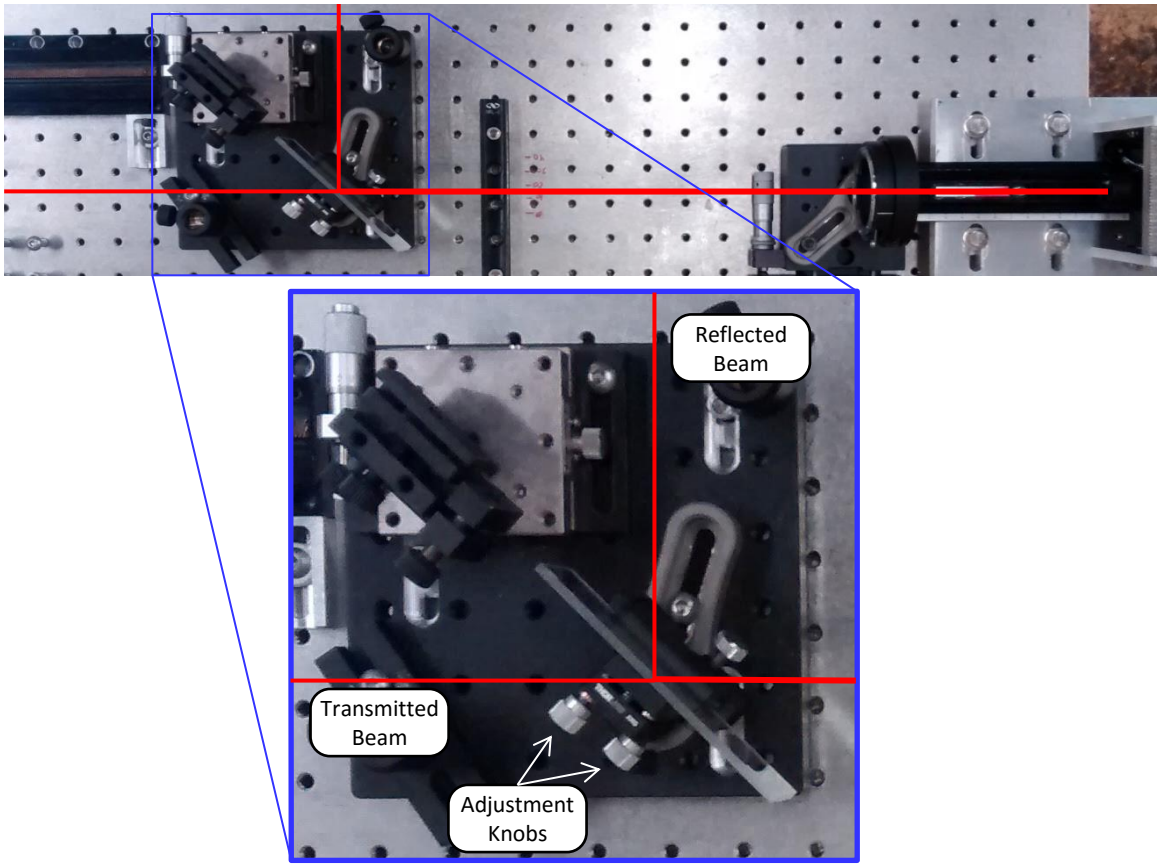

Figure B-1: Image of the Interferometer with only the first beam splitter installed

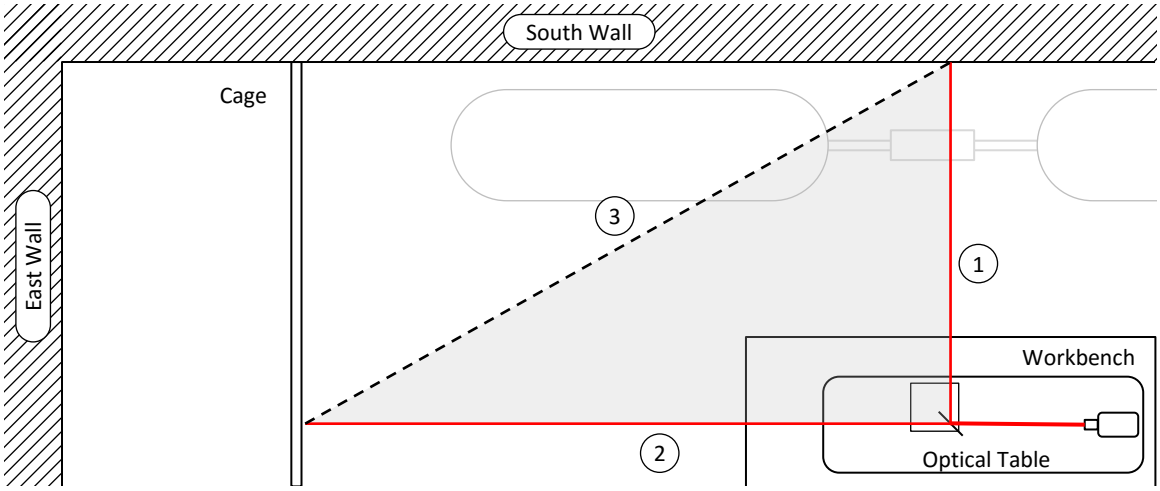

Figure B-2: Schematic of the alignment procedure used to ensure the perpendicularity of the beams reflected from, and transmitted through, the first beam splitter. The measured sides of the triangle formed by the beam are numbered 1-3

First Mirror

Before the first mirror is installed, the location where the reflected beam from the first splitter is marked on the south wall. This will allow for alignment of the second mirror when it is installed. The first mirror is then adjusted such that the now twice reflected beam is parallel to the transmitted beam. Equal horizontal spacing is accomplished by measuring the distance between the two beams at the interferometer and at the cage approximately 3 m away. The orientation of the second mirror is adjusted until the height and spacing of the two beams are equal at all points. This setup is illustrated in Figures B-4 and B-3.

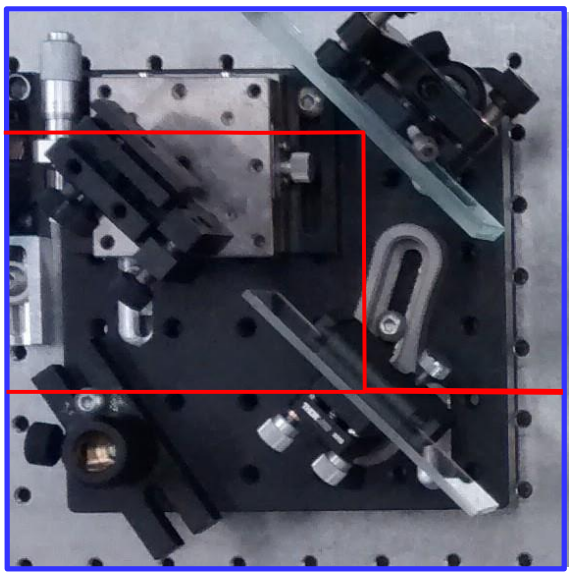

Figure B-3: Image of the Interferometer with the first beam splitter and mirror installed

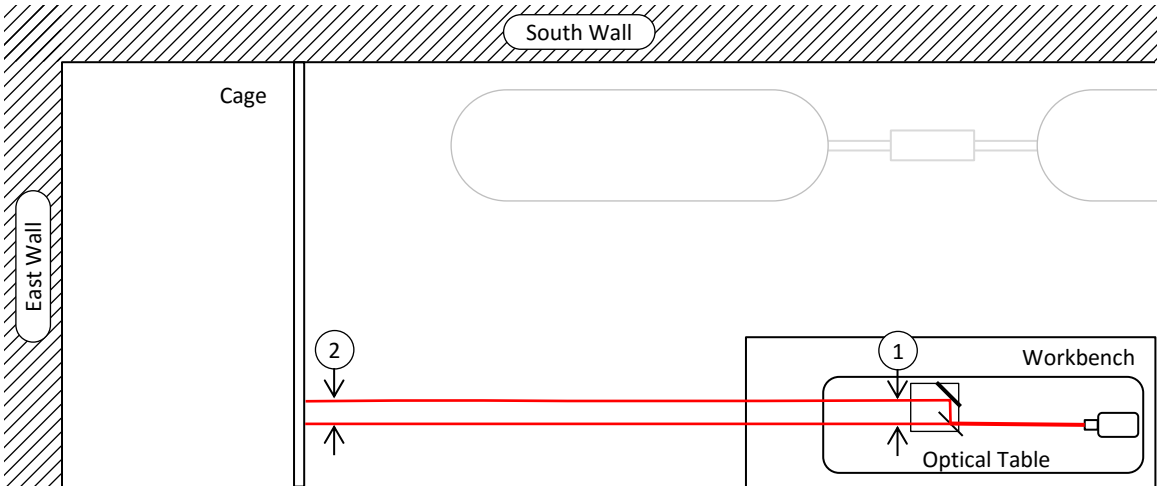

Figure B-4: Schematic of the alignment procedure used to ensure the parallelism of the beams reflected from the first mirror, and transmitted through the first beam splitter. The locations where the beam separation is checked are number 1 & 2

Second Mirror

The second mirror is adjusted using a procedure similar to that used to adjust the first mirror. This mirror must be adjusted such that the reflected beam is parallel to the reflected from the first beam splitter. Since the reflected beam from the first beam splitter is reflected by the first mirror, the spot marked on the wall where the

original beam fell (shown as a dotted line and red circle in Figure B-6) is used as the reference to ensure the beams are at a constant displacement at all locations. The spacing at the interferometer is taken as illustrated in Figure B-5 and compared with the distance between beams at location 2 in Figure B-6. The mirror mount for the second mirror is adjusted until the beam and mark on the wall are at the appropriate spacing and equal height.

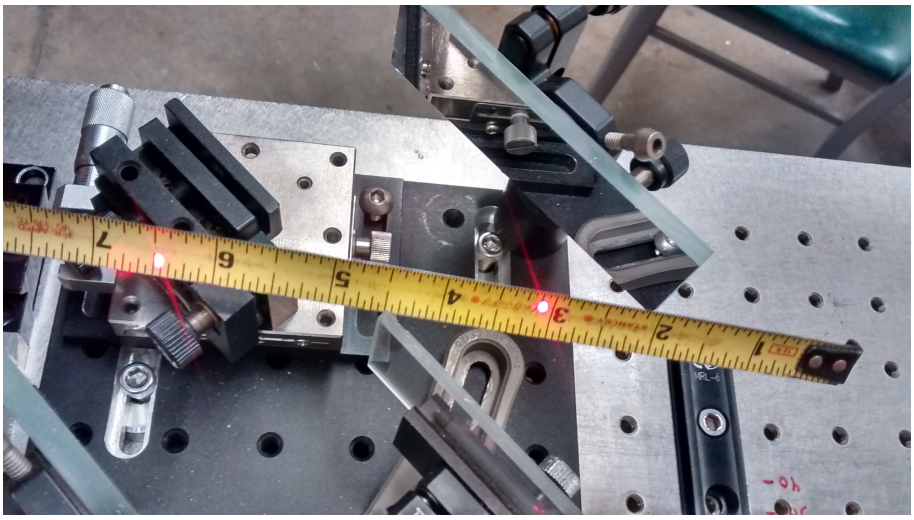

Figure B-5: Measuring the beam displacement at the interferometer (position 1 in Figure B-6)

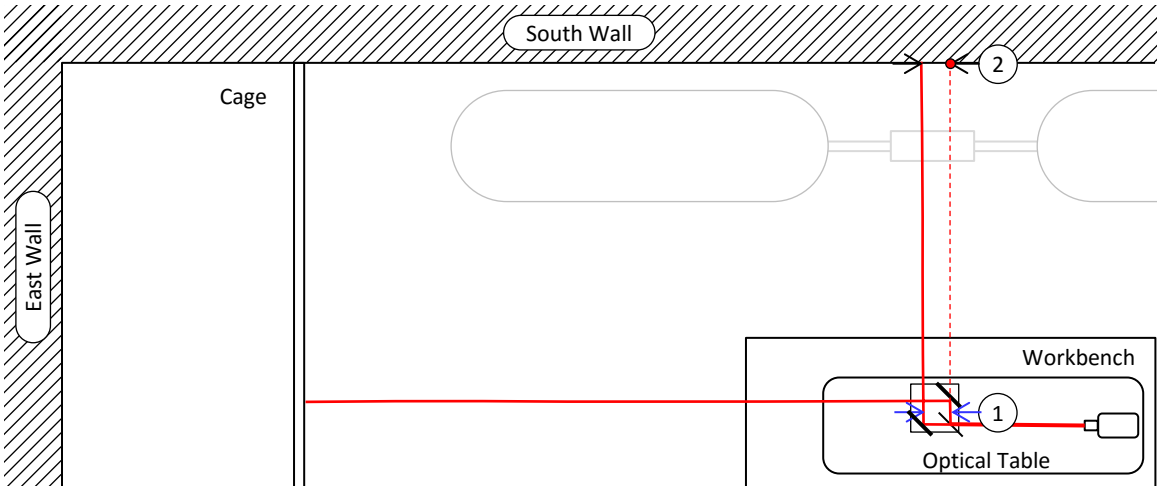

Figure B-6: Schematic of the alignment procedure used to ensure the parallelism of the beams reflected from the first mirror, and transmitted through the first beam splitter. The locations where the beam separation is checked are number 1 & 2

Second Beam Splitter

The second beam splitter combines the reflected beams from mirrors 1 and 2. The mirror is adjusted both in angle using the adjustment knobs and in lateral position using the optical traverse to align the two beams at both the cage and south wall. This is illustrated in Figure B-7.

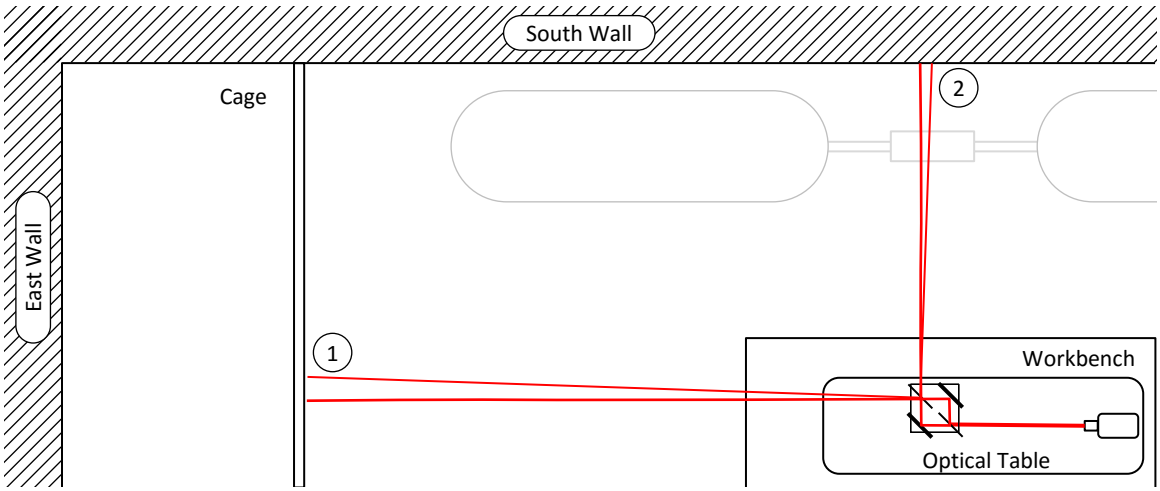

Figure B-7: Schematic of the procedure used to align the second beam splitter, using the optical traverse and the adjustable mount to align the beams at locations 1 and 2

B.1.2 Collimating the Laser Beam

There are four lenses which are used to expand and collimate the laser. The first three, which expand the beam, are mounted to a Linos FLR-40 optical rail further mounted to the aluminum plate which holds the laser. The alignment of the laser with the optical rail is critical as it determines the evenness of the light intensity across the collimated beam. It should not ever need to be changed, but in the event that it needs to be modified, the laser is adjustable using the slotted mounting holes. The laser and rail mount are all bolted to the optical table using cylindrical risers. this allows for 1" of infinite adjustability in the transverse direction, and finite adjustment in 1" increments through the optical table hole pattern in both the longitudinal and transverse directions.

The collimating lens is a manual focus telephoto lens (Manufacturer: Rokinon,

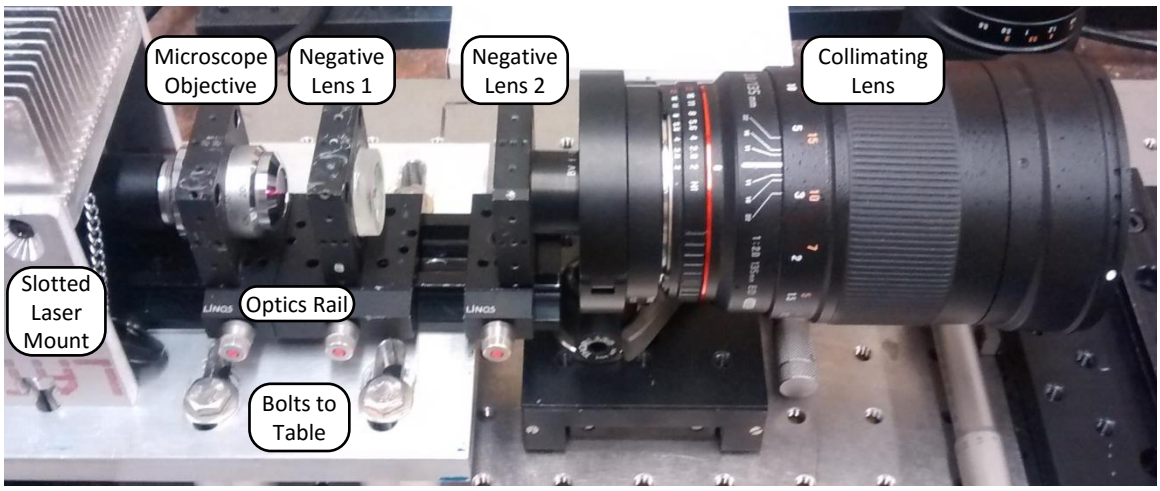

Figure B-8: image of the lenses used to expand and collimate the laser beam for the interferometer

Model: 135M-N). It uses a standard Nikon F-mount which attaches to an F-mount to 2" lens tube adapter and finally to a 2" lens tube clamp and a telescoping post mount (all from ThorLabs). The post mount allows for height adjustment and can be clamped at any location on the table using a clamping fork. There is little adjustability of the optical table relative to the test section in the transverse direction, so the laser and lens must be moved to change the location in the nozzle which is observed. This is not ideal and should probably be changed in the future.

Figure B-8 shows all components used to expand and collimate the beam. The microscope objective is placed as close to the laser as possible, the first negative lens is placed directly in front of the first mount (touching) and the second negative lens is placed 16mm away from the first. A beam filter is also placed between the negative lenses to reduce the brightness of the resulting collimated beam. The post mounted collimated lens is placed such that it is touching the end of the optical rail and is centered on the expanded beam. The beam is then collimated using the focusing ring on the lens until the beam diameter is approximately 60mm with less than 1mm variation over a distance of 3m.

B.1.3 Installing and Focusing the Camera

The camera is installed on a 30 cm traverse. A stop is bolted to the optical table which prevents the carriage on which the camera is mounted from moving too close to the interferometer. If the interferometer position is changed, this stop must be changed as well. With the camera at the stop, the lens can be focused. With the test section removed, an object such as a ruler should be placed at the desired focal plane (5mm from the inside face of the rear window inside the test section). The camera lens can then be adjusted until a clear focused image is observed. The image seen by the camera can be observed in real time using the NikonSLRCameraTest VI accessed through the "camera settings" and "start live view" buttons on the main test VI (blowdown_vi_003).

Before any runs are made, the camera's shutter speed and sensitivity must be set to 1/8000 and 100, respectively. These settings along with all other available camera settings are made in the NikonSLRCameraTest VI mentioned above. Settings are made through the P 6 tab By selecting a feature in the "Enum Capability Tab". The Current setting can be viewed by pressing the "Get Enum Data". A new value can be selected if necessary in the "Index" dropdown and set with the "Set Enum Data" button. This VI is a piece of third party software written by Ackermann Automation. Further information on its capability can be found in their documentation on their website `http://www.ackermann-automation.de/nikonlv_en.htm`.

The camera is powered by an AC adapter and a dummy battery. Most likely due to battery life detection, the camera will begin showing a low battery symbol after being plugged in for longer than approximately 12 hours. To reset this, simply unplug the 4 pin power cable and plug back in. The camera software is also prone to errors, and can cause LabVIEW to freeze. If this happens, kill the LabVIEW process in windows task manager, manually turn the camera off and on, and then restart LabVIEW as usual.

B.1.4 Adjusting the Carrier Fringes

After the beam has been collimated and the lasers adjusted, a fringe pattern should be visible on the camera image. If the alignment was done well, the fringes should be widely spaced as seen in Figure B-9

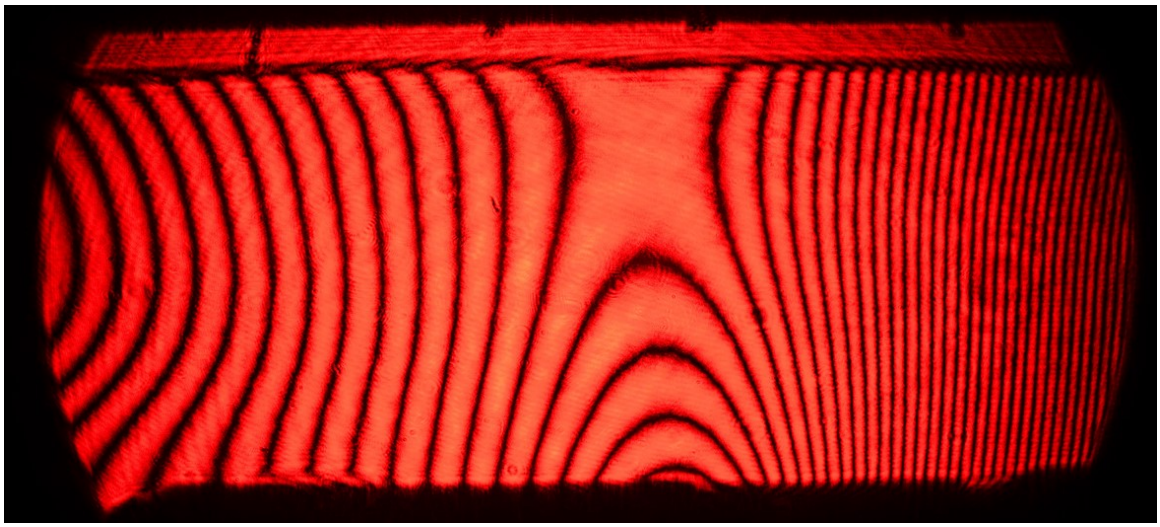

Figure B-9: Initial widely spaced and irregular fringe pattern that should result after alignment

The rotation of the second beam splitter should be adjusted until a fringe pattern with a frequency of approximately 20 pixels per fringe is observed. This should look similar to Figure B-10. The fringe frequency is adjusted by varying the angular orientation of the beam splitter about the vertical axis. The rotation about the horizontal axis can be used to ensure that the fringes are vertical.

A set of fringes adjusted to the desired pattern is shown in Figure B-10

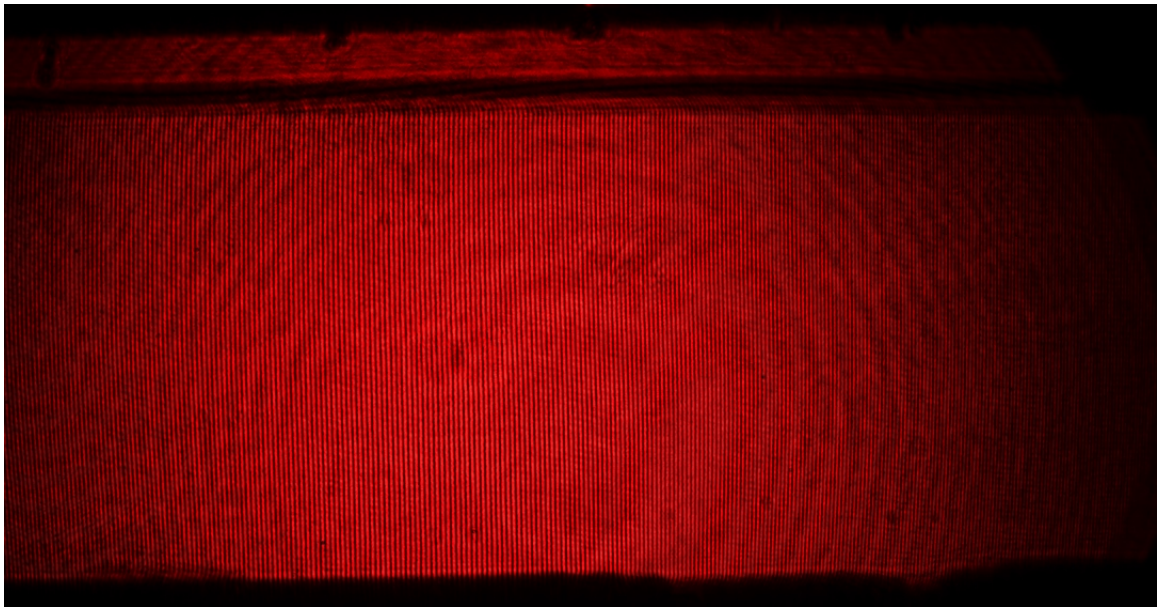

Figure B-10: Fringes adjusted to be vertical and have a horizontal wavelength of approximately 20 pixels

B.2 Operating the Rig

B.2.1 Test Section Maintenance

Disassembling the Test Section

The windows for the test section must be periodically cleaned, especially following runs at temperatures above 330K where powder deposition from the charge tank internal coating is common. The test section must first be rotated 90 degrees to orient the window facing upward. There are four bolts at each end of the test section: two secure the 1/2" thick cradles which allow test section rotation (in the center), and two which rigidly attach the test section to the stand (outside). The latter two socket head bolts, as well as the union fittings at either end, must be removed to allow rotation of the test section to the correct orientation for window removal.

With the retaining flanges now horizontal, the 22 hex head bolts around the window perimeter can be removed and the flange and nylon cushion gasket removed. The windows are removed by attaching a suction cup at each end and evenly pulling up. The clearance between the window and test section pocket is less than 100

microns, so care must be taken to not pull up at an angle. Typically, the o-ring cord stock which seals along the nozzle contour adheres to the window surface. This can usually be reused, so it must be kept for reassembly. The windows are cleaned with an optical cleaning cloth and acetone. This process should be repeated for both windows. The test section with the suction cups attached to the window is shown in Figure B-11.

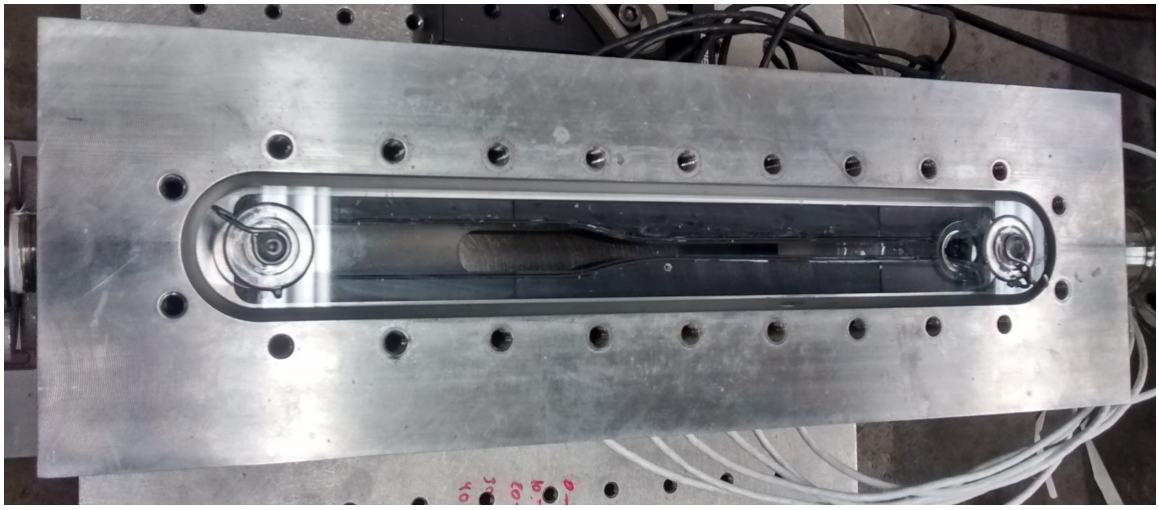

Figure B-11: Test section with the flange removed showing one of the windows with attached suction cups for removal

If the nozzle inserts are to be cleaned or replaced, they can be removed at this point by removing the two Phillips drive button head screws at either end of each insert piece. The screws and washers will fall out when rotating the test section so care should be taken to not lose them.

The Kulites can be removed at any time using custom slotted sockets. There are both 10-32 standard thread (black wire) and m5x0.8 metric thread (white wire) Kulites used on the rig. The black Kulites require a 5/16" hex socket and the white Kulites require a 3/8" socket. Custom machined sockets with a slot through which the wires are passed are in the toolbox. Refer to Kulite documentation for torque specifications. The thread length on the white Kulites is longer than that of the black Kulites, so a threaded spacer is used to provide the right mounting geometry in the test section. This can be seen in more detail in the CAD model.

Reassembling the test section

The nozzle spacers and inserts should be installed from inlet to outlet This is to ensure precise location of the pieces within the test section. While the mounting screws are tightened, pressure should be applied to the inserts to ensure that their front faces are in contact with the inlet wall or the previous insert (whichever is appropriate) Alignment in the direction of the nozzle depth should be adjusted such that there are no steps between the test section and the insert.

To prevent movement during window installation, the o-ring cord stock should be adhered in place using silicone sealant (GE RTV102). A small dot at all the curved sections of the groove is usually sufficient to keep the o-ring in place. As little silicone as possible should be used to prevent it contaminating the flow path.

With the o-rings in place, the windows can be placed back in the test section using the same suction cups, making sure that the orientation is the same as when it was originally installed. Before proceeding, make sure that the o-ring has not shifted out of its intended groove as this could cause the windows to break during tightening of the retaining flange. The nylon cushion gasket must be precisely aligned with the window to prevent pinching it between the test section and retaining flange. With the cushion in place, the flange should be carefully placed on top with all bolts and washers already in place. The central bolts on the top and bottom of the viewing slot should be finger tightened and then slowly tightened with a wrench making sure that the nylon cushion and any wires are not being pinched. After installing all bolts finger-tight, they should be torqued to 12 N·m.

With both windows bolted in place, the test section can be rotated back to the horizontal position. A square should be used to ensure that the front face of the test section is perpendicular to the optical table. When the test section is in the correct orientation the four screws which attach it to the stand should be reinstalled and the unions tightened.

B.2.2 Filling the Tank

The following steps should be used to fill the tank. Note that there is a different procedure for an empty tank and a full tank. All relevant fluid controls and components are labeled in Figure B-12, and all electrical controls are labeled in Figure B-15.

Filling an Empty Tank

1. With the test section in place and both unions tightened, open valve 20 manually and open valves 14 and 16 using the "Purge Tank" button in the LabVIEW VI

2. When pressure in the tank reaches ambient, close valve 20, open valve 18 and plug in vacuum pump until tank pressure reads less than 0.15 bar

3. Unplug vacuum pump, close test section valves by turning off "Purge Tank" switch, close valve 18, and open valve 20

4. Disconnect upstream union and tare load cell

5. Connect the braided pump inlet hose to the liquid outlet valve on the Dewar (6) using the attached CGA-622 fitting

6. Connect the 500 psi regulator (2) to a full 50 pound CO_2 bottle and connect the attached hose to the vent valve on the Dewar (4) using the attached CGA-622 fitting

7. If the Dewar is at a pressure higher than 350 psi open valves 3 and 4 and purge until the pressure reaches 350 psi then close valve 3. Hearing protection is recommended here since purging into the vent is fairly loud. This line should probably be plumbed into the main roof vent line with a dedicated hose at some point.

8. Set the regulator (2) to 400 psi to pressurize Dewar (See Chapter 6 for an explanation of this step)

9. When Dewar pressure gauge reads 400 psi, slowly open valve 6 until the pump line equalizes in pressure with the Dewar, then fully open

10. Open valve 11 and watch load cell readout to make sure CO_2 is flowing into the tank

11. When CO_2 transfer rate drops to approximately 4 kg/min, turn on the pump motor using green "run" button on the motor control panel (shown in Figure B-14) and set speed to 1500 rpm using the speed control knob. Make sure the motor is in the forward mode as indicated by the LED at the top right of the motor speed read out

12. turn off pump using red "stop/reset" button when the desired mass is shown on the load cell read out and immediately close valve 11

13. Close valves 4 and 6 and open valve 10 to purge all pump lines

14. Reconnect the upstream union to the test section

Adding CO_2 to Partially Filled Tank

1. Disconnect upstream union and check accuracy of current load cell reading

2. Connect the braided pump inlet hose to the liquid outlet valve on the Dewar (6) using the attached CGA-622 fitting

3. Connect the 500 psi regulator (2) to a full 50 pound CO_2 bottle and connect the attached hose to the vent valve on the Dewar (4) using the attached CGA-622 fitting

4. If the Dewar is at a pressure higher than 350 psi open valves 3 and 4 and purge until the pressure reaches 350 psi then close valve 3. Hearing protection is recommended here since purging into the vent is fairly loud. This line should probably be plumbed into the main roof vent line with a dedicated hose at some point.

5. Set the regulator (2) to 400 psi to pressurize Dewar (See Chapter 6 for an explanation of this step)

6. When Dewar pressure gauge reads 400 psi, slowly open valve 6 until the pump line equalizes in pressure with the Dewar, then fully open

7. Open valve 8 for 1-2 seconds to purge any CO_2 gas from the pump inlet

8. Turn on the pump motor to 750 rpm following the same directions as outlined in step 11 in the previous set of direction

9. Open purge valve 10 for 1-2 seconds to purge the pump outlet lines then simultaneously close valve 10 and open valve 11. This allows the pump to prime with little back pressure before being subjected to the pressure in the tank

10. When tank mass is steadily increasing at a rate of approximately 2-3 kg/min, increase motor speed to 1500 rpm

11. If CO_2 flow stops or never initiates, close valve 11 and immediately repeat step 9

12. Turn off pump using red "stop/reset" button when the desired mass is shown on the load cell read out and immediately close valve 11

13. Close valves 4 and 6 and open valve 10 to purge all pump lines

14. Reconnect the upstream union to the test section

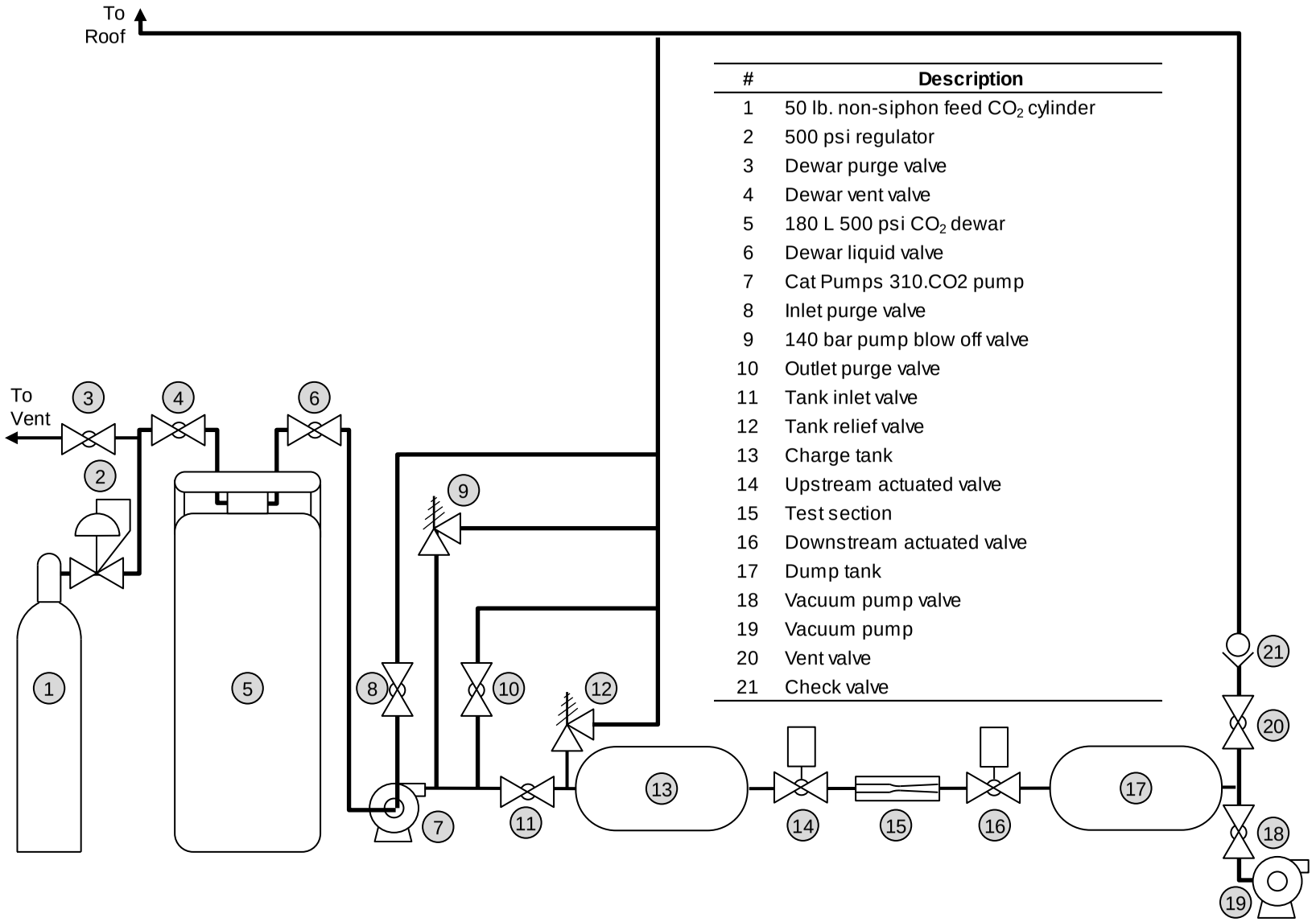

#	Description
1	50 lb. non-siphon feed CO_2 cylinder
2	500 psi regulator
3	Dewar purge valve
4	Dewar vent valve
5	180 L 500 psi CO_2 dewar
6	Dewar liquid valve
7	Cat Pumps 310.CO2 pump
8	Inlet purge valve
9	140 bar pump blow off valve
10	Outlet purge valve
11	Tank inlet valve
12	Tank relief valve
13	Charge tank
14	Upstream actuated valve
15	Test section
16	Downstream actuated valve
17	Dump tank
18	Vacuum pump valve
19	Vacuum pump
20	Vent valve
21	Check valve

Figure B-12: Schematic of the rig showing all valves and other fluid components

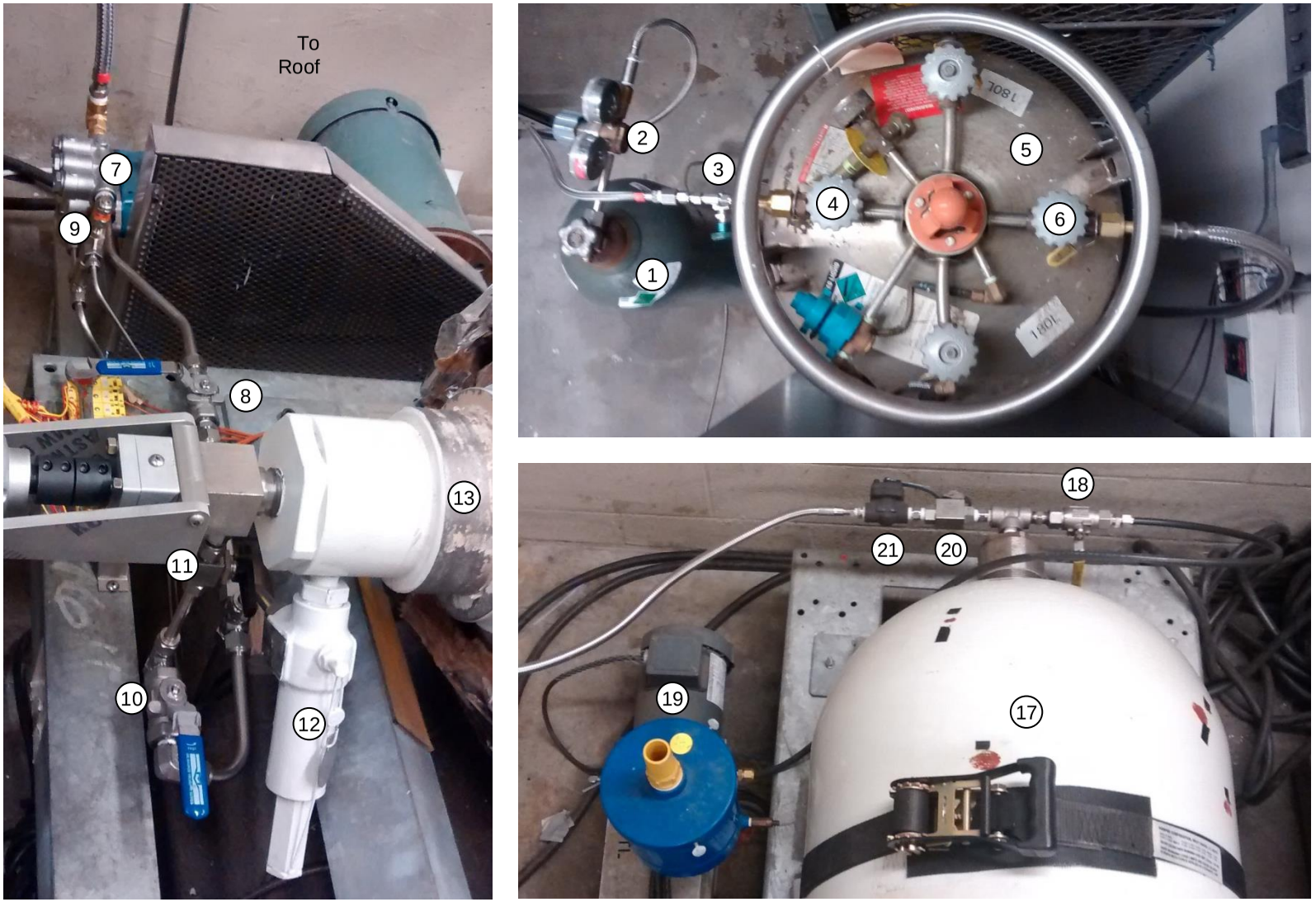

Figure B-13: Image of the rig with components labeled using the same numbering scheme as that used in Figure B-12

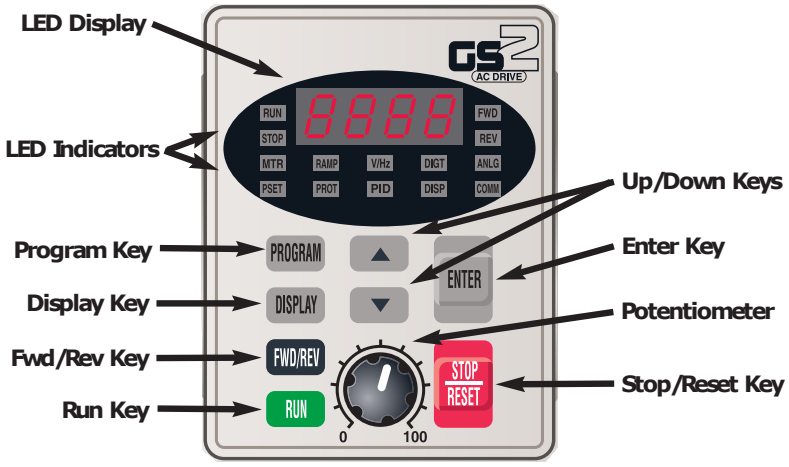

Figure B-14: Motor control panel

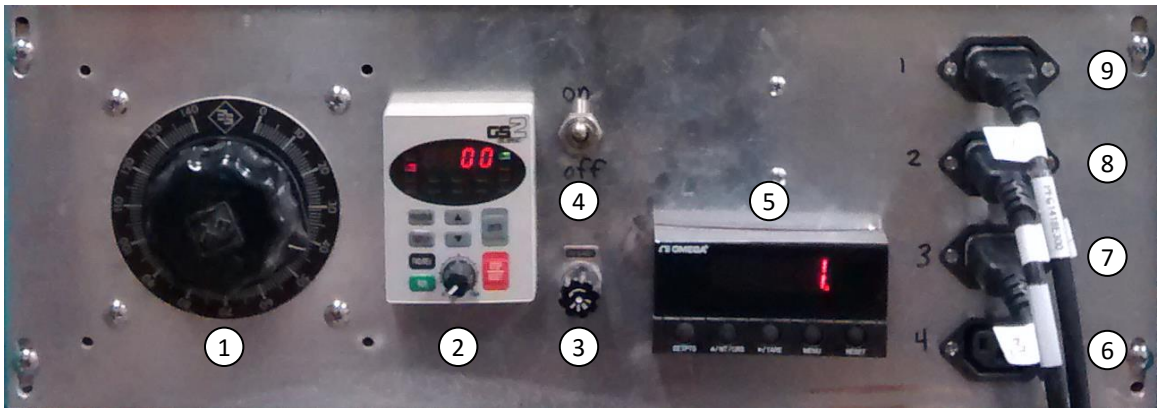

Figure B-15: Rack mounted control panel showing (1) mixer motor VARIAC control, (2) pump control panel, (3) 110V 10A fuse, (4) main power switch, (5) load cell read out , (6) unused relay output, (7) downstream valve output, (8) upstream valve output, (9) mixer motor output

B.3 Heating the Tank

The heating circuit is set up with a latching relay circuit connected to a thermal switch on the tank. If the temperature of the tank goes above 400 K, the thermal switch will trip and cause the heating tapes to turn off. The latching circuit is implemented such that the tapes won't turn back on once the temperature drops below 400 K. As a consequence of this design, turning of the power to the rig using the E-stop switches trips the latching circuit and the reset button on the gray box on the south wall must be pressed to turn on the heaters.

The tank heating rate is currently limited by the 20 amp circuit to which the triple VARIAC cabinet is wired. The cabinet is shown in Figure B-16. Typical max power settings for the heaters are 200V for tapes 1 and 2, and 75 volts for tape 3. Typical settings for reheating between runs are 150V for tapes 1 and 2 and 50 volts for tape 3. These settings produce little variation in temperature across the tank during heating. There is no convenient way to actively cool the tank, so heating should be done slowly, reducing the power to the tapes as the desired set point is approached. Typical cooling rates are 2-3 K/hour so overshooting the set point can be a time consuming error. The mixer motor should be used to ensure that there is less than 0.1 K difference between internal and average tank temperature and less than 0.2 K variation in thermocouple readings at all points in the tank. The motor should be run at a duty cycle of approximately 50% with a period of approximately 3 minutes (3 minutes on, 3 minutes off). Supply voltage should be set to a maximum of 110V (set on the VARIAC shown in Figure B-15

Figure B-16: 208V 3-phase VARIAC cabinet used to control the heating tapes

B.4 Performing a Run

B.4.1 Calibrating the interferometer

Before any density measurements can be made, the interferometer must be set up and the fringe pattern adjusted this procedure is covered in Section B.1.4. With the fringe pattern set, the beam displacement must be set and recorded. Setting the beam displacement is achieved by changing the physical location of the second beam splitter using a micrometer slide. The displacement near the throat (right side of image) should be no more than 300 microns (30 pixels) with the displacement increasing towards the inlet (left side).

As covered in Chapter 5, four four-point calibration images (16 measurement locations) are required to accurately capture the interferometer displacement across the entire field of view. Since this is a time consuming process, it is quicker to use only single four point images to evaluate the approximate displacement while it is

being adjusted with the micrometer, and then take the remaining three images once an appropriate setting has been found.

Steps for taking a set of initial calibration images

1. With the test section removed, clamp the four edged knife edge on the optical rail in the center of the optical table and clamp such that the four knife edges are approximately centered on the field of view as shown in Figure B-17.

2. Move the beam blocker to the lowest possible position using the height adjust knob shown in Figure B-18. This allows the beam through the right leg (from the camera's perspective) to pass through to the camera

3. Capture an image using the "Capture and Save" Button on the NikonSLRCameraTest VI.

4. Raise the beam blocker until the green mark on the chrome post is just above the black base. Figure B-18 shows the beam blocker mount in the raised position and the green mark is indicated by the green arrow. This position allows the beam through the left leg (from the camera's perspective) to pass through to the camera

5. Capture an image using the "Capture and Save" Button on the NikonSLRCameraTest VI. Call this image "right.jpg" or something else descriptive

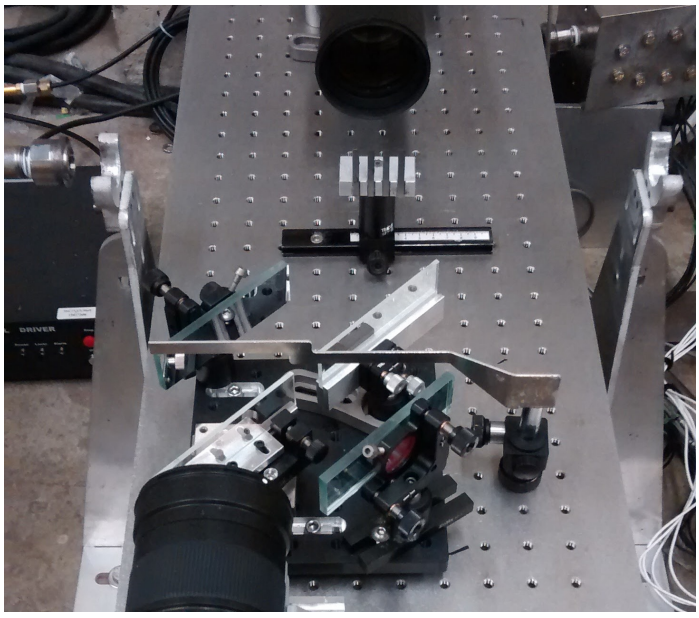

(a)

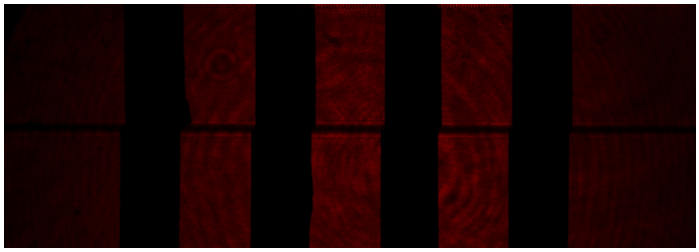

(b)

Figure B-17: Interferometer setup (a), and resulting image (b) used to measure the displacement

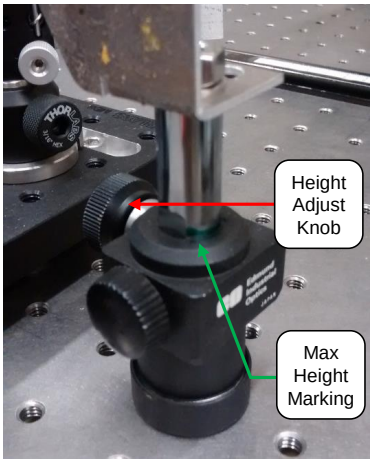

(a) Raised position

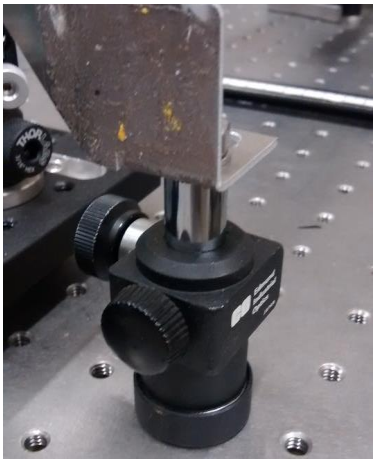

(b) Lowered position

Figure B-18: Height adjustable mount for the beam blocker showing green marking indicating raised position (a and lowered position (b)

Processing Displacement Images in MATLAB

1. Run the MATLAB file "multi_point_calibration_final.m"

2. Follow the file dialog prompts to load the left and right images taken before

3. If processing only one image (four points), select no on the dialog that comes up after selecting the images

4. Review the displacement information in the displayed plot

Repeat the procedures above until a micrometer setting which yields an appropriate image displacement (25 pixels at the right and increasing in displacement to the left) is found. To establish the final displacement curve, the above process should be repeated at four locations with spaced 3mm apart; e.g. 25, 28, 31, 34mm as measured by the right edge of the knife edge mount where it meets the ruler on the optical rail. The first image location should be set such that the first knife edge is past the curved edge of the field of view by at least 1mm in both the left and right images. If this is not the case, the MATLAB code will most likely crash or produce unrealistic results. To post process multiple images, simply click yes in the message box that comes up after selecting set of images when using the MATLAB file described above.

B.4.2 Calibrating the Sensors

Before a run is performed, the pressure sensors need to be calibrated. First, ensure that the dump tank is at ambient pressure and open the downstream valve using the VI to make sure that the Kulites are also at ambient. First, zero balance all the Kulite amplifiers by pressing down on the "Auto-Bal" switch on each amplifier. A red light should illuminate and then go out when the zero point is reached. The Kulites are calibrated using an automatic procedure built in to the VI. Before calibration, ensure that valve 18 is closed, valve 20 is open, and both unions are securely tightened. To run the calibration procedure, switch on the "Arm Experiment" switch and then press the calibrate sensors button. The calibration procedure takes about 10 seconds and

will result the in the pressurization and depressurization of the test section so stand clear of the windows while performing it.

B.5 Performing a Blowdown Run

Before starting a run where the interferometer will be used, it is good practice to take a test image with the laser on to make sure that the image is clear, there is no contamination of the windows, and that the camera is communicating with LabVIEW. For safety, the laser is connected to a power strip which also powers a flashing safety light outside the test cell. Power up the laser by turning on this power strip (located to the right of the computer) and turn on the main switch on the laser power supply. To turn of the laser, press the red round momentary button on the power supply and then switch off the main power switch.

Pre-Run Checklist

It is good practice to go over the following checklist before performing a run to prevent dangerous or expensive mistakes:

- Test section unions tightened
- Laser on
- Camera settings are correct and test image worked correctly
- Kulites have been calibrated
- Test section shows no visible leaks when pressurized
- Interferometer has been calibrated and displacement measurements recorded
- Valve 18 closed and valve 20 open

To perform a run, simply input all the relevant information in the bottom left input boxes of the VI, arm the experiment, press the large green "Start Run" button,

and confirm that you want to start a blowdown run. This will start the automatic process of taking images and opening the actuated valves. When the run completes a file dialog will pop up requesting a file name and location for the resulting files. It is recommended to make a new folder for each run as four separate files are produced by the VI (before, during, and after images, and the logged data values).

B.6 Post Processing Interferometer Images

B.6.1 Establishing the Nozzle Location

Run the MATLAB file get_zero_point.m. Load the calibration image from which the zero will be determined using the GUI. This can be any of before or after images from a set of runs. Zoom in on the location of the pinhole and hit enter. Use the mouse to select the pinhole location (red dot just above the nozzle throat). There will be a double image of the pinhole so select the right-most one. This will produce a .mat file called "zero.mat" in the folder in which the image is contained. Copy this file to all the directories which will use this same nozzle location (typically a set of runs done in a day)

B.6.2 Create Composite Image

Run the MATLAB file crop_equalize_images.m. select the folder which contains the before, during, and after images as well as the zero.mat file created before. The program will display an image of the nozzle. Click at the approximate top and bottom edge of the nozzle at the throat using the crosshairs. The average y location of these points will be used to establish the centerline of the nozzle. After this, the program will ask whether other sets of images should be post processed with the same crop window. This feature is meant to simplify the post-processing of a set of runs done in the same day with the same nozzle position. It this is the case, select yes and then select the folders you wish to process. This will produce equalized and cropped versions of the before, during, and after images, as well as a composite image called

composite.tif which contains all three.

B.6.3 FFT Filtering Process

The FFT filtering process is performed in UU, a piece of software written by Prof. Chen Lujie at Singapore Institute of Technology and Design. The steps to perform the filtering process are listed below. An accompanying video (UU_Demo.mp4), is a video recording of the process on a sample file

Steps to Filter Composite Image

1. Run UU.exe and load the composite image which is to be processed. (file - open)

2. Create 2-D FFT of composite image (Tool - Transform - FFT). Three new images will be produced, FFT real, FFT imaginary, FFT Power.

3. Create pass window in the resulting FFT Power image half height of the image, centered top-to-bottom, completely containing the right-hand power band. See video or 5 for more details. (Tool - Transform - Pass Window)

4. Click first on the FFT Real image and then FFT Imaginary image confirming the resulting check boxes. This applies the pass window to all three images.

5. Perform Inverse FFT on all three images by selecting (Tool - Transform - Inverse FFT) on the FFT power image and then repeat the previous set (click on the real and imaginary images)

6. Select the resulting FFT phase image and perform a left-to-right unwrapping (Metrology - left-to-right unwrapping)

7. Export the resulting unwrapped image as an ASCII file named "L-to-R unwrapping.asc

B.6.4 Extracting Density Information

The averaging and integration process used to extract density data from the unwrapped image produced by UU is performed using the MATLAB function extract_from_composite.m. The code includes comments which describe the inputs and outputs. Open the .m file or type "help extract_from_composite" in MATLAB to see this information